



Attribution–NonCommercial–NoDerivs 2.0 KOREA

You are free to :

- **Share** — copy and redistribute the material in any medium or format

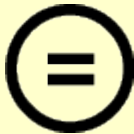
Under the following terms :



Attribution — You must give [appropriate credit](#), provide a link to the license, and [indicate if changes were made](#). You may do so in any reasonable manner, but not in any way that suggests the licensor endorses you or your use.




NonCommercial — You may not use the material for [commercial purposes](#).



NoDerivatives — If you [remix, transform, or build upon](#) the material, you may not distribute the modified material.

You do not have to comply with the license for elements of the material in the public domain or where your use is permitted by an applicable exception or limitation.

This is a human-readable summary of (and not a substitute for) the [license](#).

[Disclaimer](#) 

Doctoral Thesis

**Experimentation and Modelling of
Nanostructured Nickel Cermet Anodes
for Submicron SOFCs Fueled
Indirectly by Industry Waste Carbon**

,

August 2017

**Graduate School of Engineering
Seoul National University
Mechanical & Aerospace Engineering
Waqas Hassan Tanveer**

**Experimentation and Modelling of Nanostructured
Nickel Cermet Anodes for Submicron SOFCs Fueled
Indirectly by Industry Waste Carbon**

Advisor: Prof. Cha Suk Won

by

Waqas Hassan Tanveer

A dissertation submitted in the partial fulfillment
of the requirements of the degree of
DOCTOR OF PHILOSOPHY

**Department of Mechanical and Aerospace Engineering
Seoul National University**

August 2017

Abstract

Nickel-Samaria Doped Ceria (Ni-SDC) cermet anodic thin films were prepared on Scandia Stabilized Zirconia (ScSZ) electrolyte supports by two distinct physical vapor deposition processes, 1) pulsed laser deposition (PLD) 2) radio frequency (RF) sputtering. For PLD, the deposition was carried out at a target temperature range of 0°C ~ 700°C. For RF sputtering, the target temperature was kept constant at room temperature of 25°C, however the background sputtering gas was either Ar or Ar:O₂/80:20. Once the intended deposition conditions were established, the Ni-SDC anodes were deposited with a range of different sputtering powers (50W ~ 200W) and background Ar gas pressures (30mTorr ~ 90mTorr). The oxide conducting fuel cell configuration was completed by screen printing of lanthanum strontium manganite (LSM/YSZ) cathodes on the other side of ScSZ supports. Peak performance comparison of these cells was measured under hydrogen (H₂) fuel source at an intermediate temperature range of 600°C ~ 800°C by voltage-current-power curves. The resistances of various cell components were observed by nyquist plots.

Initial results showed that anode thin films made at increased target temperature, pressure, and high deposition power, performed better than the low powered ones, for a specific Ar or O₂ pressure. Interestingly, however, anodes made at the highest power and the highest pressure, were not the ones that showed the maximum power output at an intermediate oxide fuel cell temperature range. Eventually, an optimal condition was reported for high performance thin film Ni-SDC anodes. These high performance anodes were then tested under an indirect carbon fuel source which utilizes raw unprocessed cheap carbon in a simple home-made gasifier. The carbon fuel source matched up to the H₂ fuel in terms of a) peak power b) longevity c) lowered costs.

Key Words:

Nickel-Samaria Doped Ceria thin film anodes, Scandia Stabilized Zirconia (ScSZ) electrolyte supports, Radio Frequency Sputtering, Pulsed laser deposition, Intermediate temperature oxide conducting fuel cells, Indirect carbon fuel

Student Number: 2013-31291

Table of Contents

Abstract	3
List of Figures	7
List of Tables	12
1. Introduction	14
1.1 Motivation	14
1.2 Background Literature Survey	16
1.2.1. The need for cermet anodes	16
1.2.2. Why Thin Film Fabrication.....	17
1.2.3. Carbon as a fuel source	21
2. Methods and Materials	23
2.1 ScSZ electrolyte support fabrication.....	23
2.2 LSM/YSZ cathode formation	23
2.3 Ni-SDC anode formation	24
2.4 Cell test setup.....	25
3. Thin Film Physical Vapor Deposition of the Nickel Cermet Anodes	29
3.1 Pulsed Laser Deposition of Ni-SDC	29
3.1.1. Under the microscope	30
3.1.2. Performance	32
3.1.3. X-ray diffraction analysis	35
3.1.4. EPMA analysis.....	36
3.2 Sputtering of Ni-SDC thin film anodes.....	39
3.2.1. Under the microscope	40
3.2.2. Performance Comparison	43
3.2.3. EIS Characterization	44
3.2.4. XPS analysis	47
3.2.5. EPMA analysis.....	50
3.2.6. Anode Lifetime	52
3.2.7. Logging the optimal sputtering conditions for thin film Ni-SDC anodes	54
4. Utilization of Carbon as an indirect source of fuel for the optimized cell	68
4.1 The Reverse Boudouard Reaction (RBR).....	73
4.1.1 The gasification of carbon with Inconel Filter	74
4.1.2 The Indirect Carbon Fueled Hybrid Fuel Cell	75

5. Simulation of the Optimal Ni-SDC Anode	84
6. Concluding Remarks	103
6.1 Conclusion	103
6.2 Future Work	105
References.....	106
국문 초록	117

List of Figures

Fig. 1 Post operation SEM image of slurry sprayed BCZY at 1500°C for 2hrs

Fig. 2 Post operation SEM image of PLD/Ni-SDC on ScSZ substrate at room temperature

Fig. 3 FE-SEM images of the Pt anode surface morphologies deposited by sputtering on AAO at various Ar pressures

Fig. 4 Scanning electron microscope micrographs of the resulting Pt films as a function of the oxygen ratio, $O_2/(O_2 + Ar)$ utilized during sputtering

Fig. 5 The process of uni-axial pressing of ScSZ powder followed by sintering and machining

Fig 6 The screen printing board with a hand-made plastic brush. Magnified image shows the dimension and structure of the mesh

Fig. 7 The physical vapor deposition (PVD) vacuum chambers

Fig. 8 Schematic of the thin film hybrid fuel cell

Fig 9 (a) $1 \times 1 \text{ cm}^2$ cell, (b) Test station placed in center of furnace (c) Jig to hold the cell (d) Ceramic rod attached to turn screw to apply pressure for sealing anode from cathode gas

Fig. 10 Schematic representation of pulsed laser deposition process

Fig. 11 (a) SEM image of PLD/Ni-SDC on ScSZ substrate at room temperature, (b) top surface SEM of Ni-SDC deposited at room temperature

Fig. 12 Peak Power density comparisons of PLD/ Ni-SDC anode cell fabricated at different temperatures

Fig. 13 EIS measurements of the PLD/Ni-SDC anode cell fabricated at different temperatures

Fig. 14 XRD measurements of PLD/Ni-SDC pre-operation, non-reduction anode cell fabricated at room temperature and 700°C. (*) marks the unidentified peaks

Fig. 15 XRD measurements of PLD/ Ni-YSZ anode at various temperatures after reduction in H₂ atmosphere by Noh et al.

Fig. 16 Electron Probe Micro Analysis (EPMA) of PLD Ni-SDC anode, (a)&(c) pre- and post-operation, of anodes deposited at room temperature, (b)&(d) pre and post operation of anodes deposited at 700°C

Fig. 17 Schematic Representation of the sputtering process

Fig. 18 Post operation SEM of sputtered Ni-SDC on ScSZ substrate at room temperature at Ar/O₂:80/20 reactive sputtering gas& Top surface SEM of Ni-SDC deposited at room temperature

Fig. 19 SEM image of (a) ScSZ electrolyte support (b)microstructure of LSM/YSZ cathode, (c) top view of the Ni-SDC anode made by reactive sputtering (Ar/O₂:8/2), pre-operation (d) high-resolution SEM image of the same anode after cell test at 800C in H₂ (e) growth rate comparison of the anodes with time

Fig. 20 Polarization curves for cells, having reactively (Ar/O₂:8/2) and non-reactively (Ar only) sputtered Ni-SDC anodes, at various temperatures

Fig. 21 Electrochemical impedance spectroscopy (EIS) analysis of the cells, having reactively (Ar/O₂:80/20) and non-reactively (Ar only) sputtered Ni-SDC anodes, at various temperatures

Fig. 22 Ni2P XPS spectra of the two anodes before (a) and after (b) electrochemical evaluation, (The dashed lines are peak values of Ni²⁺ and Ni⁰ in theory), Ce3d XPS spectra of the anodes before(c) and after (b) electrochemical evaluation

Fig. 23 Electron Probe Micro Analysis (EPMA) of Ni-SDC sputtered anode, (a) pre-operation Ar only, (b) pre-operation Ar/O₂:8/2, (c) post-operation Ar only, (d) post-operation Ar/O₂:8/2

Fig 24 (a)&(c) Pre-operation (b)&(d) Post-operation top view SEM images of Ni-SDC anode. (e) Peak power density comparison of the Ni-SDC anodes with time at 800°C

Fig 25 Peak power density comparison of the Ni-SDC anodes with time at 800°C

Fig 26. Deposition rate for Ni-SDC at various pressures and sputtering powers

Fig 27 Post operation analysis of Ni-SDC anodes after 12hrs of electrochemical tests

Fig. 28 Performance Analysis of cells with Ni-SDC anodes sputtered at various powers at 90mTorr

Fig. 29 EIS of the cells from Fig. 28

Fig. 30 EIS plots of cells deposited with Ni-SDC anodes at sputtering powers (50-200W) at various applied biases

Fig. 31 Atomic Force Microscopy (AFM) of the Ni-SDC anode samples deposited at different sputtering powers, on top of ScSZ electrolytes

Fig. 32 Peak power density and low frequency arc of the nyquist plot comparison at 700°C, for thin film Ni-SDC anode fabrication via RF sputtering at various sputtering pressures and powers

Fig. 33 Usage of Carbon as direct source of fuel to the optimized cell concept

Fig. 34 Ball milled carbon placed on the anode compartment sealed by a gold ring

Fig. 35 Peak power density comparison for the two carbons with and without H₂ fuel.

Fig 36. Schematic representation of the carbon reaction sites in a cermet anode on a ScSZ electrolyte base

Fig. 37 Anode less cell test for (a) Pure (b) Impure carbon at 700°C.

Fig. 38 Inconel Filter and its attachment on the bubbler assembly

Fig. 39 Schematic Representation of the indirect carbon fueled hybrid fuel cell

Fig. 40 Off-grid Gas Chromatography results of 5g of carbon. OCV of the cells was taken with time at various temperatures

Fig. 41 Peak Power Density comparison for the indirect carbon fueled hybrid fuel cell at 700°C

Fig. 42 Peak power density and OCV shift with time

Fig. 43 (a) Schematic of the old design of the Bubbler with little or no CO (b) modification in the bubbler design resulting in higher carbon utilization and hence higher CO.

Fig. 44 Peak Power Density comparison for the indirect carbon fueled hybrid fuel cell at 700°C

Fig. 45 Peak power density and OCV with time for the updated bubbler

Fig.46 Peak power density and OCV comparison of the optimal carbon fuel cell proposed in this study with previous reported cells.

Fig.47 Schematic representation of the nanostructured anode for simulation

Fig.48 High resolution SEM image of the Ni-SDC anode and phase separation by Image J

Fig.49 Magnified view of the HRSEM Ni-SDC anode with triple phase boundaries marked

Fig.50 TPB strings for Ni-SDC anode formed by volume expansion method

Fig.51 HRTEM image of the Ni-SDC anode, clearly distinguishing the Ni, SDC and Pore grain sizes

Fig.52 Schematic representation of the point P inside the Ni-SDC anode solved by control volume method

Fig 53. Volume specific current and potential distributions from simulation. Anode over-potential is set to be 0.05V

Fig 54. Anode over-potentials at various temperatures for indirect carbon fueled SOFC

Fig. 55 (a) Scanning Transmission Electron Microscope (STEM) image of the Ni-SDC anode on top of the ScSZ electrolyte (b) EDX image of the electrolyte and anode junction (c) schematic representation of the Ni-SDC TPBs.

List of Tables

Table 1. Deposition conditions for the Ni-SDC anodes on ScSZ substrates by pulsed laser deposition(PLD). Target to substrate distance was 6cm

Table 2 Resistances measured by curve fitting of the nyquist plots from Fig.12

Table 3. Deposition conditions for the Ni-SDC anodes on SSZ substrates by RF sputtering

Table 4. Resistance values at the anode and cathode of the two cell types obtained via curve fitting of EIS plots from Fig.20

Table 5. XPS analysis of the RF sputtered Ni-SDC anodes

Table 6. Deposition rates of Ni-SDC anodes deposited at various pressures and sputtering powers

Table 7. XPS analysis of various constituent of the cermet Ni-SDC anode at various powers

Table 8. Resistance values at the anode and cathode of the cell obtained via curve fitting of EIS plots from Fig.29.

Table 9. The equations involved in the indirect utilization of carbon fuel.

Table 10. Volume Fractions V_i of each phase [%]

Table 11. TPB densities from three different images similar to Fig. 50

Table 12. Average grain sizes, contiguities and tortuosities for the three phases

Table 13. Boundary conditions for the control volume 1D steady state simulation of the Ni-SDC anode

Table 14. Calculated parameters for simulation

1. Introduction

1.1 Motivation

As the wrath of unconventional environmental shifts befuddles mankind, we are forced to ponder about the of self-created global warming dilemma. Since the industrial revolution, the Earth's near surface temperature has increased by 0.6°C on average [1]. With pollution from burning of fossil fuels to provide energy for industries ever rising, emission of gases like carbon dioxide (CO_2) and methane(CH_4) have been increasing inevitably. Research has shown an approximate linear relationship between global warming and aggregate CO_2 emission [2-4].

We as human beings first, and secondly as responsible engineers, need to find solutions to this daunting global warming problem in this age. Otherwise, the future generations, perhaps as near as our grandchildren, will remember us only as a selfish lot, that sucked up all the resources of this planet, without leaving much behind for the future. So we need to shift towards cleaner sources of energy, where we take something from the mother nature and use it as a means of energy without harming the ecological balance of the planet.

For this, renewable energy conversion systems like fuel cells, stand out to be the most viable source of energy. Even though the concept of fuel cell was developed first in 1839 by a British lawyer with a hobby in physics, William Grove [5], the interest in its development and improvement has paced much more in the last two decades [6, 7]. They exhibit high energy density as compared to internal combustion engines and lithium-ion batteries [8]. In addition, fuel cells combine the advantages of both engines and batteries by being mechanically ideal, as the fuel cell doesn't involve any moving parts to produce power.

Despite these several advantages, there are a few disadvantages that are hampering the advancement and complete implementation of the fuel cells in power generating industry. High costs of a fuel cell components is one of the major problems. A simple fuel cell consists of an electrolyte and two electrodes, an anode and a cathode. Till date the platinum (Pt) remains the most efficient electrode (cathode/anode) catalyst material for fuel cells. As of March 2017, the price of Pt is 30.7US\$/g [9]. For this reason, Pt stands right there at the top with other precious metals like gold and silver, and there are no recent signs of its price going down.

Another hurdle is the fuel cost and storage. Fuel cells are electrochemical devices that keep on producing electric power as long as they have a constant supply of fuel. Unlike batteries, which can store energy, fuel cells produce energy only when supplied with fuel. The major fuel source for the most of the fuel cells is hydrogen, which is not an easy fuel to store [10]. Also replacing the existing infrastructure with a hydrogen infrastructure is not being seen as a favorable option in the foreseeable future [11].

This dissertation intends to provide some viable options, by using of technology as well as by unraveling naturally existing resources, to deal with the above mentioned problems. The thesis is, but a small contribution, to play my part in solving the crisis of global warming in this lifetime

1.2 Background Literature Survey

1.2.1. The need for cermet anodes

In an effort to replace noble metals like Pt as electrodes, researchers have been turning towards a relatively cheaper material, with a performance comparable to Pt. In this search, nickel (Ni) is coming out as a preferred alternate material. It is a much cheaper material and costs only 0.0106US\$/g almost 3000times cheaper than Pt [12].

However, the electronic conductivity and catalytic activity of using only Ni is lower than Pt. Hence Ni is almost always used in conjunction with a ceramic, making a cermet anode, where Ni acts as a catalyst and the ceramic provides the framework for ionic conduction to the electrode [13]

For oxide conducting fuel cells, zirconia based electrolytes are an almost automatic choice for researchers [14]. Ni-YSZ (yttria stabilized zirconia) cermet anodes can naturally match the thermal coefficient of expansion of the YSZ electrolyte[15, 16]. Thus providing mechanical stability to the cell at elevated temperatures (800°C ~1000°C), necessary for rapid O²⁻ ion transport through the electrolyte.

However, with hydrocarbon fuels, Ni-YSZ is susceptible to sulfur poisoning [17], and carbon coking [18], which essentially block the triple-phase-boundaries (TPBs) of the fuel cell, where all the electrochemical action takes place. If hydrocarbon fuels are to be used with Ni-YSZ, they must go through rigorous reforming and partial oxidation processes to strip H₂ from the C, and these add to cost and time of the system [19-21].

Ceria(Ce) based Ni anodes are less prone to carbon deposition, hence direct usage of hydrocarbon fuels is possible, which automatically lowers system cost. Since ceria is a mixed ionic electronic conductor (MIEC) [22, 23], its use as an anode can extend the TPB

zone above the electrolyte electrode interface. It is for these reasons that Ni-Ce based anodes can outperform Ni-Zr at intermediate temperature(IT) range of 600°C ~800°C. As will be explained in the next chapters, we will be using carbon as a fuel source for this study, so carbon contamination is a big concern. That is why we chose a Ni-samaria doped ceria(SDC) thin anodes. Also for carbon as a fuel source, all the major action takes place at the anode side. This is the sole reason we worked upon optimizing only the anode side of fuel cell.

1.2.2. Why Thin Film Fabrication

Regardless of the type of cermet used for anode manufacturing, all conventional fabrication methods (screen-printing, tape casting, slurry spraying of the oxides), require sintering of these oxides at high temperature [24-26]. Processes like screen-printing, spraying, require a temperature as high as 1500°C to properly adhere the cermet inter-intra-actively. Also to achieve this temperature in a furnace one requires a substantially long time. Some ceramics are susceptible to poor sintering, which results to poor grain boundaries, hence leads to inefficient TPBs (Fig.1). The thickness control is normally in micrometers(μm) and repeatability is poor.

In physical vapor deposition (PVD) methods like, sputtering and pulsed laser deposition (PLD), we can control the thickness of the deposited structure in nm. Fig. 2 shows a post operation scanning electron microscopic (SEM) image of PLD/Ni-SDC on scandia stabilized zirconia (ScSZ) substrate at room temperature (used in this study). We can see that the anode structure is adhered well to the substrate, without any added high temperature sintering process. Repeatability is exceptional, and we were able to produce almost exact thicknesses in nm range for the same process multiple times.

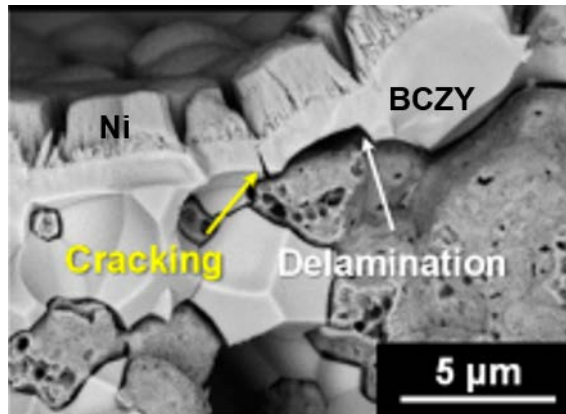


Fig. 1 Post operation SEM image of slurry sprayed BCZY at 1500°C for 2hrs[27]

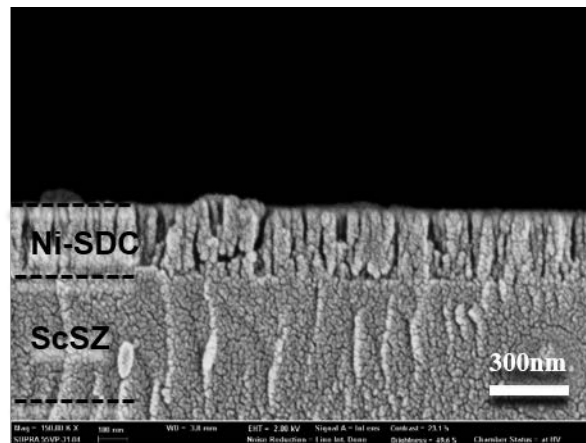


Fig. 2 Post operation SEM image of PLD/Ni-SDC on ScSZ substrate at room temperature

Despite of the above mentioned benefits, in electrode manufacturing via PVD, achieving porosity for gas transport to the TPB, is a problem. For a porous substrate, like anodic aluminum oxide (AAO), achieving porosity with thin film deposition is not difficult. The porosity of the substrate is translated onto the porosity of the structure deposited on top of that substrate. Fig 3, has been taken from a paper by Park et. al [28]. In this paper, the authors showed how the anode morphology changes when the chamber pressure is

increased from 0.67Pa (5mTorr) to 12Pa (90mTorr) for varying thicknesses of the Pt anodes. For thin structures, the porosity is high even at a low pressure. While porosity is low for thicker anodes at low pressure. And sometimes, in severe conditions, we need a relatively thicker anode (still in the same range. i.e. nm) but thick enough to provide the necessary active area for long time, without being consumed. When the sputtering pressure was increased to 90mTorr, even the thicker anodes showed porosity.

However, for dense substrates, the deposition follows the dense behavior of the substrate and it is much more difficult to achieve porosity. Fig. 4 has been taken from a paper by Jung et.al [29]. The authors deposited symmetric Pt structures on either end of a

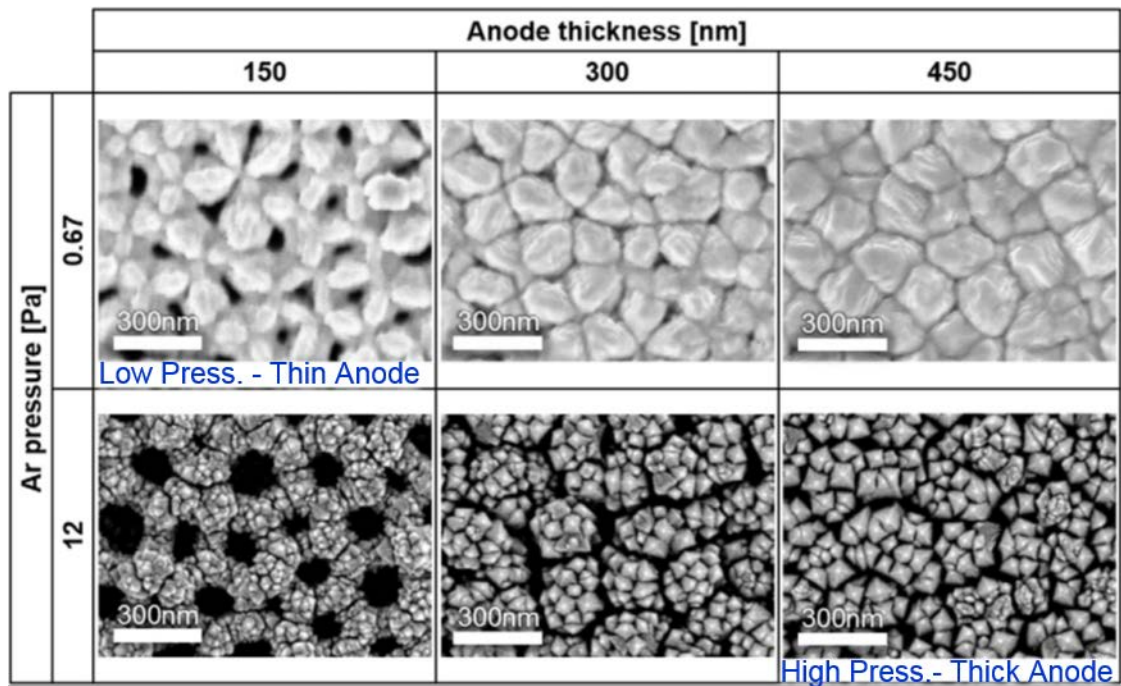


Fig. 3 FE-SEM images of the Pt anode surface morphologies deposited by sputtering on AAO at various Ar pressures [28].

dense YSZ substrate using a mixture of Ar and O₂ reactive background sputtering gases. It can be seen that the films were almost dense until 20% of O₂/(O₂+Ar) reactive mixture gas. Pores, marked by arrows, begin to be appear at an O₂/(O₂ + Ar) ratio of 25%. As the ratio of O₂/(O₂+Ar) was increased, the porosity of the Pt films also increased. All of as-deposited films have the same thickness (~200 nm).

Hence by controlling the pressure and background gas composition of the vacuum chamber, one can make porous structures even with dense substrates, by using thin film deposition techniques.

Another reason for using automated thin film deposition techniques instead of handmade conventional methods, is to improve mass production output. For large scale production, thin film deposition for mass industrial application can lower the ultimate

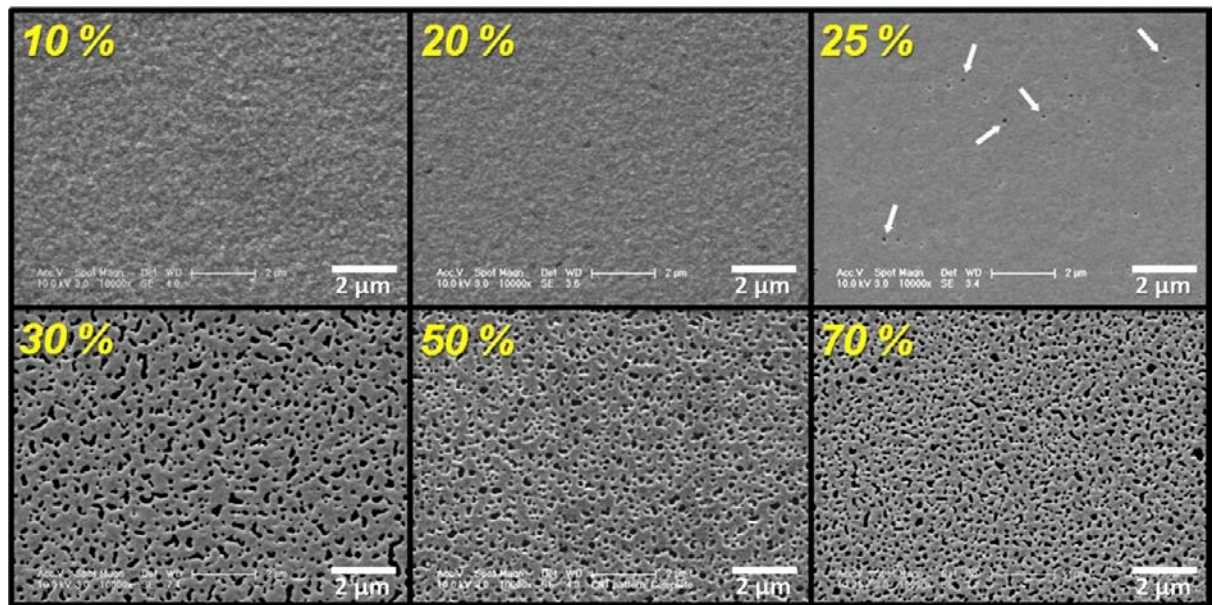


Fig. 4 Scanning electron microscope micrographs of the resulting Pt films as a function of the oxygen ratio, O₂/(O₂ + Ar) utilized during sputtering [29].

production cost and time of a system.

1.2.3. Carbon as a fuel source

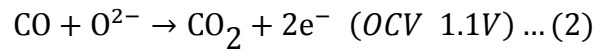
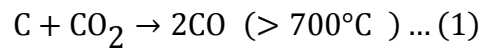
By mass, carbon is fourth most abundant element in the whole universe [30]. On Earth's lithosphere, which is the earth's crust and outer mantle, the carbon content is about 0.032 percent. Upon calculation the total weight of lithosphere by David Smith [31], carbon by weight comes out to be 1.4×10^{23} kg. Also, the human body is almost 18% carbon, so once we die, we become a carbon source too. All in all, it is a very abundant material, whose abundance is always increasing. So to utilize it as a fuel is only natural and humans have been doing it since start of times.

Coal, which is the richest form of carbon, is providing 30% of the energy worldwide according to World Coal Association. Even though efforts have been made for carbon capturing to reduce CO₂ emission [32-34], it is a fact that burning of the coal to produce electricity for power generation is the leading cause of increase in global warming [2, 3].

CO₂ makes 0.04 percent of the Earth's atmosphere according to National Oceanic & Atmospheric Administration (NOAA). Compared to H₂, CO₂ is much easier to store, and we can see them easily in carbonated drinks industries. The use of carbon fuel, directly, or in conjunction with CO₂, not only gives an ethical advantage towards reducing global warming, but also, because of abundance of these substances in nature, it could lead to a much cheaper infrastructure than H₂ infrastructure. And it will not take as much of a reformation time either, because a carbon infrastructure, in one form or the other, already exists in the current system.

The process that utilizes both carbon and CO₂ as a fuel source, it termed as Boudouard Reaction. It was named after Octave Leopold Boudouard, who discovered this reaction in

1905. He utilized direct carbon as a fuel source. In this reaction carbon reacts with oxygen ions from the cathode, conducted through the electrolyte and produces CO₂ in a 4 electrons process. A reverse of this reaction is when the C reacts with CO₂ at an elevated temperature of above 700°C to produce CO (Eq.1). It is a non-electrochemical reaction and is called the reverse boudouard reaction (RBR). This CO from RBR can then be fed to the fuel cell anode, where it meets with the conducted O²⁻ ion transmitted from the cathode via electrolyte, and produce 2 electrons. (Eq.2)



Carbon as an indirect for of fuel via RBR has been used to fuel Ni- cermet anodes by several researchers [35-41], however to our knowledge, the performance of carbon as a fuel on thin film anodes has never been analyzed prior to this research. Now for carbon fuel source, the reaction at cathode and subsequent O²⁻ ion conduction through dense electrolyte is important, but the whole action of RBR takes place at the anode side. This is the reason we have chosen anode optimization only for this study.

In this research we have devised a cheap, easy to fabricate, and efficient system to utilize carbon in its most crude form as an efficient and cheap indirect fuel source for optimal thin film Ni-SDC anode for intermediate temperature oxide conducting fuel cells (ITOFCS).

2. Methods and Materials

The experimental methods used in this paper have already been published in journal of current applied physics by Tanveer et al. [42] that is the author of this thesis, and are reported here again for detailed understanding.

2.1 ScSZ electrolyte support fabrication

We chose the conventional oxygen-ion-conducting 9mol.% scandia-stabilized-zirconia ($\text{ScSZ}:(\text{Sc}_2\text{O}_3)_{0.09}(\text{ZrO}_2)_{0.91}$; China, Beijing) sheets as electrolyte material to fabricate the supporting material for the cells. This doping concentration was previously found to have the highest ionic conductivity at the given temperature range (600°C - 800°C) [43]. These sheets were sent for cutting and subsequent polishing. A 4hr heat treatment at 1250°C was done to remove any impurities adhered to the electrolyte after the machining process. Electrolyte membranes fabricated by this method had a square geometry of $1 \times 1 \text{ cm}^2$ and an average thickness of about $150 \mu\text{m}$.

2.2 LSM/YSZ cathode formation

LSM/YSZ ink (50:50 by wt.% $(\text{La}_{0.80}\text{Sr}_{0.20})_{0.95}\text{MnO}_{3-x} / (\text{Y}_2\text{O}_3)_{0.08}(\text{ZrO}_2)_{0.92}$ FCM: Fuel Cell Materials, Columbus, OH, USA) was deposited onto one side of electrolyte membrane via a screen-printing mesh ($1 \text{ cm} \times 1 \text{ cm}$ Mesh-400; Samborn screen). Up to three layers of ink were brushed on top of one another by subsequently drying each layer at 100°C and then depositing a second layer on top of the first. The layers were sintered at 1200°C for 5hrs in air to minimize the charge transfer resistance at the cathode [44].



Fig. 5 The process of uni-axial pressing of ScSZ powder followed by sintering and machining

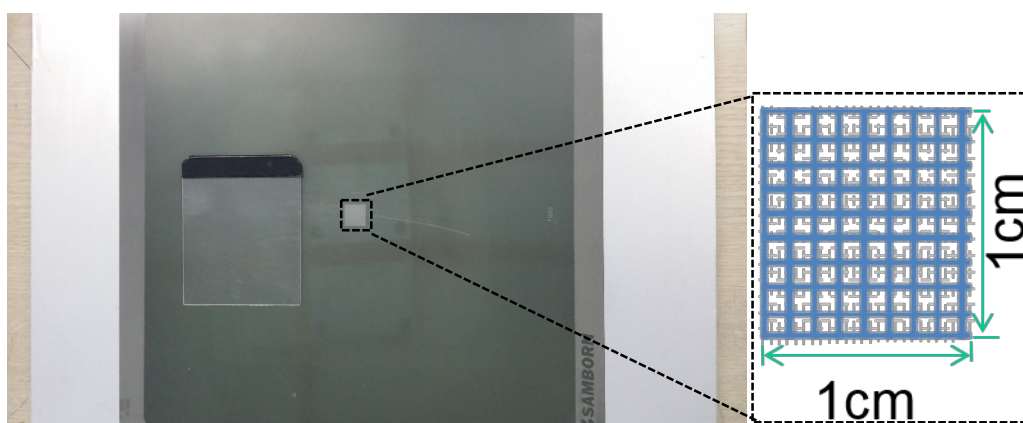


Fig 6 The screen printing board with a hand-made plastic brush. Magnified image shows the dimension and structure of the mesh

2.3 Ni-SDC anode formation

The anode was deposited on the other side of the electrolyte membrane via pulsed laser deposition (PLD) and radio-frequency (RF) sputtering. The target chemical composition for PLD anode was by XRF to be Ni:67.23%, Ce:22.05, Sm:9.8%, by weight. The

deposition was carried out on ScSZ substrate for 1hr. The target was deposited at room temperature and 700°C to analyze the effect of sintering of the target.

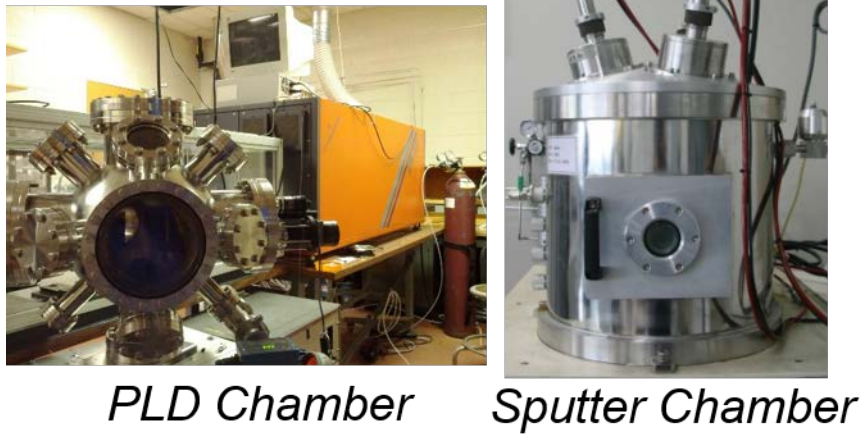


Fig. 7 The physical vapor deposition (PVD) vacuum chambers

In RF sputtering the target used for the anode deposition process was Ni-SDC (50:50 by wt.% nickel-[CeO₂]_{0.9} [SmO_{1.5}]_{0.1}: R&D Korea). The reason for choosing this doping concentration was because this configuration has been reported to give the lowest anodic polarization [45]. The deposition process lasted for 6hrs, at a constant power of 100W, and pressure of the chamber was maintained at 50mTorr. To analyze the effect of reactive O₂ gas on the anode manufacturing process, two different background gases were used during deposition, a) reactive mixture of Ar/O₂:8/2, b) Ar only.

2.4 Cell test setup

The cells were placed inside a test station that has a gold ring with an internal diameter of 0.7cm used to seal the anode compartment from the cathode. A Ni mesh was used as

current collector on the anode side, and a Pt mesh was used as a current collector on the cathode side. The schematic of the cell configuration is shown in Fig. 8. The cell station was placed inside a furnace, where a temperature of up to 800°C was obtained at a ramp rate of 10°C/min. A ceramic rod was placed on top of the center of the test station and sealing was achieved by pressing the gold ring against the anode by rotating a turn screw on top of the ceramic rod. An average pressure of 5kg/cm² was used for effective sealing. The electrochemical surface area of the cell was 0.38cm².

The anode gas used was either H₂ or indirect carbon, while air was used as the cathode gas, with a flow rate of 100sccm for both gases. Cells were tested at 600, 700 and 800°C respectively. The actual temperature of the cells was measured by a thermocouple attached to the top of the cell assembly. Cells were characterized electrochemically by an electrochemical cell test system (1287/1260, Solartron Analytical, Hampshire, England). A VIP plot was constructed at a scan rate of 10mV/sec. EIS measurements were taken at open-circuit-voltage (OCV) for various discharging currents. The impedance spectra were analyzed by a sine wave at an amplitude of 30mV within a frequency range of 0~10KHz.

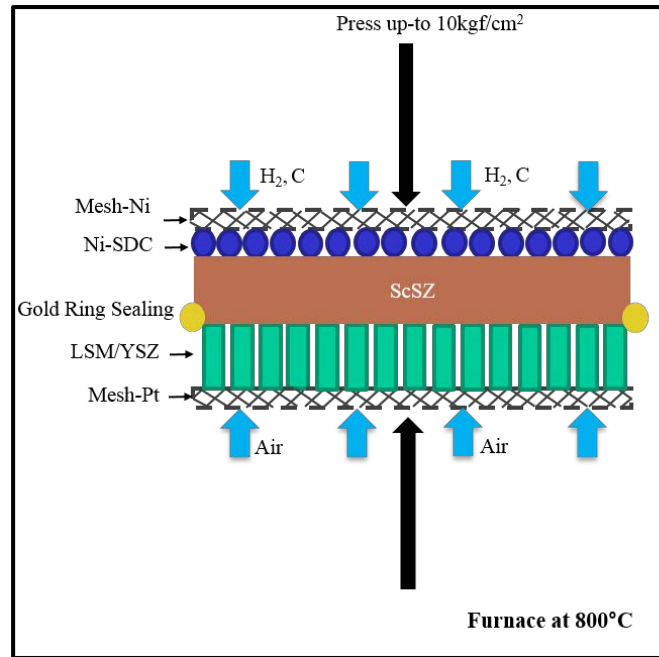


Fig. 8 Schematic of the thin film hybrid fuel cell

Analyses of the data and curve fittings with nyquist plots of the anodic and cathodic resistance of the cells were done with the software packages Z-Plot and Z-View, respectively, for Windows (Scribner Associates Incorporated, NC, USA). The microstructures of thin films were investigated using FIB & FE-SEM (Quanta 3D, FEG, FEI Company, Hillsboro, OR, USA).

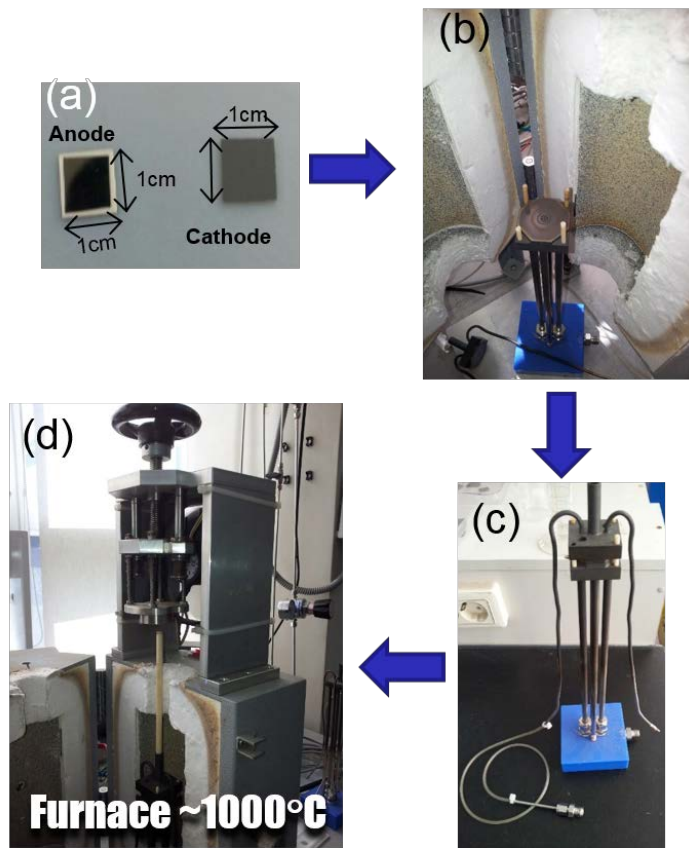


Fig 9 (a) $1 \times 1 \text{ cm}^2$ cell, (b) Test station placed in center of furnace (c) Jig to hold the cell
(d) Ceramic rod attached to turn screw to apply pressure for sealing anode from cathode

gas

3. Thin Film Physical Vapor Deposition of the Nickel Cermet Anodes

3.1 Pulsed Laser Deposition of Ni-SDC

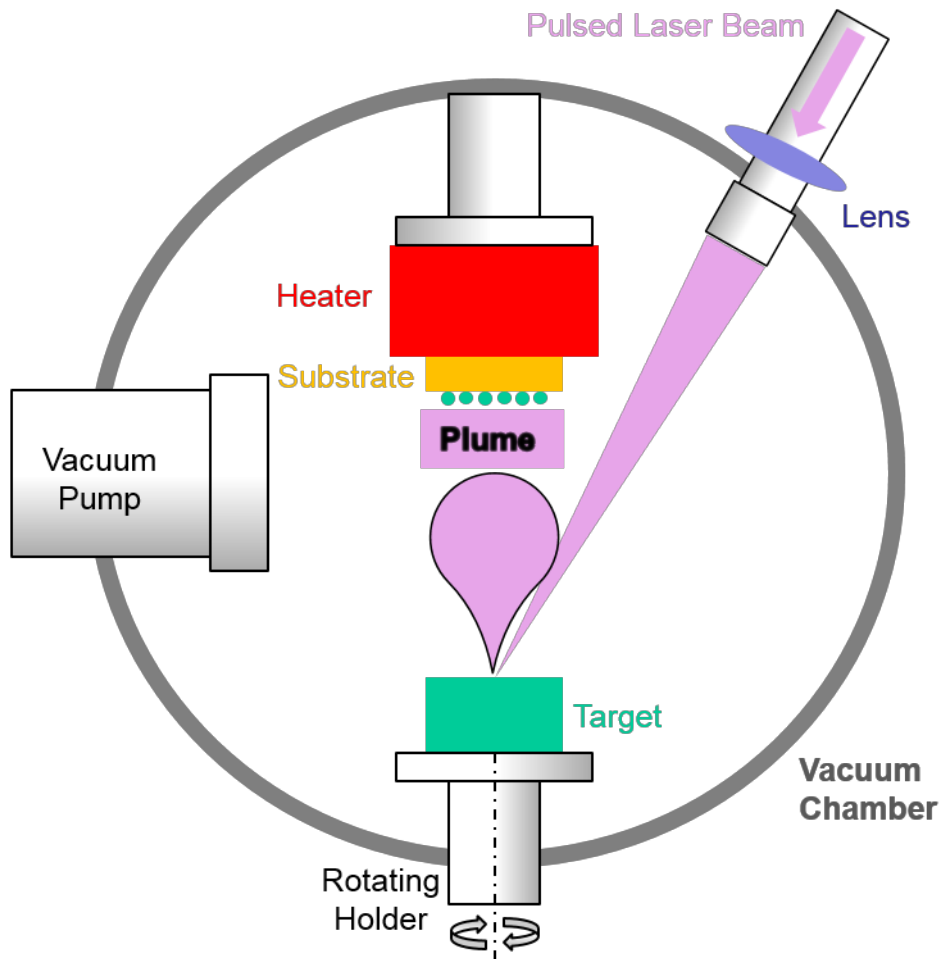


Fig. 10 Schematic representation of pulsed laser deposition process

Pulsed laser deposition (PLD) is a thin film deposition technique based on PVD principle. High-powered pulsed laser beam is directed inside a vacuum chamber to strike a rotating target of the material which is to be deposited. This target material is then vaporized as a result of this high energy strike from the target, and forms a plume, which can normally

be seen as a bright pinkish color. This plume then deposits as a thin film on to the substrate. This process requires an ultra-high vacuum and normally occurs in the presence of a background gas, such as argon, nitrogen and/or oxygen. Schematic representation of the PLD process is shown in Fig. 10.

From plume generation to final film deposition is a relatively complicated process to understand. Researches have tried to put ahead various theories regarding modelling and understanding of the process [46-50]. The whole process can be narrowed down to five basic steps

- 1) high power laser is absorbed on the target surface,
- 2) laser erodes the target material at its surface and generates a plume (ions/electrons and neutrons),
- 3) the plume progresses towards the substrate through the chamber
- 4) deposition of the ablated material on the substrate
- 5) nucleation and growth of the film on the substrate surface

3.1.1. Under the microscope

First a target was deposited on bare Si wafer and sent for characterization. Chemical composition of the target by X-ray Fluorescence (XRF) was found out to be Ni:67.23%, Ce:22.05, Sm:9.8%, by weight %. Table 1 shows the deposition conditions of the Ni-SDC anode on the ScSZ electrolyte for performance analysis, and SiO₂ bare wafer to measure thickness. All depositions were carried out under O₂ pressure of 100mTorr and laser power of 2J/cm² and target to substrate distance was maintained at 6cm.

Table 1. Deposition conditions for the Ni-SDC anodes on ScSZ substrates by pulsed laser deposition(PLD). Target to substrate distance was 6cm

#	Oxygen Pressure	Laser Power	Temperature	Thickness
(1)	100mTorr	2J/cm ²	Room Temp	~250nm
(2)	100mTorr	2J/cm ²	700°C	~250nm

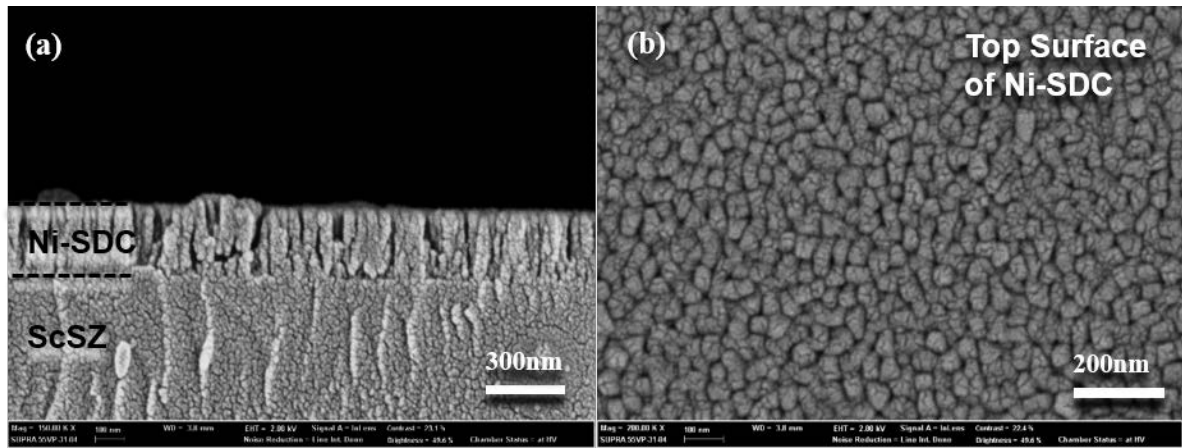


Fig. 11 (a) SEM image of PLD/Ni-SDC on ScSZ substrate at room temperature, (b)top surface SEM of Ni-SDC deposited at room temperature.

One cell was deposited at room temperature (RT) and the other was heated till 700°C at a ramp rate of 10°C /min. After 1hr of successful deposition, both cells were taken for subsequent analysis under the microscope. Thickness of both the films was tested by FESEM. The analysis confirmed that the temperature had no effect on the anode thickness, when deposited with PLD. Both showed a remarkably fast growth rate of nearly 250nm/hr.

Fig. 11 shows an SEM image of the PLD/Ni-SDC anode. Both anodes had relatively

similar structure. It can be seen that the Ni-SDC is adhered well with the ScSZ electrolyte in Fig. 11(a), and has a uniform columnar growth on top of a dense zirconia based substrate, which was remarkable. Also the porosity, which is a necessary feature of an electrode was well observed in the Fig. 11(b). Hence on a microscopic level, PLD served as a satisfactory thin film deposition method.

3.1.2. Performance

Now the cells made at the two PLD target temperatures were applied to the test at the test station mentioned in section 2.4. The results of the test are shown by voltage-current-power (VIP) curves in Fig. 12. The first thing to notice was that the open-circuit-voltage (OCV) for both the types of cells was almost same, however there was a marked different between peak power density of the two cells. For the cells produced with a Ni-SDC anode at room temperature, the peak power density at 700°C was no more than 5mW/cm². The peak power density at the same conditions for a Ni-SDC anode deposited at 700°C target temperature, was 52mW/cm², about 10 times higher than the ones deposited at room temperature.

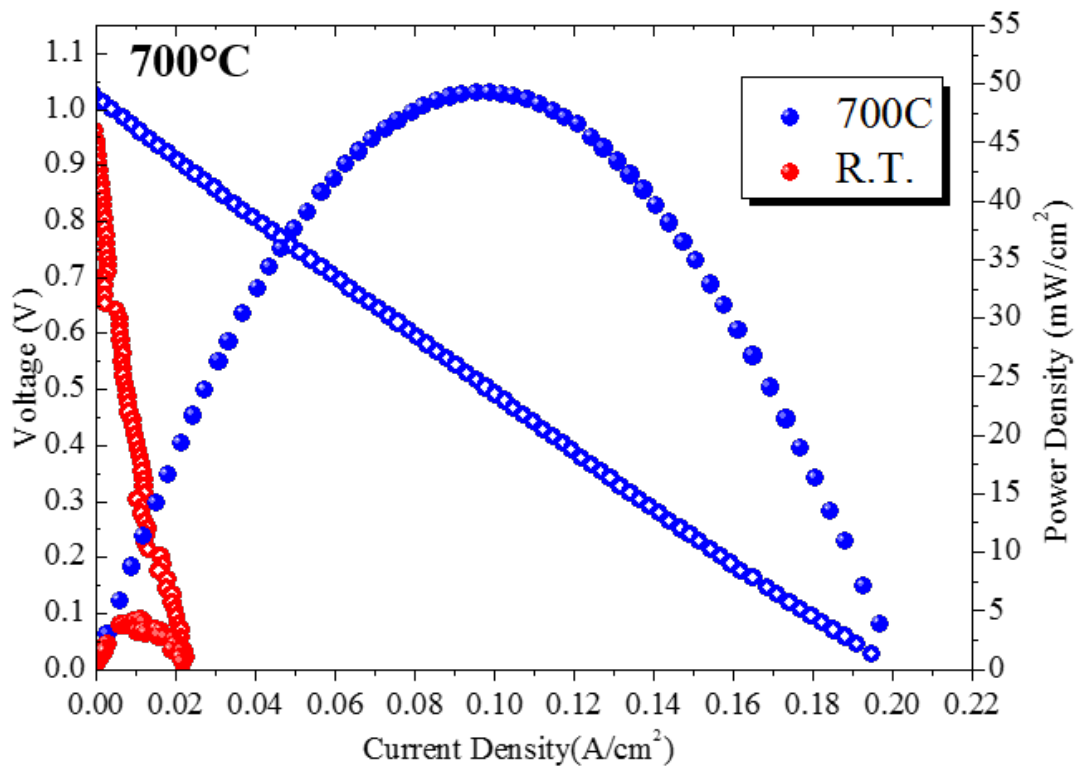


Fig. 12 Peak Power density comparisons of PLD/ Ni-SDC anode cell fabricated at different temperatures

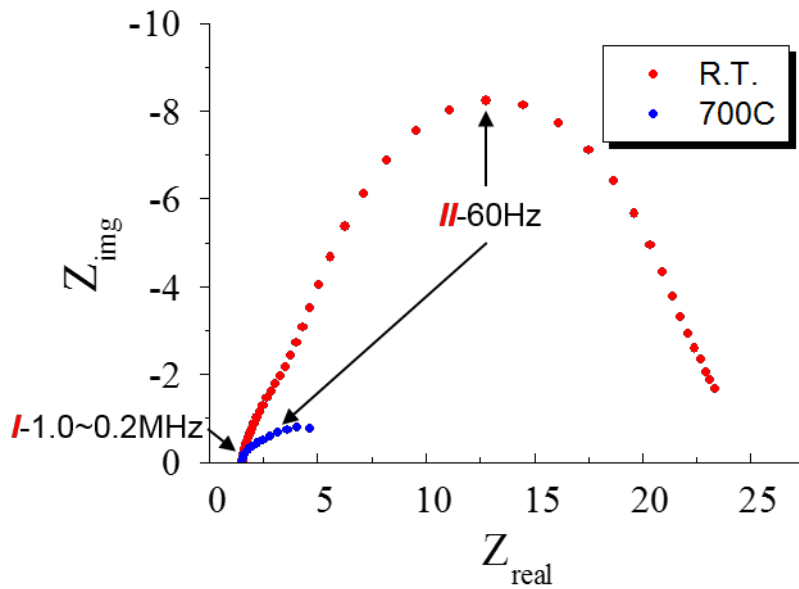
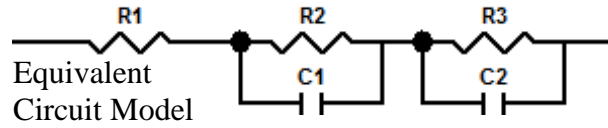


Fig. 13 EIS measurements of the PLD/ Ni-SDC anode cell fabricated at different temperatures

Table 2 Resistances measured by curve fitting of the nyquist plots from Fig.12



Temperature	$R\Omega$ (ohm-cm ²)	R_I (ohm-cm ²)	R_{II} (ohm-cm ²)
25°C	2.7	0.8	20
700°C	2.4	0.45	5

Now we wanted to see the resistances of the measured cell. Fig.13 shows the electrochemical impedance spectroscopy of the two cells. Two distinct peaks were visible for both the cells. One at high frequency, around 1MHz and other at low frequency of about 60Hz. On an ideal electrochemical circuit, the x-intercept owes to the electrolyte ohmic loss, the first semicircle at high frequency is related to anode activation loss, while the one at low frequency range is related to the cathode activation loss [51].

We can model the electrochemical processes of the fuel cell in form of circuit elements. Table 2 shows an equivalent circuit model of the EIS plots from Fig. 13. R_I is the ohmic resistance, straight off from the electrolyte. It is almost identical for both cells at the measuring temperature, since both cells have the same thickness of electrolyte. The remaining two resistances were modelled using a capacitor in parallel to the resistance, to represent the electrochemical behavior of the anode and the cathode. Since cathode is the same for all cells, the main electrode creating this difference in impedances is anode, and is the reason for shifts in performances.

3.1.3. X-ray diffraction analysis

Since there was a heating of targets involved, it was suspected that the crystallinity of the deposited substances may be something to look at. Fig. 14 shows the X-ray diffraction analysis (XRD) of the two cells before reduction by H_2 in the cell tests. Both of these depositions were done on bare Si wafer, so Si peaks are visible for both cells. For room temperature deposited PLD/Ni-SDC there was no peak seen for either NiO or SDC. While the red-line peak for the Ni-SDC deposited at a target temperature of 700C shows distinct SDC(111) and NiO(200) peaks at around 29° and 47.5° respectively. Whatever the Ni-SDC is present in the Ni-SDC deposited at room temperature is not crystalline. Similar results were shown by Noh et al. [52] where authors deposited Ni-YSZ at different target

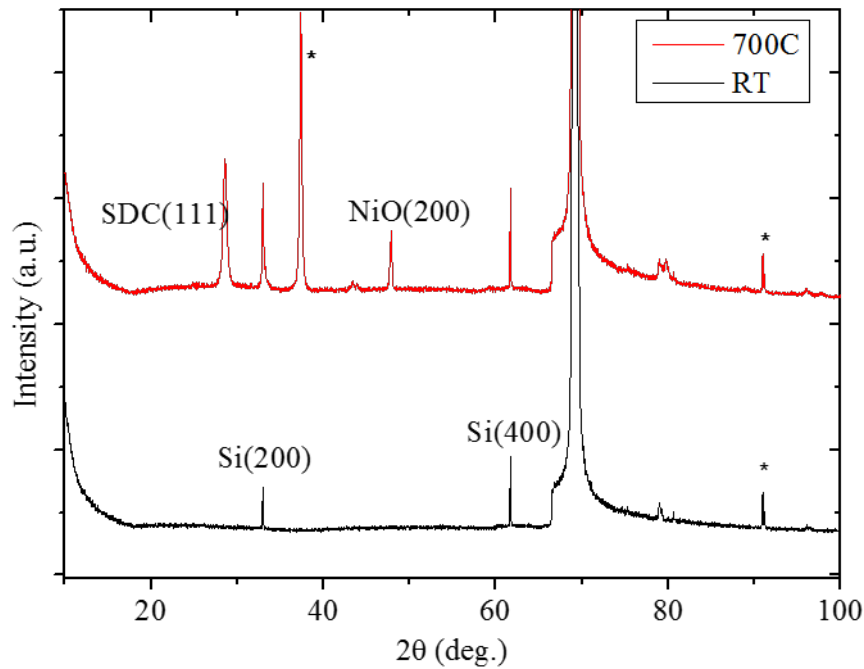


Fig. 14 XRD measurements of PLD/ Ni-SDC pre-operation, non-reduction anode cell fabricated at room temperature and 700°C. (*) marks the unidentified peaks.

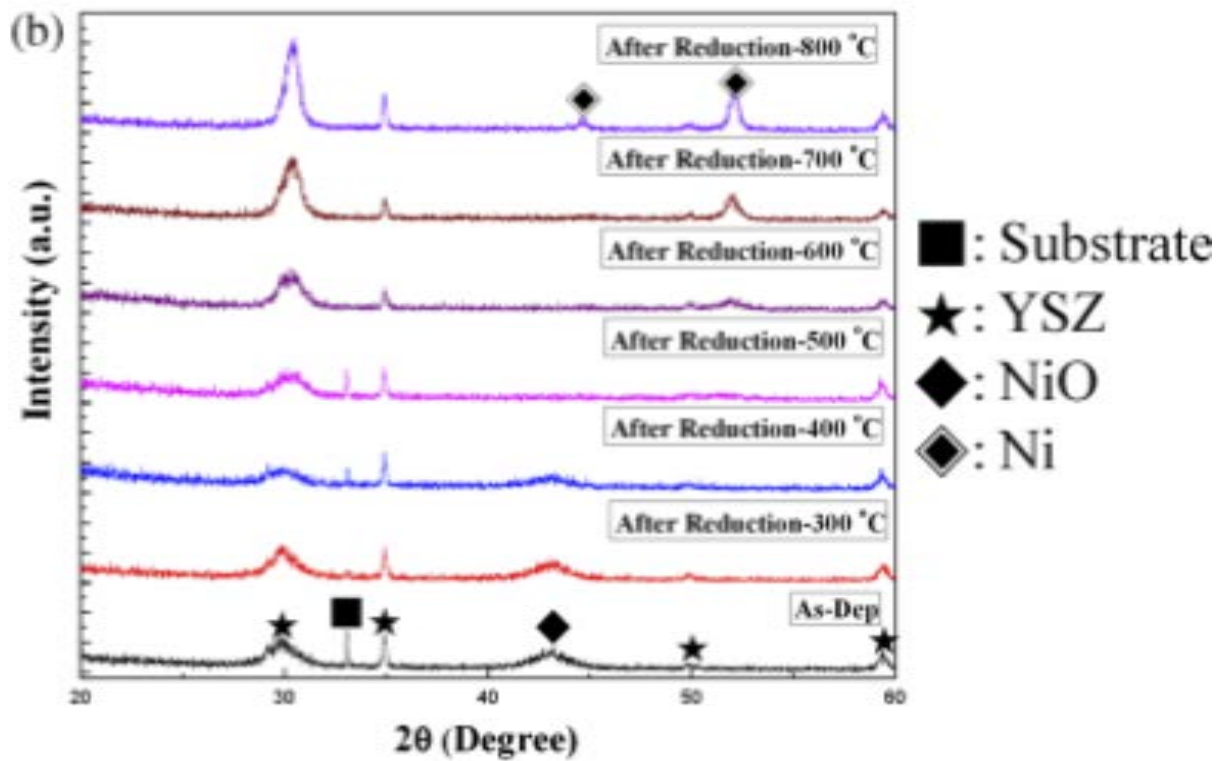


Fig. 15 XRD measurements of PLD/ Ni-YSZ anode at various temperatures after reduction in H₂ atmosphere by Noh et al. [52]

temperatures and their XRD was measured post H₂ reduction (Fig. 15). One can see that the Ni and YSZ content keeps on increasing as the temperature is increased from room temperature up to 800°C. This means that in order to deposit a well performing crystalline anode, one needs high temperature sintering of the anode during deposition, to get the required thin-film anode characteristics.

3.1.4. EPMA analysis

As no Ni-SDC could be detected by the XRD for the Ni-SDC deposited at room temperature, we wanted to check whether we actually could detect any Ni or SDC from

other methods. Electron Probe Micro Analyzer (EPMA) was used to detect the average count and distribution of the constituent materials making up the cermet anodes.

Fig 16 shows the top view EPMA analysis of the Ni-SDC PLD anodes. Fig 16 (a)&(b) are the pre-operation images. One can see that the Ni count is much larger in the 700°C Ni-SDC PLD anodes. The average count for Ni is 20 compared to only 5 for a given area of observation of $625\mu\text{m}^2$. Similarly, the count for samaria (Sm) and ceria (Ce) was also considerably lower for the anodes deposited at room temperature. This could be the main cause of the poor performance shown in Fig 12, and high impedance measured in Fig 13

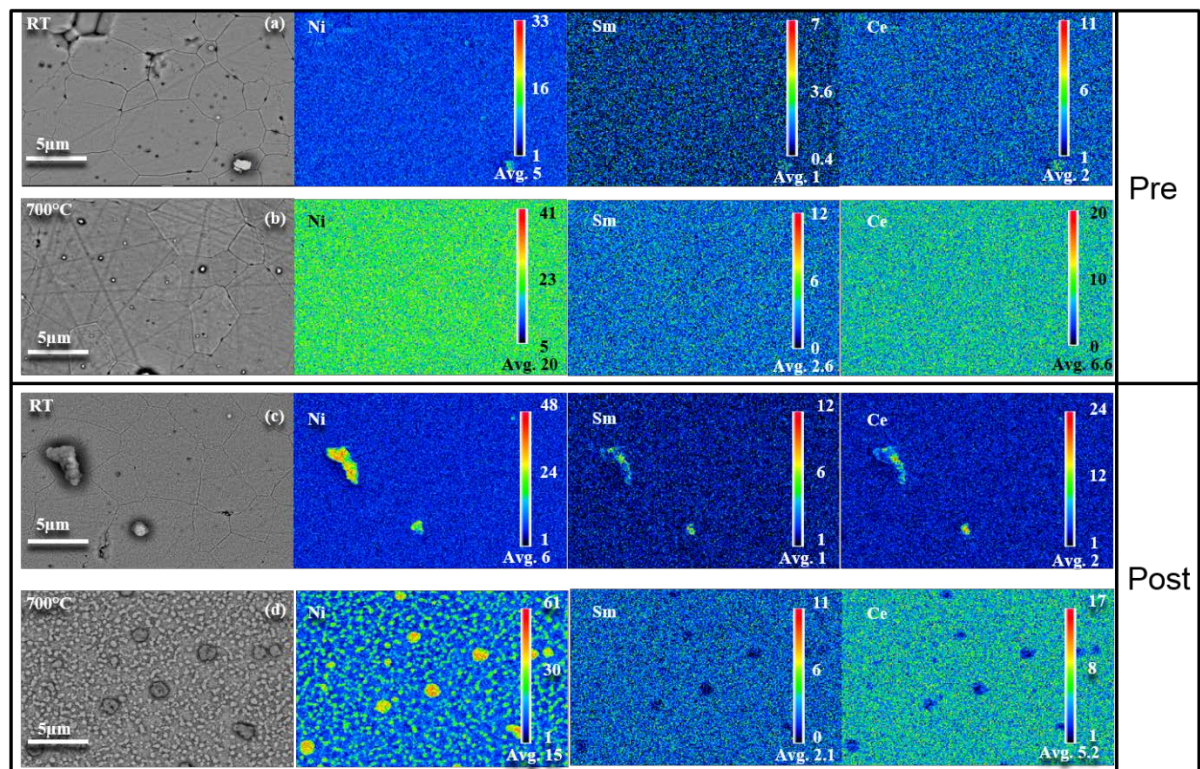


Fig. 16 Electron Probe Micro Analysis (EPMA) of PLD Ni-SDC anode, (a)&(c) pre- and post-operation, of anodes deposited at room temperature, (b)&(d) pre and post operation of anodes deposited at 700°C.

for room temperature deposited Ni-SDCs. Fig 16 (c)&(d) show the post operation analysis of the two anodes. Clear agglomerated Ni particles are visible for the anodes deposited at 700°C while Ni is only slight agglomerated at certain spots and the average count of Ni remains the same.

This means that for a PLD –Ni-SDC, one needs high temperature sintering of the target material to attain the necessary deposited anode properties. However, the core idea of shifting towards a thin film deposition technique in this paper, is to remove high temperature sintering methods that consume both time and resources. So it was concluded that PLD is not the suitable technique for deposited thin film anodes. We had to look for other options.

3.2 Sputtering of Ni-SDC thin film anodes

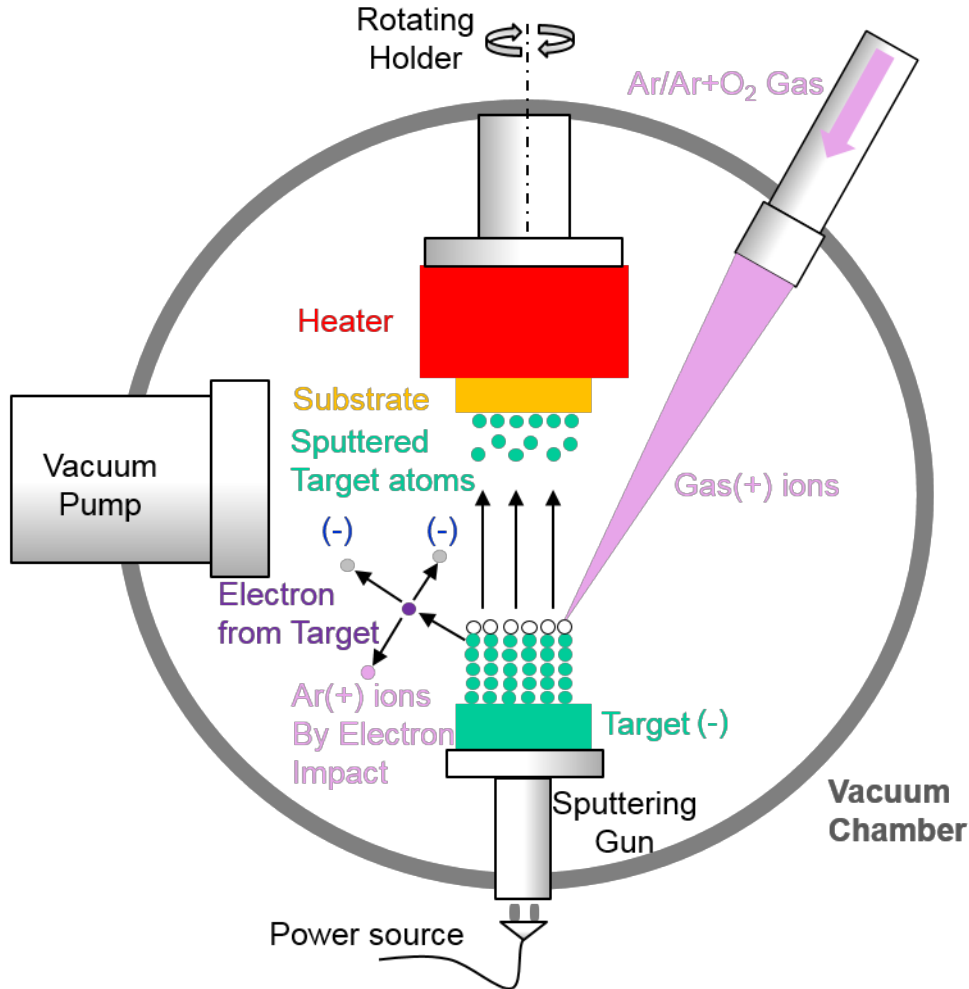


Fig. 17 Schematic Representation of the sputtering process

Sputtering is a thin film deposition technique based on the principle of collision of particles. Atoms are knocked up and ejected from a solid target (normally a metallic oxide or processed metal). Although sputtering is a very mature process these days, its history dates back to early 19th century where there first patents were filed [53-55].

Sputtering usually results smaller grain size than PLD, but larger than atomic layer

deposition. It shows similar adhesion to the substrate as PLD. A variety of different grain orientations can be achieved by using different types of sputtering. Various types of sputtering depending upon the power source

- 1) Direct Current (DC)
- 2) Radio Frequency (RF)
- 3) Magnetron, where usage of magnetic fields is done to control electron motion
- 4) Ion Assisted

We used RF sputtering source in our research. The schematic of which is shown in Fig. 17. This setup has a rotation unit to rotate the substrate, in order to give maximum exposure to all areas of the substrate. Target to substrate distance was 7.5cm. RF sputtering is normally used to sputter insulated targets, and has a lower deposition rate than the DC sputtering. However, it has been found that RF deposited films have a better stoichiometric reproducibility [56], and this is what we require for a repetitive thin film process.

3.2.1. Under the microscope

First a target was deposited on bare Si wafer and sent for characterization. Chemical composition of the target by X-ray Fluorescence (XRF) was found out to be Ni:50%, Ce:46%, Sm:3.6%, by weight %. So in essence the Ni concentration for this target is lower than the PLD target.

As mentioned in section 1.2.2, one needs to have a proper background gas with certain content of O₂ with Ar to achieve the necessary porosity for a thin film electrode deposition. I deposited various Ni-SDC anodes on ScSZ substrate at room temperature for 1~5hrs under Ar and Ar/O₂:80/20. The deposition conditions are explained in Table 3. The

Table 3. Deposition conditions for the Ni-SDC anodes on SSZ substrates by RF sputtering

#	Chamber Pressure	RF Power	Temperature
Ar/O ₂ :80/20	50mTorr	100W	Room Temp
Ar	50mTorr	100W	Room temp

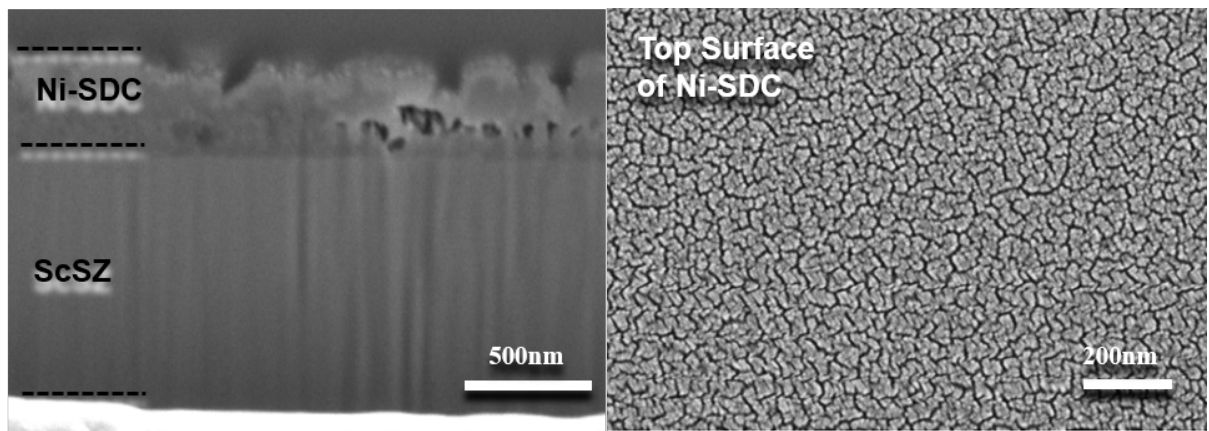


Fig. 18 Post operation SEM of sputtered Ni-SDC on ScSZ substrate at room temperature at Ar/O₂:80/20 reactive sputtering gas& Top surface SEM of Ni-SDC deposited at room temperature.

thickness varied with the deposition time.

Fig 18 shows the SEM image of the Ni-SDC anode deposited on the ScSZ substrate. We can see uniform granular structure of about 250nm with good adherence to the electrolyte. The second image in Fig. 18 shows the top view of the Ni-SDC anode. We can see that it is moderately porous structure and the arrangement of the surface is quite different from the PLD structure shown in Fig. 11. The thickness of the Ar/O₂ deposited

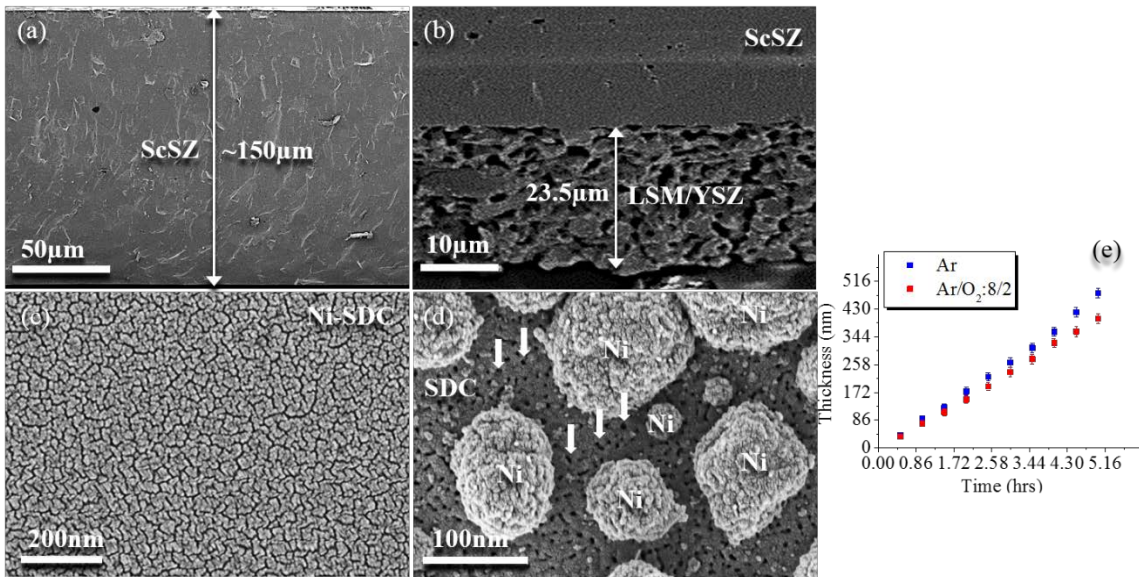


Fig. 19 SEM image of (a) ScSZ electrolyte support (b) microstructure of LSM/YSZ cathode, (c) top view of the Ni-SDC anode made by reactive sputtering (Ar/O₂:8/2), pre-operation (d) high-resolution SEM image of the same anode after cell test at 800°C in H₂ (e) growth rate comparison of the anodes with time

anode was slightly lesser than the Ar only deposited, but nothing significant to report about. The structure was more or less the same.

From here on the results and discussions are taken again from the author's published work in journal of current applied physics [42], are forwarded here to explain the scope of work presented in this thesis, more elaborately. Fig. 19(a) & (b) are the FE-SEM images of the micrometer scaled electrolyte and the cathode respectively. Fig. 19(a) shows that the ScSZ electrolyte support layer was dense and approximately 150 µm thick. Fig. 19(b) shows that the LSM/YSZ cathode consistently adhered to the electrolyte surface and the three-layer screen-printing process resulted in an average thickness of about 20 µm. Fig. 19 (c) is a pre-operation top-view of the Ni-SDC anode made by reactive sputtering. The porosity

of the anodes could not be clearly calculated by this image for both anodes. Fig 19(d) shows the high-resolution SEM image of the same anode after 1hr of heat treatment at 800°C under H₂ atmosphere. Such high temperature reduction results in a) agglomeration of Ni [57], which can be seen as bright balls above the dark grey SDC framework, b) loss of the oxygen from the Ni-O-SDC, resulting in nano-porous Ni-SDC anode. Pores are indicated by white arrows and average pore size was calculated to be around 3.5nm on average.

Fig.19 (e) shows the growth rate comparisons of both anodes. Anode thickness increased linearly with increase in sputtering time, however the growth rate of films sputtered with Ar/O₂:80/20 reactive gas, was 20% slower than the ones sputtered with Ar only. We confirmed a similarly decreased growth rate on average for Ar/O₂:80/20 sputtered Ni-SDC anodes in about 5 samples consistently. This means that the O₂ in the reactive gas mixture is somehow retarding the growth rate of Ni-SDC anode films. A similarly lower growth rate was found by other researchers while using O₂ reactive sputtering gas while depositing thin metallic films [58].

3.2.2. Performance Comparison

Fig. 20 shows the polarization and power density curves of the two cells at 600,700 and 800°C. As expected, the cell power density and current density increased with an increase in the temperature due to the increased reaction kinetics of fuel cells at higher temperatures. The cells showed an OCV of about 1.05V at 600°C, and when the temperature was raised to 800°C, the OCV decreased by 5%, which is consistent with the reversible voltage variation with a change in the temperature as noted in the literature [59].

Peak power densities for Ar/O₂ sputtered anode cells were 150mW/cm², 75mW/cm²

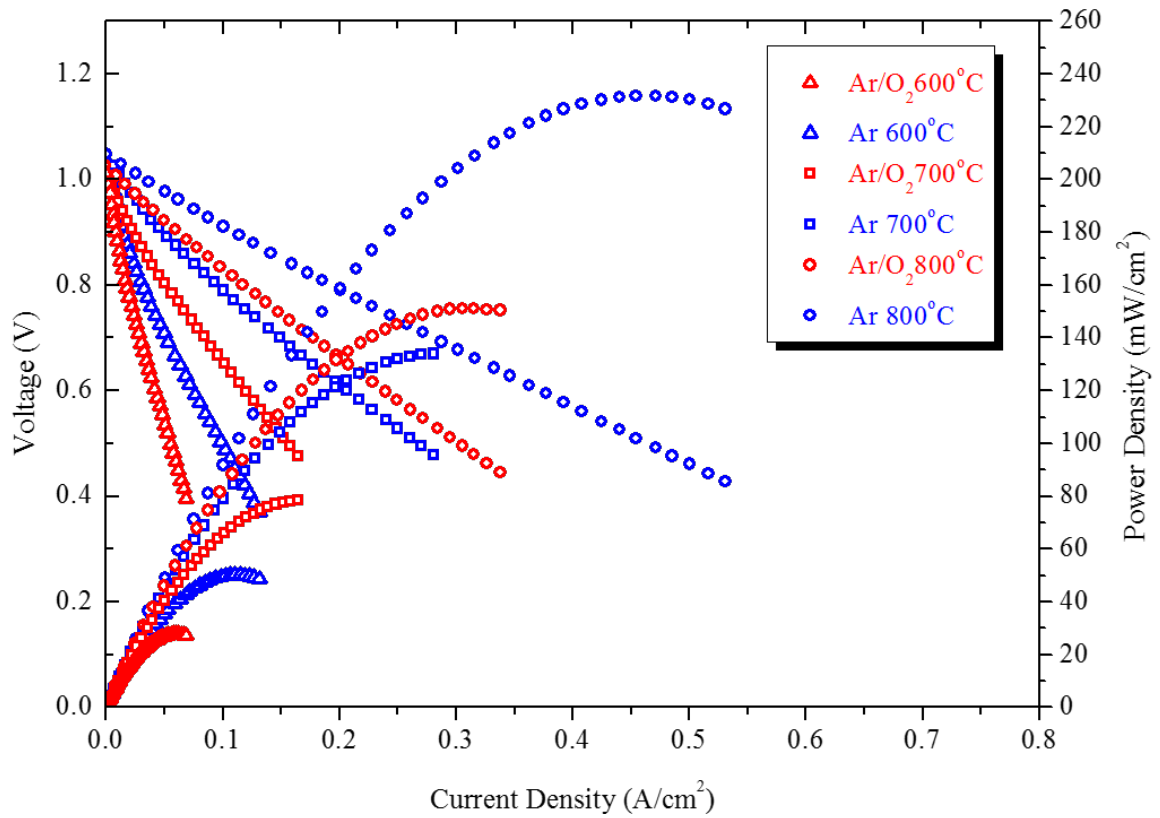


Fig. 20 Polarization curves for cells, having reactively (Ar/O₂:8/2) and non-reactively (Ar only) sputtered Ni-SDC anodes, at various temperatures.

and 25mW/cm² at 800°C, 700°C and 600°C respectively. Peak power densities for Ar only sputtered anode cells were 240mW/cm², 140mW/cm² and 50mW/cm² at 800°C, 700°C and 600°C respectively. These results show that the performance of Ar/O₂ (reactively) sputtered anode cell is almost half of the cell with Ar only sputtered anode.

3.2.3. EIS Characterization

In order to investigate the cause of this performance variation, we turned towards impedance measuring techniques. Fig. 21 shows the EIS of the cells at above mentioned

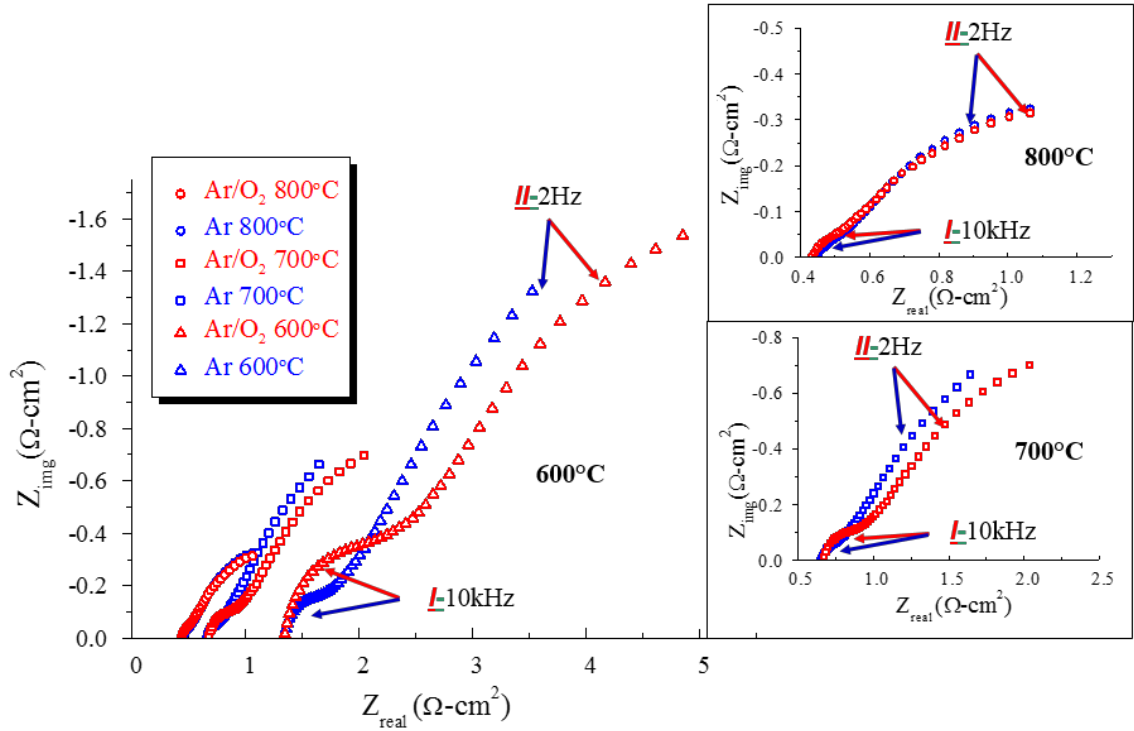


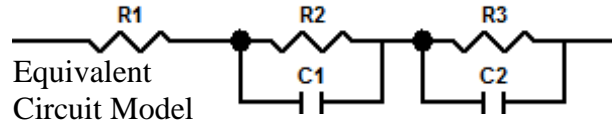
Fig. 21 Electrochemical impedance spectroscopy (EIS) analysis of the cells, having reactively (Ar/O₂:80/20) and non-reactively (Ar only) sputtered Ni-SDC anodes, at various temperatures.

temperatures. The inset shows a magnified view of both cells at 700°C and 800°C. Two major curves can be seen in this figure. The one corresponding to a higher frequency is related to the anode activation loss, while the one corresponding to a lower frequency range is related to activation losses on the cathode side [51]. Since the cathode sides were identical in both cells, the cells have the same semicircle diameter at a low frequency of 2Hz, at a given temperature. There is however a marked difference in the anode activation loss, the semicircle at a high frequency range of 10KHz, between the two cells. At a temperature range of 600°C-800°C, it can be seen from Fig. 21 that the anode activation loss semicircles for the cells with a reactively (Ar/O₂) sputtered anode are significantly larger as compared

to those with a non-reactively (Ar only) sputtered anode.

For a clearer perspective we calculated the exact values of the anode and cathode resistances by drawing an equivalent circuit model of the cells. These values were obtained by the curve fitting of the EIS plots from Fig.21 and are shown in Table 4. The circuit model consists of the electrolyte ohmic resistance R , attached in series to the anode and the cathode polarization resistances of R_I & R_{II} . The impedance behavior of the electrochemical reaction at the anode and cathode is represented by the double-layer capacitance constant-phase element (CPE), parallel to the respective electrodes. Table 4 shows that the anodic over-potential is increased in the case of reactively sputtered anodes. Reactively sputtered anodes showed an over-potential value almost twice that of the non-reactive ones. While cathode over-potential values were almost similar for both cells. Since cathode and electrolyte are same for all cells, we can conclude that the low peak power density in case of reactively sputtered anode cell, seen in Fig.20, is primarily related to the increased anodic over-potential seen in Fig.21, and calculated in Table 4 for these cells.

Table 4. Resistance values at the anode and cathode of the two cell types obtained via curve fitting of EIS plots from Fig.20.



Furnace Temperature	Anode Type	R/ (ohm-cm ²)	R// (ohm-cm ²)
600°C	Ar	0.67	9.21
	Ar/O ₂ :80/20	1.40	9.45
700°C	Ar	0.28	2.68
	Ar/O ₂ :80/20	0.55	2.72
800°C	Ar	0.08	1.77
	Ar/O ₂ :80/20	0.14	1.83

Table 5. XPS analysis of the RF sputtered Ni-SDC anodes

#	Ce3d	Sm3d	Ni2p	O1s	C1s
Ar only	15.49%	5%	25.05%	54.02%	0.44
Ar/O ₂	18.6%	6.14%	18.91%	55.24%	1.11

3.2.4. XPS analysis

The XPS analysis of both anodes has been shown in Table 5. It was revealed that both methods produced a slightly different composition of Ni-SDC anodes. There was especially a marked difference between the Ni percentages for both methods. Ni content

was higher in the case of Ar only sputtered anode as compared to Ar/O₂:80/20 sputtered ones. The Ni in Ni-SDC provides the catalytic and electronic conductivity while Sm doped Ce is responsible only for providing the structural framework to the cermet anodes [60, 61]. Low atomic percentage seen in XPS for the catalytic Ni could be the reason for increased over-potentials (Fig.21) and reduced performance (Fig.20) for reactively sputtered anodes.

A comparison between XPS binding energy peaks for the two anodes before and after the electrochemical evaluation has been shown in Fig.22. Fig.22 (a)&(b) shows the nickel binding energy peaks before and after characterization respectively. Two distinct peaks are visible for both reactively (Ar/O₂) and non-reactively (Ar only) sputtered anodes. The first (minor) peak in Fig.22 (a) is closer to the theoretical value for Ni⁰ (metallic) and second (major) peak is more relatable to Ni²⁺ (oxidized) theoretical value for both anodes [62].

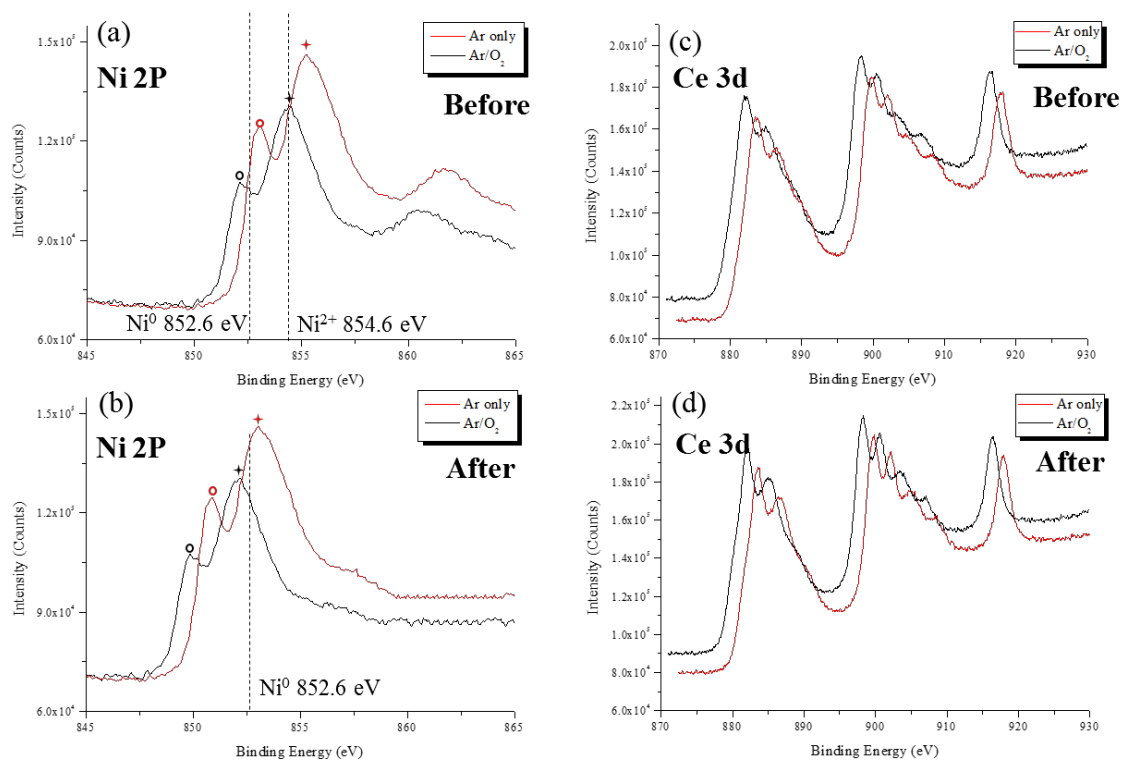


Fig. 22 Ni2P XPS spectra of the two anodes before (a) and after (b) electrochemical evaluation, (The dashed lines are peak values of Ni²⁺ and Ni⁰ in theory), Ce3d XPS spectra of the anodes before(c) and after (b) electrochemical evaluation

This shows that both metallic and oxidized Ni phases were present in the two anodes. Fig.22(b) shows that after cell test, the major peak for both anodes shifts towards the metallic Ni (Ni⁰) region, which is understandable under reducing anodic conditions (100sccm of H₂ @ 600-800°C for 12hrs), while the minor peak shifted to even lower values compared to pure phase Ni. There was no distinct change seen in the intensity of the peaks.

Fig.22(c)&(d) shows the ceria binding energy peaks before and after characterization respectively. Normally in Ce, six distinct peaks can be seen due to multi-electron

interaction [63]. All the peaks seen in Fig.22(c)&(d) can be attributed to Ce^{4+} oxidation state. After electrochemical measurement, no shift in binding energies for the respective peaks was found. One of the shortcoming for using Ceria based anodes is the partial oxidation of Ce^{4+} to Ce^{3+} which can lead to mechanical issues as a result of lattice expansion. This lattice expansion can cause the electrolyte and electrode interface to delaminate [64], thereby sabotaging the triple phase boundaries and life-time of the cell. No such problems are found in our cell, which can mean that the cell can perform for longer periods than a conventional method deposited anode. However, the intensity of the peaks increased by a factor of 10^4 on average. Nonetheless a change in the valence state of the ceria was not found.

3.2.5. EPMA analysis

Fig.23 shows the EPMA images of both anodes before and after cell tests. The first image in each row shows a back-scattered image of Ni-SDC anode, while remaining images in the same row show the average count of the detected materials, Ni, Sm, and Ce, for that anode. From Fig.23(a)&(b), we cannot see a significant difference in the Ni distribution in the cermet anodes made by both methods. However, the average count of the detected Ni is higher in the case of Ar only sputtered anodes. This result is consistent with the XPS results showed in Table 5.

Another important aspect is that even though the constituent target Ni distribution was lower in case of sputtering as compared to PLD the deposited films showed a remarkably higher Ni content for sputtered Ni-SDC films. Average count for both Ar/O₂:80/20 and Ar was 25 and 40 counts per given area of $625\mu m^2$.

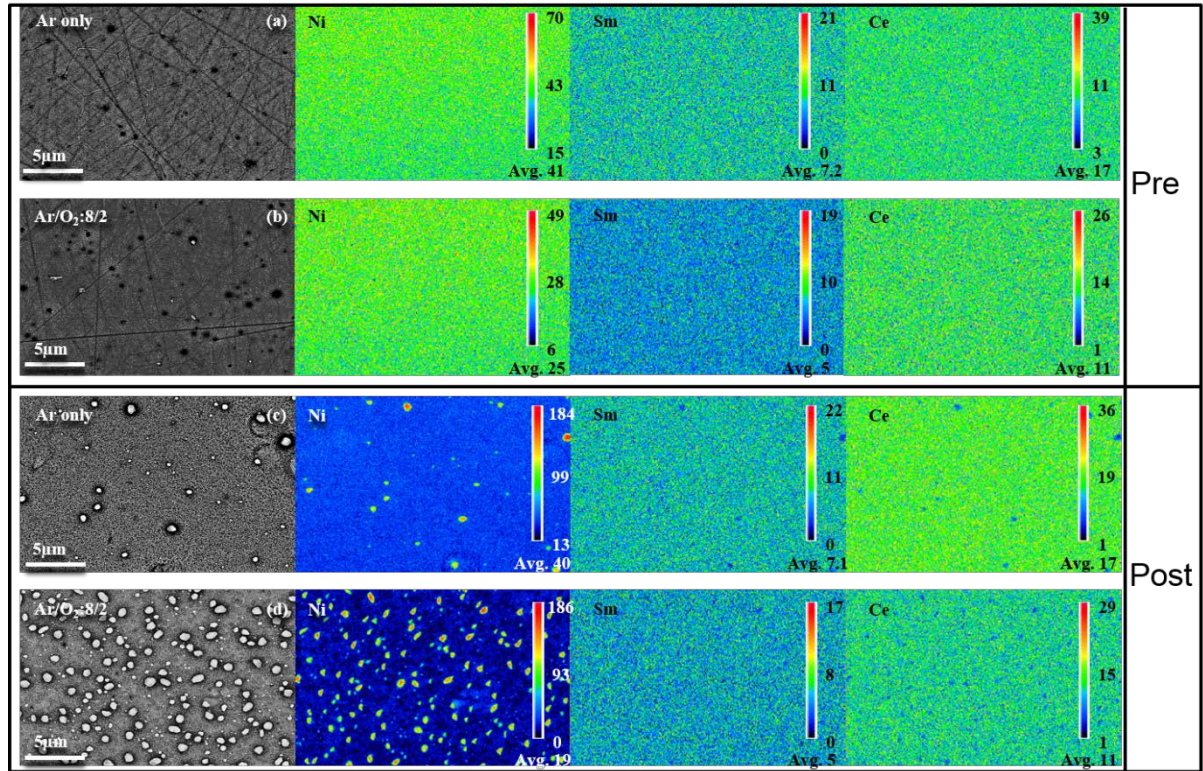


Fig. 23 Electron Probe Micro Analysis (EPMA) of Ni-SDC sputtered anode, (a) pre-operation Ar only, (b) pre-operation Ar/O₂:8/2, (c) post-operation Ar only, (d) post-operation Ar/O₂:8/2.

Post operation images , Fig. 23(c)&(d) show significantly higher counts of Ni for both anodes. This can be because the Ni-O has now been reduced to metallic agglomerated Ni and is more clearly detectable. Interestingly, the average count of the Ni still remains the same for Ar only sputtered anodes, while the average count of Ni drops from 25 to 19 in the case of Ar/O₂ sputtered anodes.

The results from Fig.22 and Fig.23 clearly indicate that both metallic and oxide phases of nickel were present in the two anodes, which get reduced to clustered metallic Ni, post operation. For Ar/O₂ sputtered anodes the clusters of Ni appear much more pronounced,

both in number and the size. Sm and Ce remain unaffected at this high temperature and reducing condition.

3.2.6. Anode Lifetime

Another factor in the manufacturing electrodes for IT-SOFC applications, is their effective lifetime. Fig. 24 shows the SEM top view of the Ni-SDC anode, before and after 12hrs of electrochemical operation, manufactured by both methods. From the pre-operational image, Fig.24(a)&(c) we cannot see any distinct difference in the microstructure between the two electrodes. Fig.24 (b) & (d) show the post operational SEM

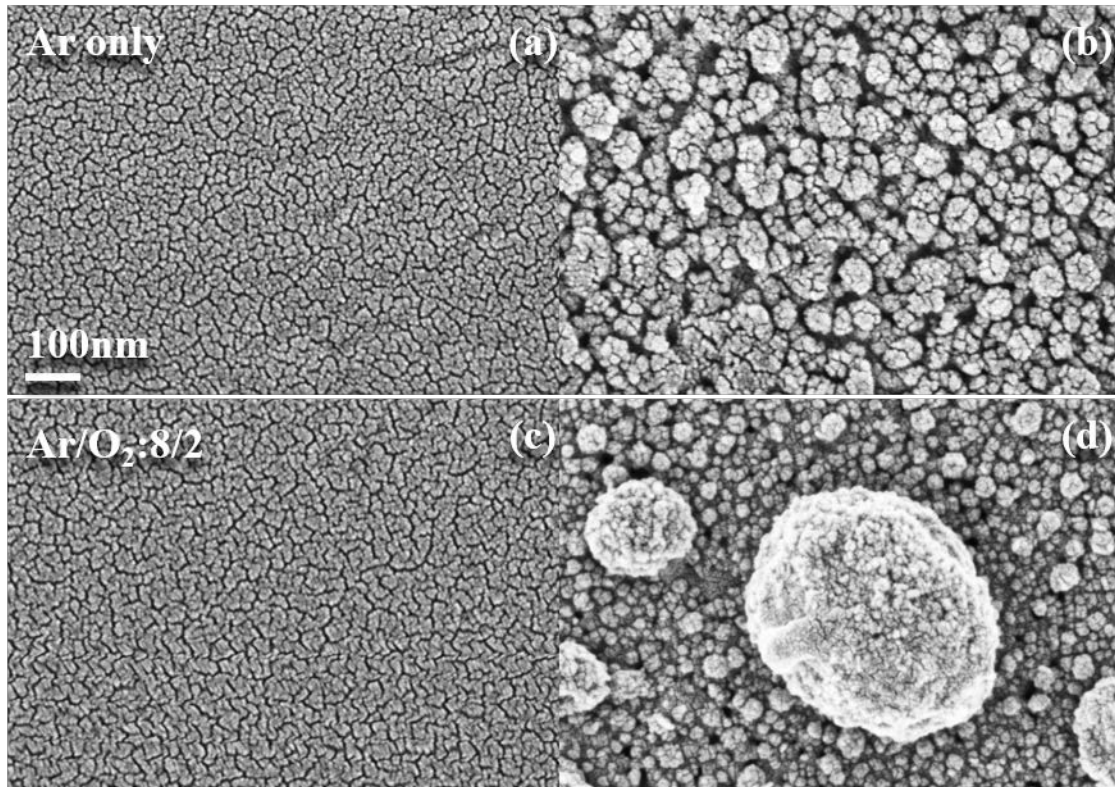


Fig 24 (a)&(c) Pre-operation (b)&(d) Post-operation top view SEM images of Ni-SDC anode. (e) Peak power density comparison of the Ni-SDC anodes with time at 800°C.

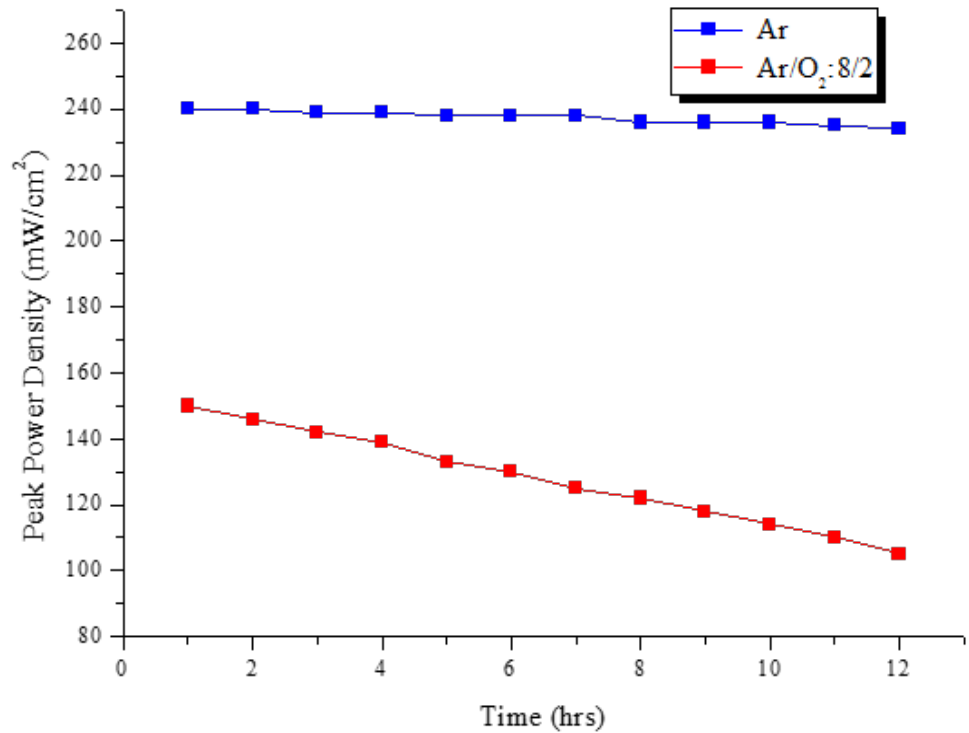


Fig 25 Peak power density comparison of the Ni-SDC anodes with time at 800°C.

images of the Ni-SDC top surface.

It can be seen that there is a very high agglomeration set-in within the reactively sputtered anode as compared to the non-reactive one. The results are similar to the EPMA images (see Fig.23).

Fig. 25 shows the comparison of the peak power densities for both anodes with time at 800°C. It can be seen that Ar only sputtered anodes continued to show nearly the same peak power density with time. Meanwhile, the peak power density of the reactively sputtered anode decreased from 150mW/cm² to 105mW/cm² after 12hrs of operation. The

high agglomeration with time (Fig.24) combined with the post-operation decreased Ni content (Fig.23), could be the cause of the deterioration in peak power density with time, for the reactively sputtered anode. Thus contrary to the common notion shown by previous researchers, about introduction of O₂ to achieve porosity and other required attributes of a successful electrode on a dense substrate, in case of Ni cermet anodes the 20% O₂

1. Retards growth rate
2. Produces lesser catalytic Ni
3. Which leads to decreased performance
4. Also sets in higher agglomeration with time

3.2.7. Logging the optimal sputtering conditions for thin film Ni-SDC anodes

So once we had established it is best not to use O₂ is not the right background gas to use when depositing electrode structures of cermet, we started logging the optimal power and pressure conditions for the Ni-SDC thin film anodes.

Table 6 is a description of the various conditions used to deposit and analyze a suitable Ni-SDC anode for our application. All the anodes were deposited on room temperature. Three main categories of background Ar gas pressures were used to maintain the vacuum pressure, they were 90mTorr, 50mTorr, and 30mTorr. All pressures were tested at a RF power source range of 50W,100W,150W, and 200W.

All samples were deposited on a bare Si wafer and sent for subsequent thickness measurement by FE-SEM. Generally, the deposition rate increased with increasing power at all pressures. It can be speculated that higher sputtering power owes to more

Table 6. Deposition rates of Ni-SDC anodes deposited at various pressures and sputtering powers

Temperature	Chamber Pressure	RF Power	Deposition Rate (nm/hr)
25°C	90mTorr	50W	13.5
		100W	53
		150W	120
		200W	200
25°C	50mTorr	50W	35
		100W	80.5
		150W	101
		200W	110
25°C	30mTorr	50W	25
		100W	60.5
		150W	95.5
		200W	130

Ar ions in the plasma, consequently the number of collisions with the target is increased with increasing power [65-67].

A graph of the growth rate was depicted in Fig. 26 to analyze the trend of the growth rate increase with time. Different trends of growth rate were seen for various deposition pressures at various sputtering powers. For 30mTorr the growth rate increased linearly with increasing power. While for 90mTorr, the growth rate increased exponentially. The most interesting case of growth rate increase was for the 50mTorr chamber pressure. For this pressure the growth rate increase was not as significant as compared to other sputtering pressures. It increases almost sinusoidal until 150W and then there was little or no increase

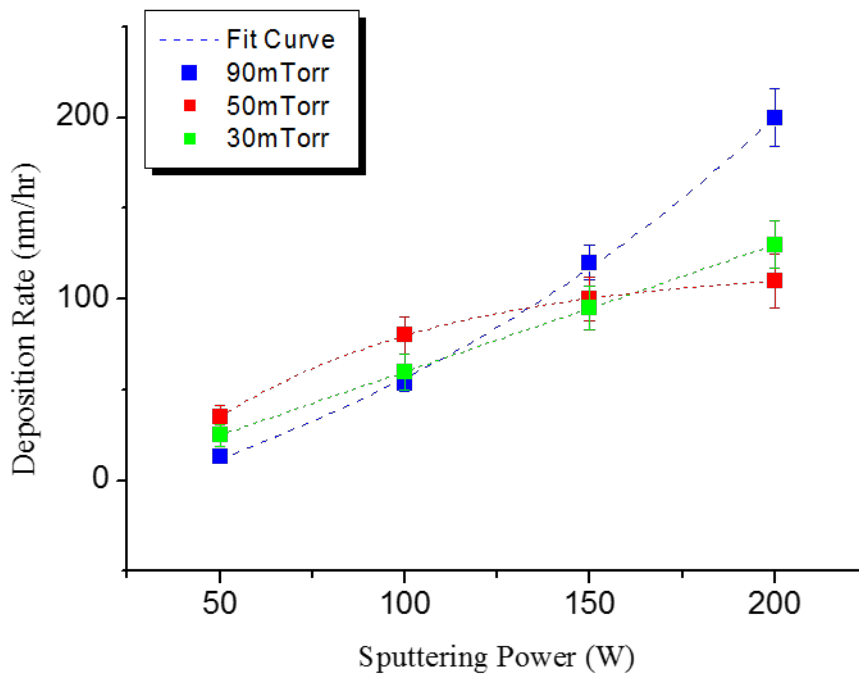


Fig 26. Deposition rate for Ni-SDC at various pressures and sputtering powers

in growth rate found when the sputtering power was increased from 150W to 200W.

3.2.7. 1 Microstructure at different sputtering powers

The top surfaces of the Ni-SDC anodes were then analyzed under high resolution SEM and are shown in Fig. 27. Regardless of the pressure of the sputtering chamber, different sputtering powers showed different thin film micro-structures. The micro-structure for 50W Ni-cermet is rice like, for 100W it changes to granular, for 150 one can see a mix of granular and circular while for 200W the structure of the Ni-cermet is completely circular.

It is common knowledge that circular shape is the easiest to produce porous microstructure, and hence more passage for the fuel to reach the TPBs. Also circular

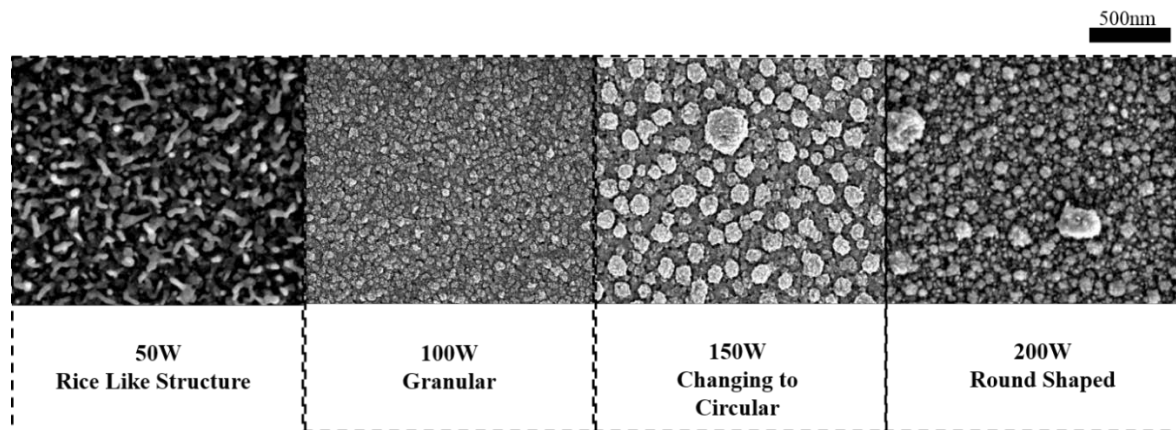


Fig 27 Post operation analysis of Ni-SDC anodes after 12hrs of electrochemical tests

structures are the most favorable for thin film fabrication as they have the smallest perimeter for a given area [68], hence maintaining the low thickness with maximum efficiency.

3.2.7.2 XPS analysis at various powers

The subsequent films deposited at various powers and pressures were now sent for XPS analysis. Table 7 shows an XPS analysis detail of the various anodes deposited at the sputtering power ranges of 50W ~ 200W. It was found out that the RF sputtering showed stoichiometric thin films, and sputtering power had little to no effect upon the percentages on the atomic percentages of Ni or Ce. However, there was a difference in the atomic percentages between the two.

Even though both Ni and Ce have almost similar atomic percentages, (calculated by converting the weight% mentioned in section 3.2.1) Ni 30 at.% ,Ce 29 at.% , Sm 2%, and the rest is oxygen, yet Ni percentage is always higher than the Ce percentage in RF sputtering. This phenomenon can be best described by Winters and Sigmund preferential

Table 7. XPS analysis of various constituent of the cermet Ni-SDC anode at various powers

Sputtering Power (W)	Cerium (at.%)	Samaria (at.%)	Nickel (at.%)
50	16	2	25
100	16	2	26
150	17	2.5	25
200	16	1.9	25

sputtering for [69]. Winters and Sigmund defined an existence of the energy transfer coefficient during sputtering of chemisorbed nitrogen on tungsten by low energy ions. This coefficient can be best described from Eq. (3)

$$\gamma = \frac{4M1.M2}{(M1 + M2)^2} \dots (3)$$

Here,

γ = the energy transfer coefficient of a certain species,

$M1$ = the incident ion mass

$M2$ = the target atom mass

So, in our case the incident atom is always Ar and the target atom constituents are Ni, Sm, and Ce, their respective transfer coefficients can be obtained from Eq. (3) as follows,

$$\gamma_{Ni} = 0.96$$

$$\gamma_{Sm} = 0.65$$

$$\gamma_{Ce} = 0.68$$

Transfer coefficient of Ni is larger than Ce in a Ni-SDC cermet target. So, regardless of the nearly equal atomic percentage of Ni & Ce in a Ni-SDC cermet, the Ni deposition will always be higher than Ce. This fact works in our favor since Ni provides the catalytic activity in a Ni cermet anode, the more catalytic the anode, the better its performance.

3.2.7.3 Performance Comparison

Since 90mTorr sputtering vacuum chamber pressure is the most comparable to the PLD vacuum pressure (100mTorr) used in this paper, in order to make apple-to-apple comparison, this pressure was taken as a representative pressure for comparison of performances. Fig. 28 shows the peak power densities of the Ni-SDC anodes sputtered at 90mTorr at various powers ranging from 50W ~ 200W at 700°C.

OCV for 50W ~ 150W range was almost similar and was nearly 1.0V, OCV for 200W was near 1.15. Peak power density increases linearly with the increase of anode sputtering power. For a 50W sputtered Ni-SDC the peak power density was 12mW/cm², for 100W it increased to 40mW/cm². Peak power density was about 70mW/cm² and finally 130mW/cm² for the Ni-SDC anode cells sputtered at 200W.

A similar increase in performance of indium tin oxide (ITO) films by RF magnetron sputtering by Wu et al. [70]. The authors in the afore-mentioned paper found strong connection of sputtering power and structural orientation of the ITO films. In our deposition process the structure of the films is also constantly changing from rice like shape at 50W, to circular shaped at increased sputtering powers of 150W and 200W. Hence a case can be made that due to the preferred change in film structure at higher sputtering powers, the cells

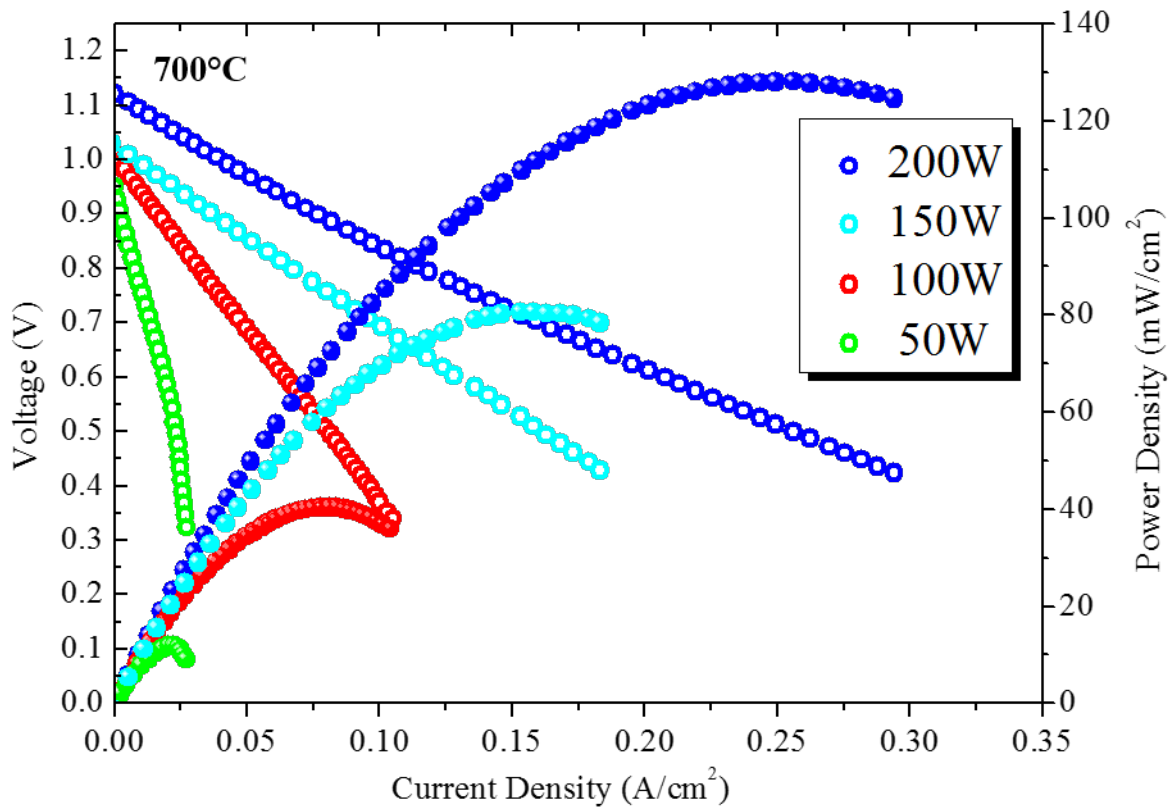


Fig. 28 Performance Analysis of cells with Ni-SDC anodes sputtered at various powers at 90mTorr

containing thin film anodes deposited at higher power at a given background gas pressure, are performing better than those sputtered at lower powers.

3.2.7.4 EIS Characterization

In order to confirm that the shift in performance was due to the change in anode sputtering power, we shifting to the EIS analysis on the cells. Fig. 29 shows the impedance curves of the various cell components taken at OCV for the cells performance measured in Fig. 28.

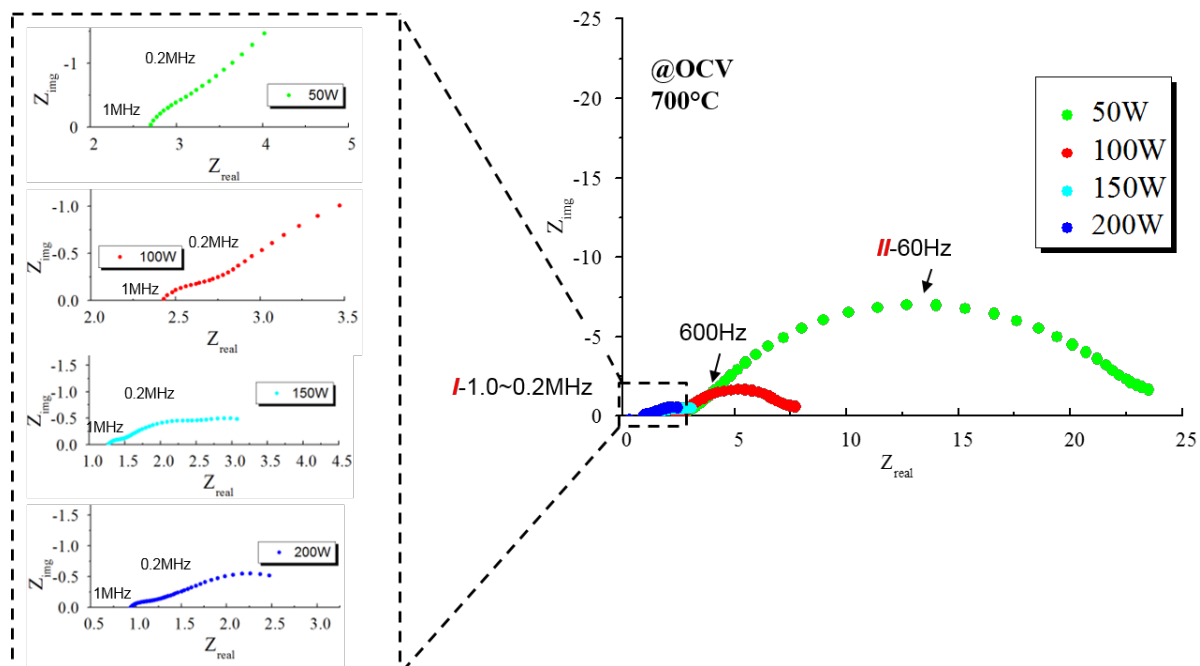
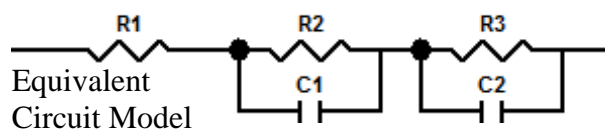


Fig. 29 EIS of the cells from Fig. 28

Table 8. Resistance values at the anode and cathode of the cell obtained via curve fitting of EIS plots from Fig.29



Sputtering Power (W)	$R\Omega$ (ohm-cm ²)	RJ (ohm-cm ²)	$R//$ (ohm-cm ²)
50	2.9	0.7	20
100	2.7	0.4	6
150	1.25	0.3	3.1
200	0.8	0.3	1.8

For all the cells, two distinct peaks were visible, and impedance curve diameter increased with decreasing Ni-SDC sputtering power. One peak appeared at high frequency range of 1.0MHz ~ 0.2MHz, and the other at a low frequency range of 600Hz ~ 60Hz. Since the curve difference is large, most of the high frequency curves could not be shown in a single picture, so they have been described in detail in the in-set magnified view in Fig. 29.

For a clearer perspective we calculated the exact values of the anode and cathode resistances by drawing an equivalent circuit model of the cells. These values were obtained by the curve fitting of the EIS plots from Fig.29 and are shown in Table 8. The circuit model consists of the resistance R , attached in series to the two resistances of R_I & R_{II} . The impedance behavior of the electrochemical reaction at the anode and cathode is represented by the double-layer capacitance constant-phase element (CPE), parallel to the respective electrodes.

Table 8 shows almost all the resistance values were different from each other for cells deposited with different anode sputtering powers. Since the electrolyte and cathode are same for all the cells, at a given temperature range at least the electrolyte and cathode resistances should be comparatively same.

Apart from the ideal system conditions where the electrolyte, anode and cathode resistances are clearly visible in the EIS plot [51]. However, another explanation given by Tuller et al. [71] and then endorsed by Shim et al. [72], was that there might be two different distributions within a high frequency EIS curve, and both can be related to the electrolyte. One could be due to the bulk electrolyte and other due to its grain boundary. Also Meyer et al. reported that the grain boundary arc can be perturbed by application of a small bias of

200mV [73]. So we applied various voltage biases of 0.2V ~ 0.8V to our EIS measurements. The results are shown in Fig. 30. However, we could not see any existence of a second semicircle within the high frequency range. Since we can only see one semicircle in our case, even at magnified views, we can safely say that both the resistances are encapsulated in one semicircle.

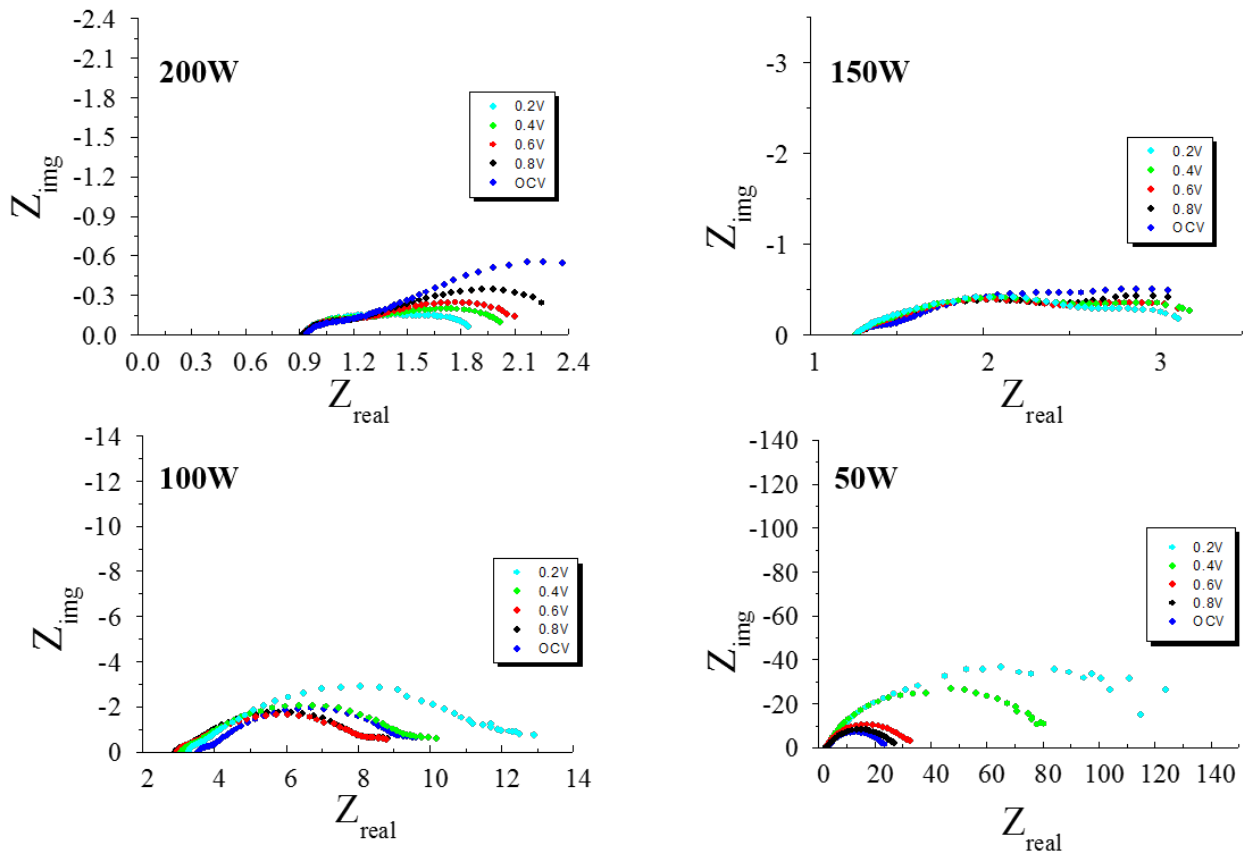


Fig. 30 EIS plots of cells deposited with Ni-SDC anodes at sputtering powers (50-200W) at various applied biases.

Also for a symmetric Pt/YSZ/Pt cell the low frequency arcs were related to the electrode (both anode and cathode) process in literature [74, 75]. For 200W to 150W, high sputtering power Ni-SDC anodes, the low frequency anodes increased with the increasing applied bias from 0.2V~ 0.8V which is normal. However, for 100W and especially for 50W the over potential of the electrodes increased at lower applied biases. The reason could be that the thickness of these films was low. For a 100W Ni-SDC film it was 50nm, while it was about 12nm for a 50W Ni-SDC. And at low applied biases the only contribution to the impedance semicircle is coming from the cathode which is thicker and has much more resistance.

So from Table 8 and Fig. 29 we can see that except for the 50W-Ni-SDC cells, all cells showed the same ohmic resistance RI of about 0.3ohm-cm^2 , and the capacitance values for $C1$ were found to be around 10^{-8}F/cm^2 , typically related to the electrolyte process [72]. There was a marked difference seen in RII of Table 8. RII was high for low power sputtered Ni-SDC anode cells while it was low for high power sputtered Ni-SDC anode cells. This trend was analogous to the peak power shift trend in Fig. 28. Since cathode is the same for all cells, the main electrode creating this difference in impedances is anode, and is the reason for shifts in performances.

3.2.7.5 AFM of the anode surface

The surface roughness is one of the key parameters in determining the structure of deposited materials. Especially for our thin film deposition, it is necessary to see the trend of the surface, since it translates almost similar properties at the top surface as the TPB junction between the anode and electrolyte where all the action takes place.

Atomic Force Microscopic (AFM) results of the anode samples on top of ScSZ pellets

is shown in Fig. 31. Films deposited at 50W were almost flat with no visible grains even at such high resolution. The root mean square (RMS) roughness was about 2.58nm. For 100W we can actually start detecting some grains and the RMS roughness increased to 4.41nm. 150W Ni-SDC anodes started to show some clarity in grain structure until at 200W Ni-SDC we can see clearly visible grains. This grain structure variation is again verifying the trend in grain structure seen in Fig. 27. This phenomenon can be explained in this way, that at high powers, the sputtered particles can get more energized before colliding with the substrate [76].

However, the RMS roughness actually starts to decrease with increased sputtering power after 100W. For 150W the RMS roughness decreased to 3.13nm and for 200W it

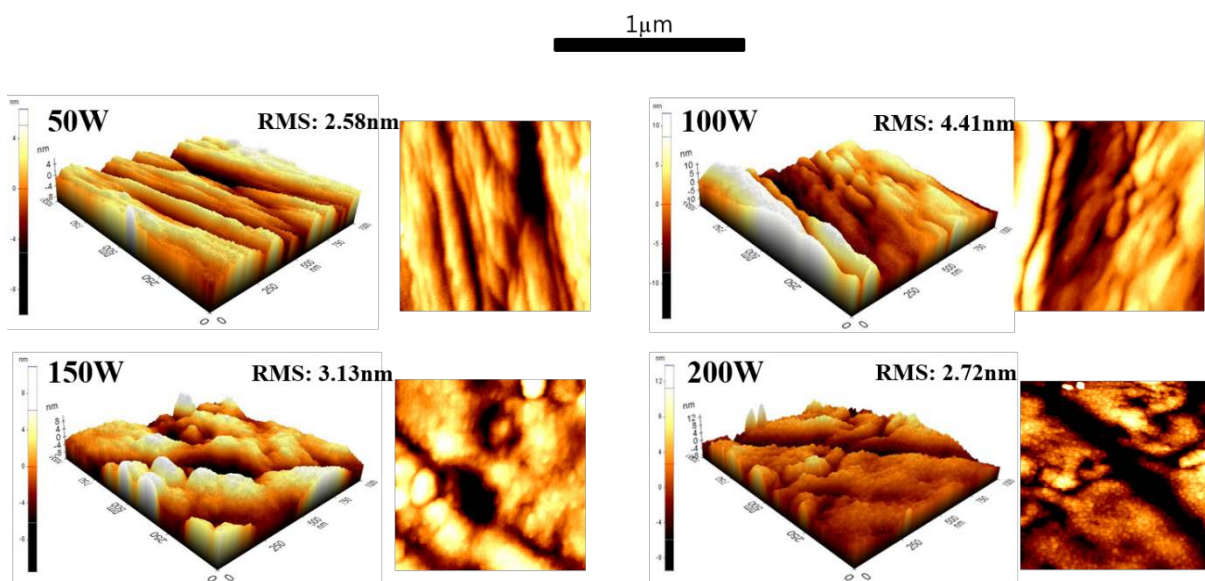


Fig. 31 Atomic Force Microscopy (AFM) of the Ni-SDC anode samples deposited at different sputtering powers, on top of ScSZ electrolytes

decreased to 2.72nm. A similar increase in RMS roughness for RF sputtered In_2S_3 thin films by Hwang et al. [77]. They showed that the RMS increased consistently from 60 – 120W, however the scope of that research was limited to medium powered thin films with a difference in powers of only 20W, which might not be so significant. In our research, the power range is larger, and the difference between two samples is 50W, so it encompasses a wider scope of study. And by increasing this scope we have found that the best roughness is found at 100W, and then it decreases. Previous researchers have showed that the RMS roughness increases with increased thickness due to increase in the grain size [78, 79], however in our case the grain size actually starts to decrease after 100W, and is the lowest for the 200W deposited films and hence shows the minimum surface RMS roughness

3.2.7.6 Optimal Pressure and Power for Thin Film Sputtered Anode

After testing the various thin film properties of the most relatable sputtered anode conditions to PLD anode of 90mTorr, we then went on and checked the performance of 50mTorr and 30mTorr background Ar sputtering gas pressure with a range of sputtering powers of 50W ~ 200W at 700°C. The results have been shown in Fig. 32

Logic would say, that the anode deposited at the largest sputtering power and highest pressure must be the best performing anode. Interestingly, it was not the case. The peak power density was achieved for the anode deposited at an Ar pressure of 50mTorr and RF sputtering power of 100W. This high performance was directly related to the low frequency arc of the nyquist plots, as can be seen from the Fig 32, that the anodes deposited at 50mTorr-100W had the lowest anode over-potential. Thus the optimal deposition condition was logged.

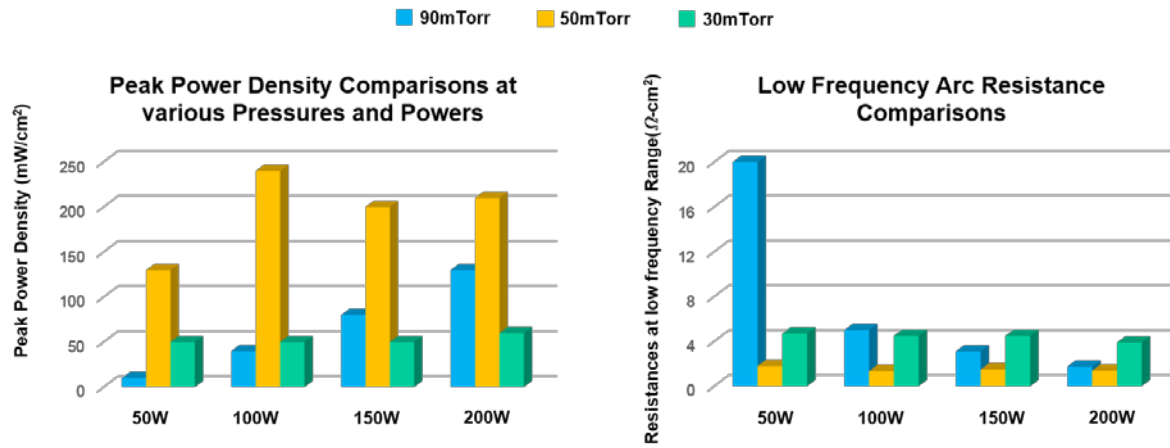
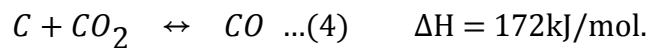


Fig. 32 Peak power density and low frequency arc of the nyquist plot comparison at 700°C, for thin film Ni-SDC anode fabrication via RF sputtering at various sputtering pressures and powers

4. Utilization of Carbon as an indirect source of fuel for the optimized cell

The use of carbon as a direct source of fuel was first introduced about a century ago. The reaction was named as Boudouard reaction named after Octave Leopold Boudouard who discovered this reaction in 1905 [80, 81] . The reaction is highly endothermic and is mostly used in the gasification of carbon (carbonaceous products) [82], and is represented in Eq. (4)



This is the initial concept, that we will place carbon on top of the thin film anode, carbon will react with oxygen ions from the cathode, conducted through the electrolyte, and produces CO₂ in a 4 electrons process.

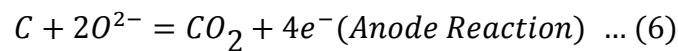


Fig. 33 shows the concept of carbon fuel in direct contact with the cermet anode. Two different carbon types were used 1) Super P-Li carbon 2) Industrial waste Carbon. Super P-Li carbon is a conductive black carbon used as conductive additive in Li-ion batteries [83]. It is of high purity, which means it has a low ash and sulphur content, and its highly structured with a moderate surface area [84]. Industrial waste carbon is amorphous and has a high ash and sulphur content, with low conductivity and moderate surface area [85, 86].

Both carbons were ball milled in order to make them in powdered form and allow easy access to the carrier gas, and placed as a fuel on the anode. The rest of the configuration was exactly the same as used in the cell tested with H₂. Fig. 34 shows the actual picture of the test station.

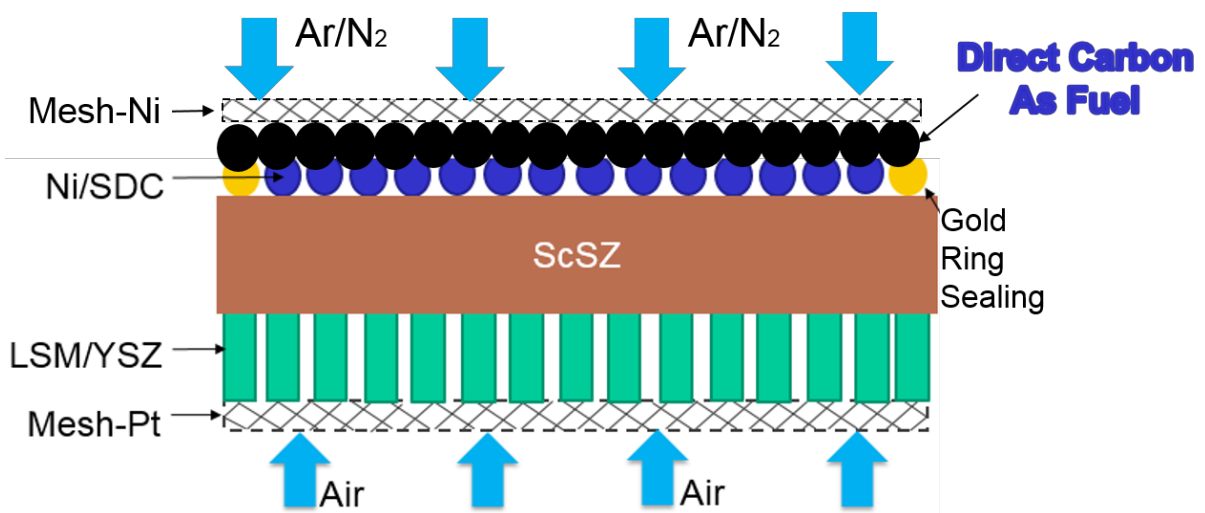


Fig. 33 Usage of Carbon as direct source of fuel to the optimized cell concept

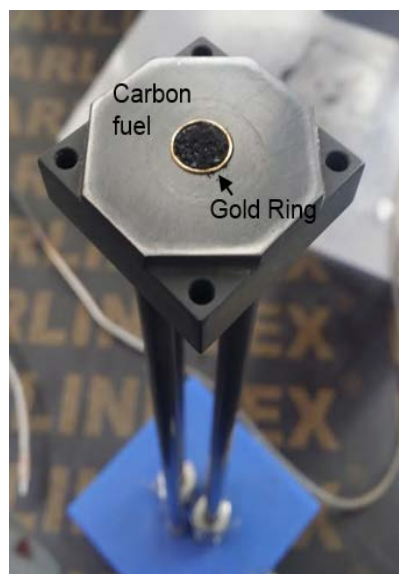


Fig. 34 Ball milled carbon placed on the anode compartment sealed by a gold ring.

Unfortunately, we could not find any OCV and consequently no power output, with the inert carrier gases for both carbons. It might be the carbon is not making any electrochemical connection with the electrolyte at the TPB. It was only when we introduced

hydrogen into the system, that the fuel cell started to show a power output.

Fig. 35 shows the peak power density comparison for the optimized cell under various fuels and carrier gases at 700°C. We found out that with H₂ the impure carbon performed better than the pure one. This is an interesting result, since pure carbon goes through a lot of processing to reach the pureness and has increased costs, so it should be working better than the impure one.

Naqvi et al. [87] showed that in the presence a catalyst of with K₂CO₃ with ash, whose main constituent are sulphur and carbonates of metals, there are extra reactions taking place at

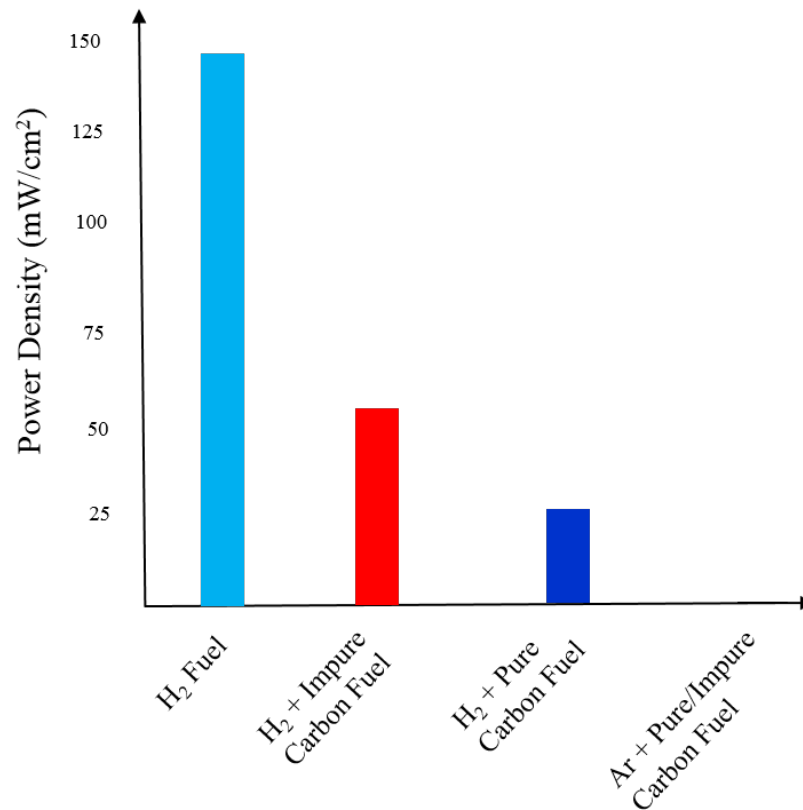


Fig. 35 Peak power density comparison for the two carbons with and without H₂ fuel.

the anode, that produce more CO, and in turn the potassium reacts with steam to give more H₂ fuel. Upon XPS analysis of the Ni-SDC anodes after testing with carbon fuel, we found traces of aluminum and silicon together with some sulphur in the industrial waste carbon. It is possible that these elements are producing some carbon monoxide, under equations below and this CO can react with the oxygen ions conducted through the electrolyte.

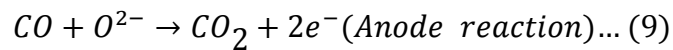
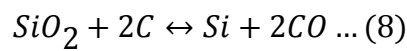
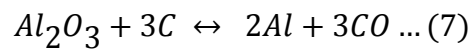


Fig. 35 also shows that with H₂ there was an OCV and power Output, however it was considerably lower than the performance of the cell without carbon. This means that carbon is actually blocking the gas supply until the TPB. Li et al [88] showed that the solid carbon

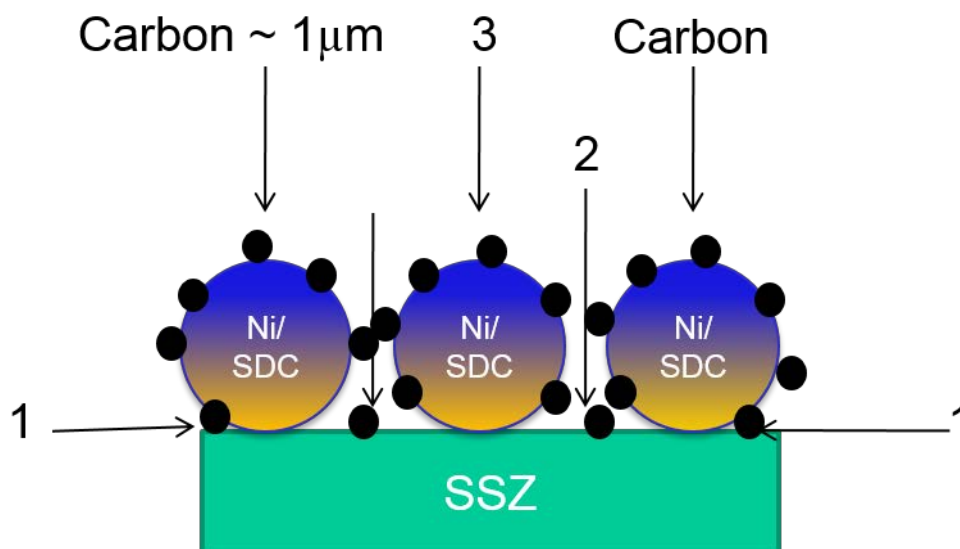


Fig 36. Schematic representation of the carbon reaction sites in a cermet anode on a ScSZ electrolyte base

has three distinct reaction sites on a cell, 1) the intersection of anode and the electrolyte 2) on the surface of the electrolyte 3) on the surface of the anode. Regardless of the type of carbon used, the processes that make up the carbon particles, like ball-milling, cannot produce less than $1\mu\text{m}$ carbon. Our thin film anode however has porosity is in nanometers.

In order to confirm that in case the carbon reached the anode and electrolyte interface, there would be some Boudouard reaction, we removed the anode of the cell and deposited carbon on top of an anode-less cell. Fig. 37 shows the performance of the anode-less cells with pure and impure carbon fuels. Similar to the results seen in Fig. 35, the impure carbon performed better than the pure one. The OCV for pure carbon anode-less cell was nearly 0.5 while the OCV for impure carbon anode-less cell was 0.9V. The peak power density for impure and pure anode-less cells was $0.27\text{mW}/\text{cm}^2$ and $0.1412\text{mW}/\text{cm}^2$. Xu et al. [89] was also able to achieve high power densities without any anode using a carbon and carbonate mixture suspended in form of a slurry on top of a cathode support. Our cell didn't show such high performances, because the carbon was in solid form, but an electrochemical interface was certainly proved.

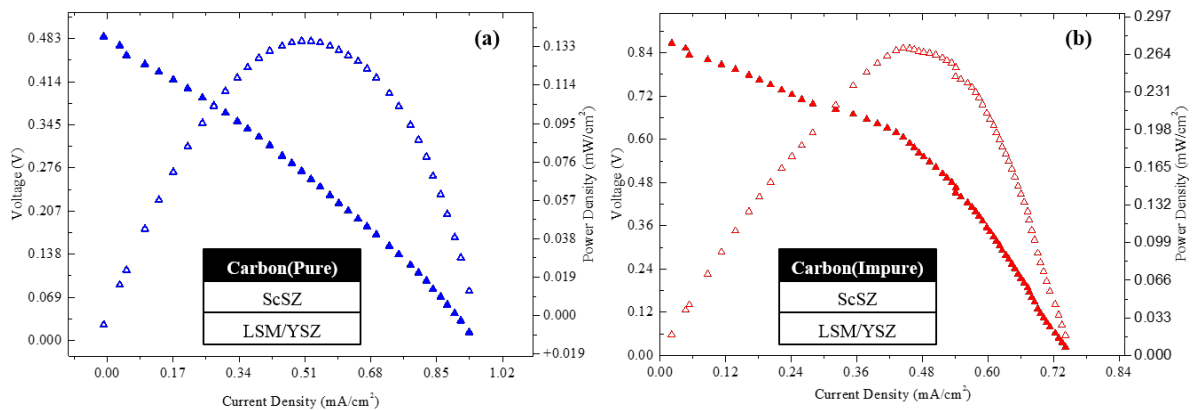


Fig. 37 Anode less cell test for (a) Pure (b) Impure carbon at 700°C.

Hence it can be concluded that carbon in its solid form is failing to reach these reaction sites and hence not showing any electrochemical reaction. Another option is to use carbon in some form of liquid phase, since liquid phase has a better chance to find its ways to the TPBs, however the test station setup does not allow the usage of carbon in this form. We had to take other steps

4.1 The Reverse Boudouard Reaction (RBR)

In order to deliver carbon to the nano-pores of the thin film cermet anode and ultimately to the TPBs, we needed to devise a method that can utilize carbon or its by-products in other forms. The reverse boudouard reaction is a non –electrochemical reaction where CO₂ reacts with coke or carbon at a high temperature (>700°C) and produces CO. This CO gas in turn can be used as a source of fuel. The detailed reactions are shown in Table 9.

Table 9. The equations involved in the indirect utilization of carbon fuel.

#	Reactions	Details
(a)	$\text{C} + \text{CO}_2 \rightarrow 2\text{CO} \dots (10)$ <p style="text-align: center;">(> 700°C)</p>	Reverse Boudouard Reaction (NonElectrochemical Reaction)
(b)	$\text{CO} + \text{O}^{2-} \rightarrow \text{CO}_2 + 2\text{e}^- \dots (11)$	Anode Reaction OCV~1.1V
(c)	$\text{C} + \text{O}^{2-} \rightarrow \text{CO}_2 + 2\text{e}^- \dots (12)$	Anode Reaction OCV~1.2V

We have already seen that Eq. (12) from Table 9 is not viable for our setup so we need to filter out any unreacted carbon from our system. However, the CO gas produced from the carbon in Eq. (10), which is essentially called the reverse boudouard reaction, can be used as a fuel. Reverse Boudouard reaction takes place at high temperatures of $> 700\text{C}$, because at higher temperature the standard enthalpy of the endothermic reaction in Eq. (4) becomes less negative with increase in temperature [90]. Additionally, reaction kinetics and mass transport rates are faster in a gaseous phase than in liquid or solid phase.

4.1.1 The gasification of carbon with Inconel Filter

The process of reacting a material with a gas at a given temperature is termed as gasification. Carbon gasification is achieved at high temperatures of 700°C as mentioned in Table 8, and its byproducts need to be removed. An inconel 600 grade (APEC Industries, South Korea) was used to filter the by-products of the carbon gasification process. It is a 2mm thick inconel plate which has a $20\mu\text{m}$ pore opening. It was tested for good condition and air permeability by the manufacturer. The filter was machined and placed in the outlet of a bubbler. The pictures of this bubbler and attachment of the Inconel filter are shown in Fig. 38.

The inconel filter was machined to sit on a stainless steel ring, which was welded to the outlet of the bubbler. A carbon fuel inlet was designed on top of the bubbler, for readily filling up the depleted carbon fuel. CO_2 enters the bubbler and reacts with the carbon inside the bubbler at a high temperature. The resulting CO produced due to the reverse boudouard reaction will then leave the outlet of this bubbler after being filtered from the filter.

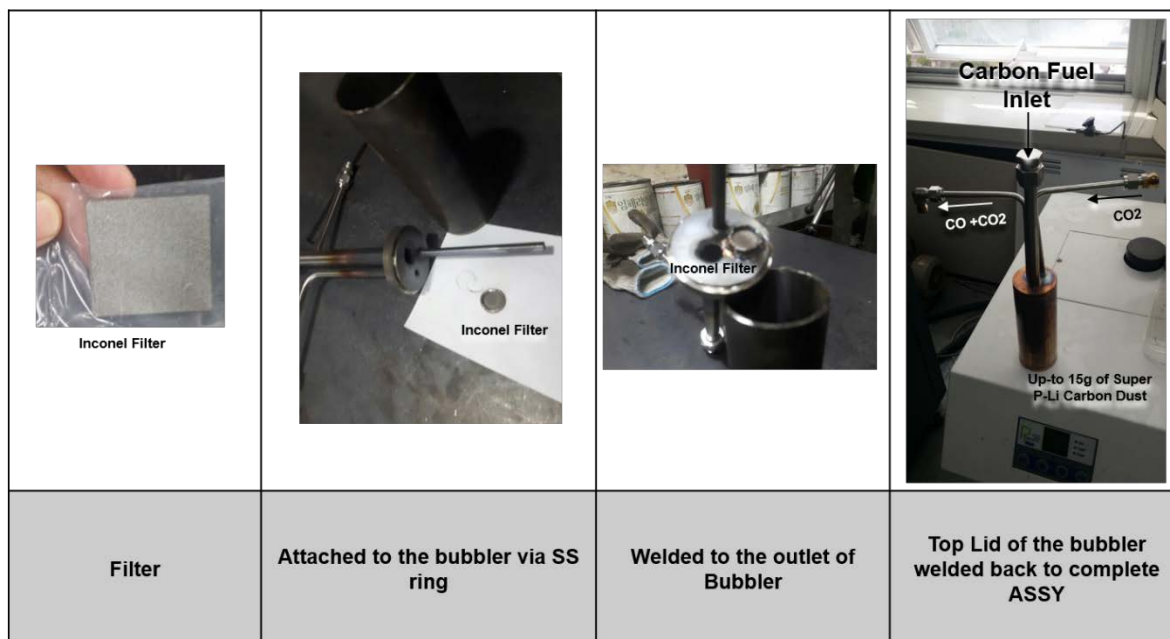


Fig. 38 Inconel Filter and its attachment on the bubbler assembly

4.1.2 The Indirect Carbon Fueled Hybrid Fuel Cell

Fig. 39 shows the system devised to utilize the carbon fuel indirectly in the optimized anode cell. A 100sccm CO₂ gas enters the bubbler via a CO₂ mass flow controller. The bubbler contains 10g of raw impure waste carbon, placed inside a furnace at which the temperature can reach up to 1000°C. The outlet of the bubbler was fitted to the gas chromatograph (GC) to identify the products of the reverse boudouard reaction. The GC was off-station and measured in Chung-Ang University material science lab.

The outlet to GC was attached to a H₂ gas supply line with a switch. The H₂ can also enter the fuel cell system easily by controlling the H₂ MFC. This hybrid fuel system is connected to the test station setup discussed in detail in section 2.4, where the optimized cell is tested for electrochemical measurement via Solatron.

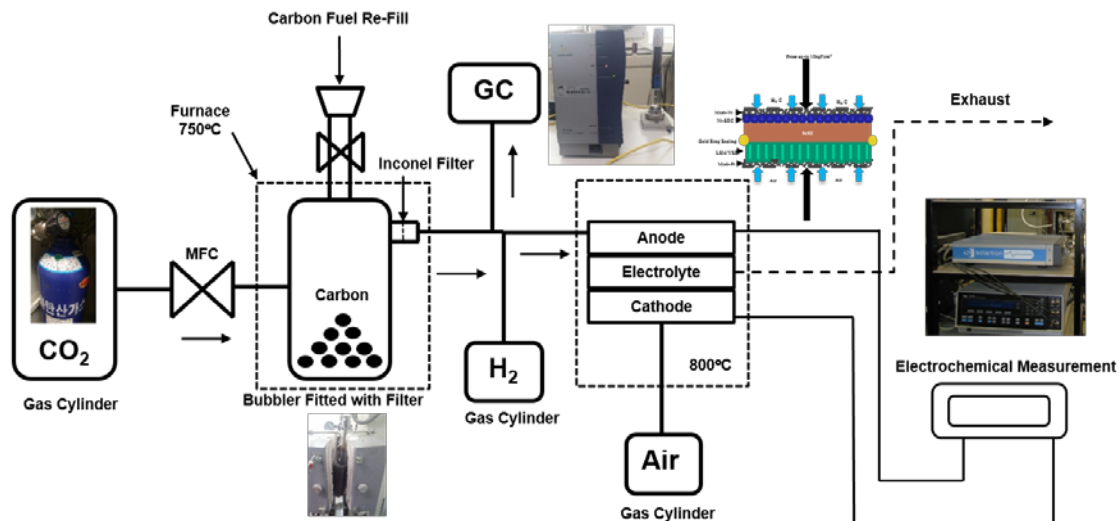


Fig. 39 Schematic Representation of the indirect carbon fueled hybrid fuel cell

4.1.2.1 Performance

Fig. 40 shows the gas chromatography and the OCV of the optimized fuel cell with increasing furnace temperature over a period of 12hrs. It is noted that as the temperature increases there is nothing picked up by the GC other than the unreacted CO₂ for almost 2hrs. After 2hrs, the percentage of CO₂ starts to drop, and even though there is no CO detected, we can detect a slight OCV of 0.2 V.

The drop in the CO₂ keeps happening steadily, and the OCV rises from 0.2V to 0.5V after 7hrs, until the bubbler temperature of 750°C is achieved. After 7hrs the GC starts detecting CO which keeps on increasing steadily as the CO₂ drops further down. The maximum CO level is attained after 11hrs. After 9hrs an OCV of 0.6V is achieved. It is at this point that the peak power density of the cell was tested.

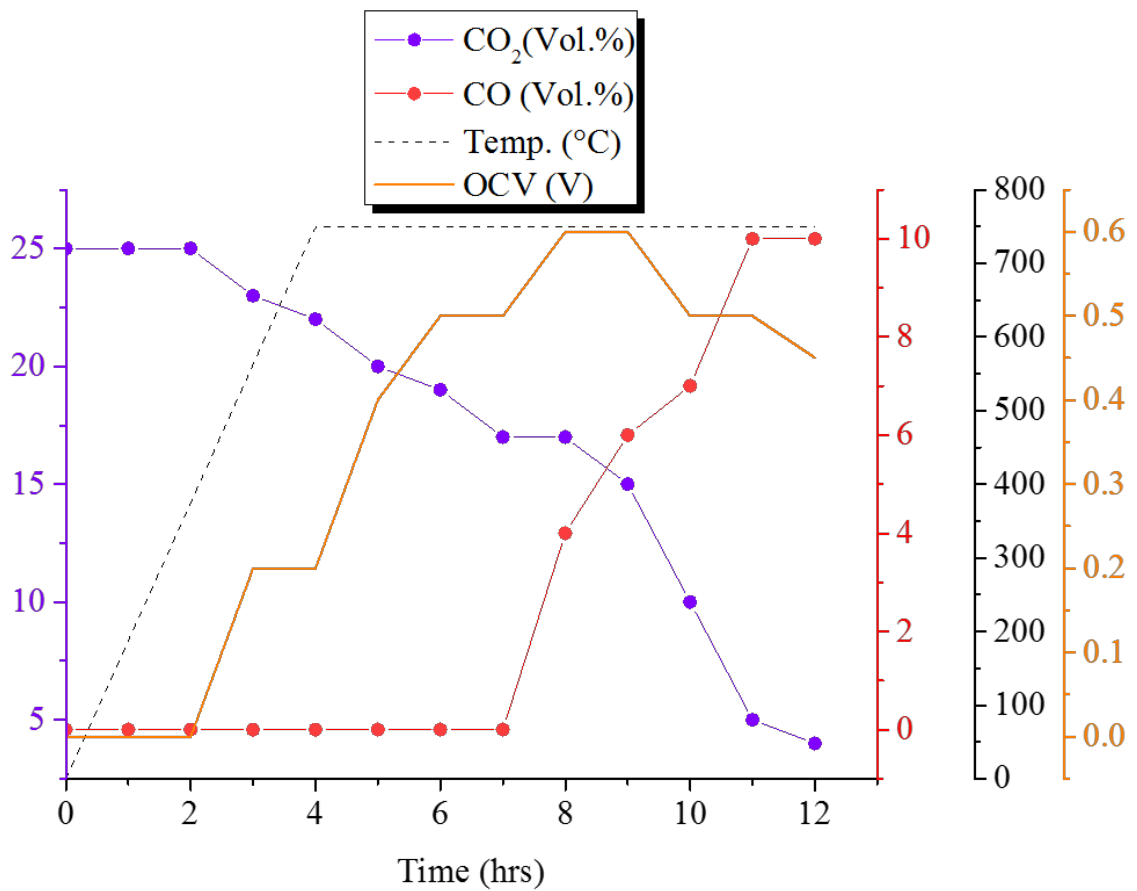


Fig. 40 Off-grid Gas Chromatography results of 5g of carbon. OCV of the cells was taken with time at various temperatures

Fig. 41 shows the peak power density of the indirect carbon fueled hybrid fuel cell at 700°C. It can be seen that the peak power density and the OCV achieved with the carbon are almost half the peak power density achieved with hydrogen fuel for the same hybrid cell. However, this wasn't the biggest concern.

It was seen that after 9hrs of operation, the OCV and the power density continuously kept on decreasing. Fig. 42 shows that after 10hrs of operation, the OCV of the cell starts decreasing and consequently the peak power density also decreases. Both keep on decreasing until there is no more OCV after about 20hrs of operation.

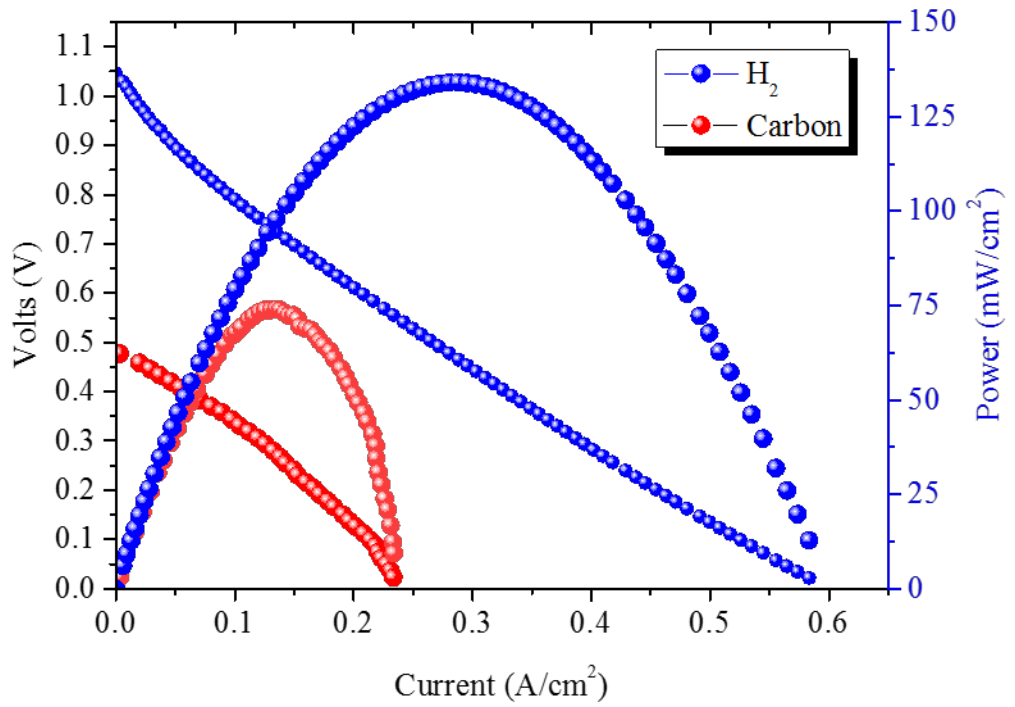


Fig. 41 Peak Power Density comparison for the indirect carbon fueled hybrid fuel cell at 700°C

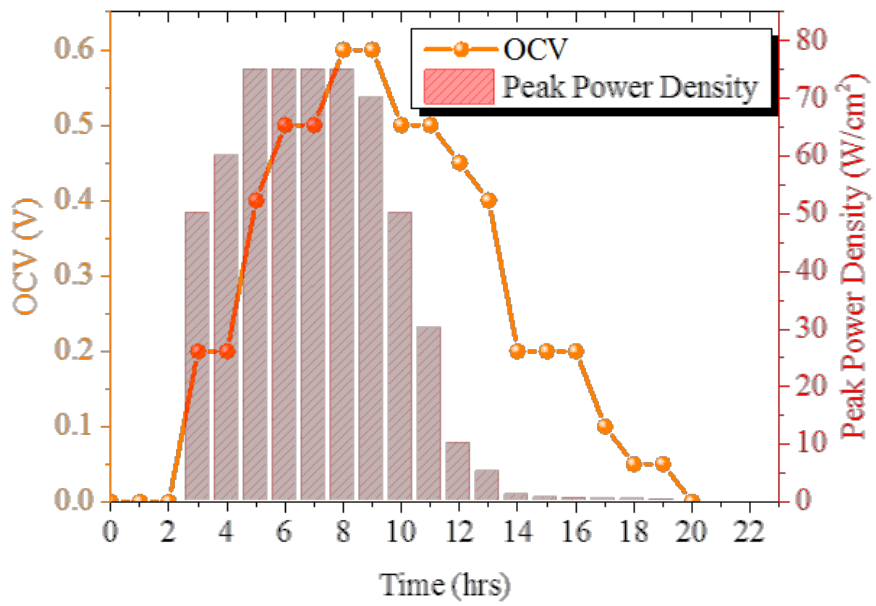


Fig. 42 Peak power density and OCV shift with time

The bubbler was then taken to the off-grid GC setup, and it was found that no CO was being produced by the system. It is possible that after the first few hours of operation, the CO₂ might have stopped reacting with the available carbon in the bubbler. The OCV is produced by the CO produced only in the first 12hrs of operation, and then CO₂ gas makes a consistent shortest possible route outside the bubbler via the filter. Fig 43 (a) shows a schematic representation of this process. Upon opening of the bubbler outlet, some unreacted carbon dust was also seen at the pipe connections. Also the carbon in the bubbler was forced out and weighed, it had only dropped by 0.3g. This means that almost 97% of the carbon remained un-utilized for such a long operation.

In order to maximize the utilization of the carbon fuel, I updated the design of the bubbler. The new design is shown in Fig. 43(b). The inlet to the bubbler was modified, so

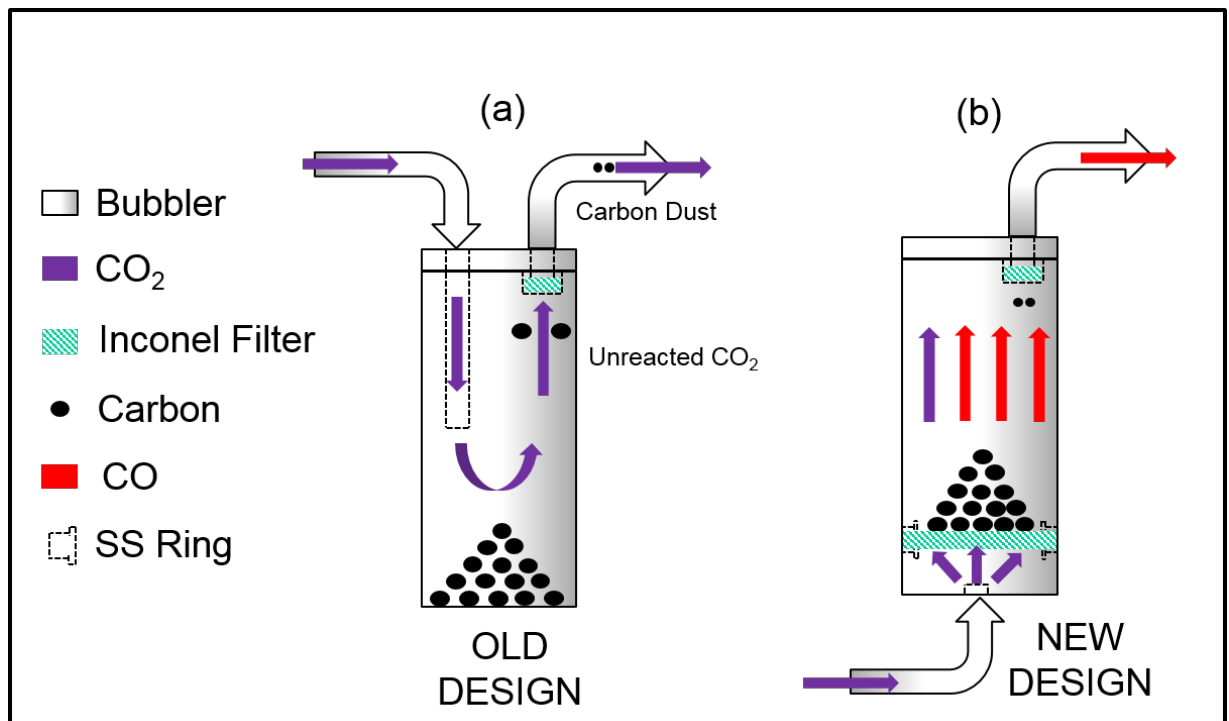


Fig. 43 (a) Schematic of the old design of the bubbler with little or no CO (b) modification in the bubbler design resulting in higher carbon utilization and hence higher CO.

that the CO₂ now enters from the base of the bubbler. A second inconel filter is welded just a few centimeters above the base of the bubbler. With this new design the carbon fuel now sits on top of the filter, and almost all of the CO₂ passes through the filter and bubbler after reacting with the carbon. Also with the two filters, the carbon dust does not build up, and allows free passage of the gases without blocking the lines. Hence even unprocessed carbon in raw form can also be used with this new design.

After updating the bubbler design, the hybrid fueled cell performance was again measured and is shown in Fig. 44. First noticeable thing is that the OCV has increased to 0.86V compared to 0.6V with the old bubbler design. Also the peak power density has increased to 110mW/cm². It is almost 82% of the peak power density achieved by H₂ fuel source. Which is quite reasonable considering the cost effectiveness of the carbon fuel compared to the H₂ fuel.

There is however a certain noise during the electrochemical measurement, especially at the mass transport region of the IV curve in Fig. 44 for carbon fuel. It is possible that in the start of the reaction process, say first few hours, the reverse boudouard reaction is not producing CO at a constant rate, and hence the fuel is not readily available for the electrochemical reaction. Later on the reverse boudouard reaction attains equilibrium, and we did not find any noise in the IV curve measurement.

Fig. 45 shows the peak power densities and OCV with time for the updated bubbler design. It shows that an OCV of 0.86V is achieved after 2hrs, which increases to 0.9V in 6hrs and stays there for the next 8 hrs. These measurements were taken after every hour until 20hrs of operation, the optimal hybrid cell showed a consistent OCV of 0.85 V and the peak power density reduced to 90mW/cm². This means that for nearly 1 day of operation

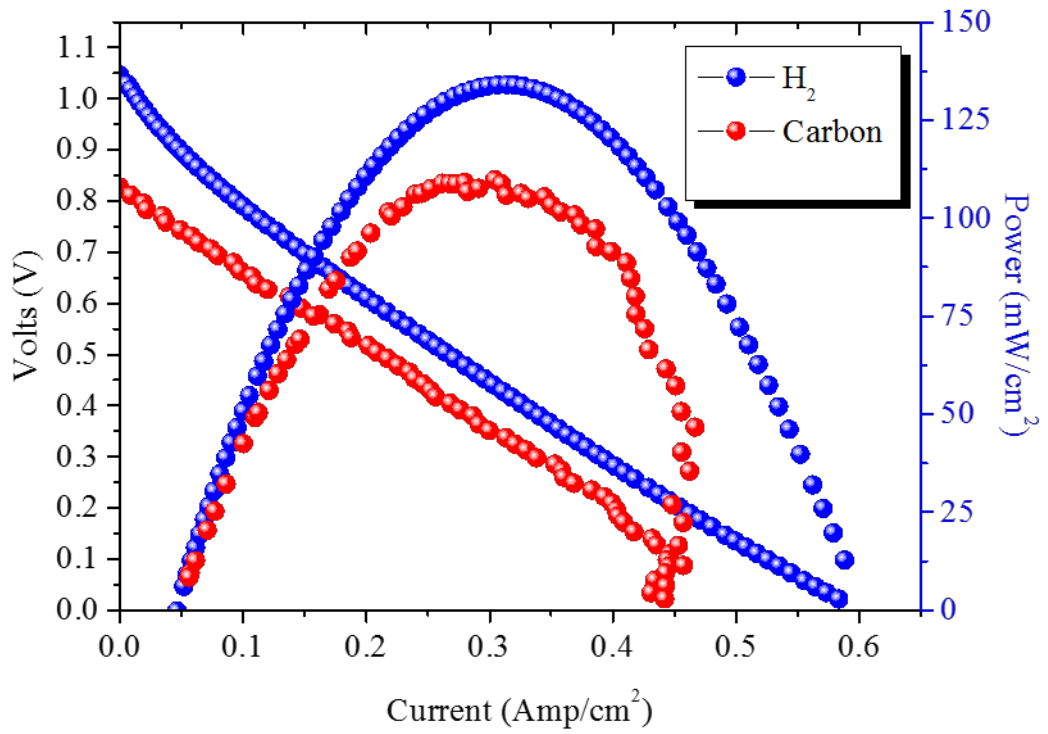


Fig. 44 Peak Power Density comparison for the indirect carbon fueled hybrid fuel cell at 700°C

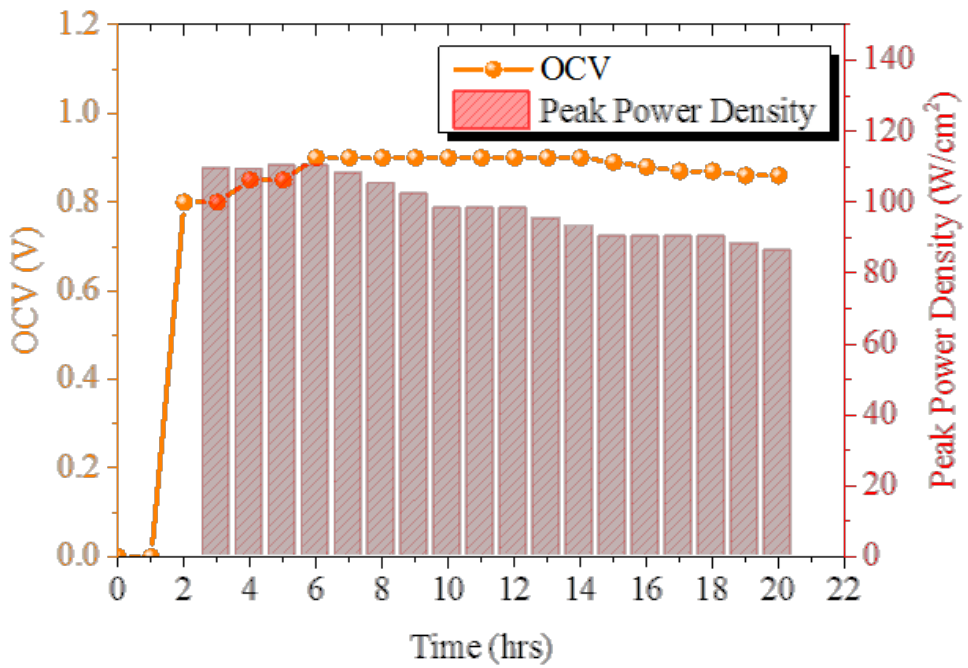


Fig. 45 Peak power density and OCV with time for the updated bubbler

the cell keeps on performing under carbon fuel with a decrease of only 20% of its peak power density compared to the start of the day. The ScSZ electrolyte support is dense and it is believed that this cell can perform as long as there is carbon inside the bubbler. The cell was tested to give a consistent OCV of 0.8V for 50hrs of operation.

Fig. 46 shows the peak power density comparisons OCV comparisons of cells made by other researchers at various carbon fuel mixtures, with this research. Tang et al. [36] utilized Fe-loaded pure carbon fuel on an Ag-GDC anode to achieve a peak power density of 45mW/cm² at 800°C. Even with the use of a noble metal as an electrode with a catalyzed fuel at 100C higher temperature than our paper, the cell by Tang et al. performed remarkably lower than ours. Wu et al. [37] showed a carbon fuel cell (CFC) with a high power output by integrating Fe_mO_n-M_xO (M = Li, K, Ca) catalyst with activated carbon in a Ni-ScSZ anode supported cell on ScSZ electrolyte with LSM cathode. The peak power density for this cell setup was 98mW/cm² at 775°C. So even at a higher temperature than our setup, this cell couldn't match with the performance of this paper.

Naqvi et al. [87] used steam gasified carbon with K₂CO₃ catalyst on a tubular Ni-YSZ anode support with a YSZ electrolyte and LSM cathode, and was able to achieve a peak power density of 53mW/cm² at 700°C, which lacks behind the system proposed in this study by a fair margin. Li et al. [91] showed an improvement in performance of a Ni/YSZ anode supported button cell on a 20µm electrolyte with an LSM/ScSZ cathode, by using a potassium (K) catalyst with carbon black gasified by RBR. It showed a peak power density of 95.6mW/cm² at 700°C. Even with a thinner electrolyte, leading to lower ohmic resistance, the peak power density was lower than the result of this research.

The reason of the performance enhancements achieved in this research, can be related

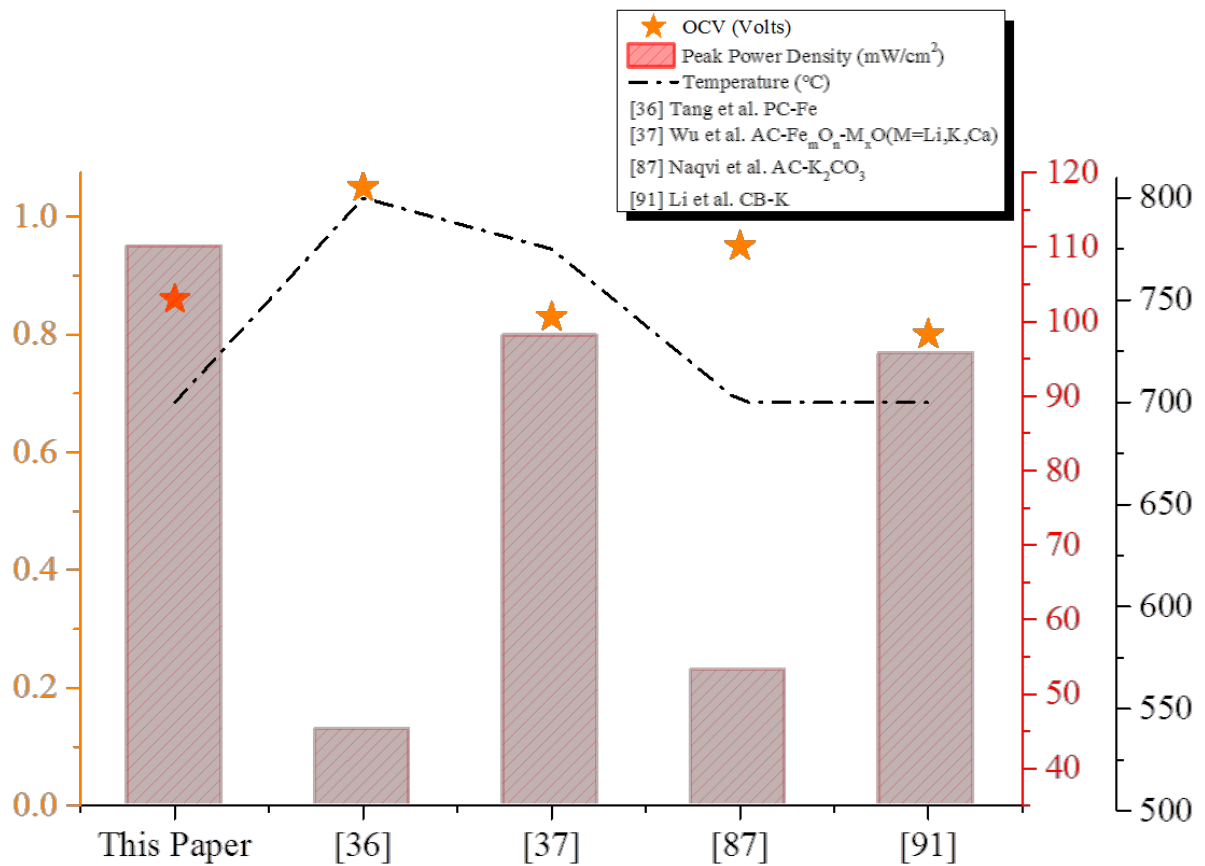


Fig.46 Peak power density and OCV comparison of the optimal carbon fuel cell proposed in this study with previous reported cells.

directly to the use of optimal thin film fabrication methods utilized to fabricate the Ni-SDC anode in this paper, since all the action of the RBR takes place on the anode side of the cell.

Thus this improved, cost effective system, to utilize waste-carbon in its most raw, un-processed form, without any added catalysts, performs better than the reported cells of same category, at an intermediate temperature of 700°C.

5. Simulation of the Optimal Ni-SDC Anode

Nomenclature	
i_{tpb}	TPB density (m/m^3)
i_0	Exchange current density per unit volume (A/m^3)
$i_{0,tpb}$	Exchange current density per unit TPB length (A/m)
η	Overpotential (V)
F	Faraday's Constant (C/mol)
P	Partial Pressure (Pa)
σ	Conductivity (m^2/s)
E	Electric Potential (V)
E^{eq}	E at equilibrium (V)
E_0^{eq}	E^{eq} at standard state
Φ_{el}	Electronic Potential (V)
Φ_{io}	Ionic Potential (V)
V	Volume Fraction
τ	Tortuosity Factor
C_i	Contiguity of species i
N_L^{ii}	Number of intercepts within species i
N_L^{ijk}	Number of intercepts within species ijk
λ_i	Mean free path of species i
\bar{L}_i	Mean intercept length (m)
d_i	Grain diameter of species i (m)

D_{ij}	Binary diffusion coefficient (m^2/s)
X_i	Molar Fraction of Species i
P_i	Partial Pressure of species i (Pa)
N_i	Molar flux of gas species i ($mol/s.m^2$)
μ	Viscosity (Pa.s)
K	Gas Permeability (m^2)
M_i	Molecular weight of species i
$\sum v_i$	Diffusion volume of molecules of species i (m^3/mol)
$\left(\frac{S}{V}\right)$	Surface to volume ratio

In order to simulate a Ni-SDC composite anode, we have to take a representative porous homogeneous anode as shown in Fig. 47. Electrochemical representation of the RBR is given by a Butler-Volmer Type equation. Local charge transfer rate at the Ni-SDC anode is given by following equation,

$$i_{tpb} = i_0 \left[\exp\left(\frac{2F}{R_0T} \eta_{act}\right) - \exp\left(-\frac{F}{R_0T} \eta_{act}\right) \right] \dots (10)$$

$$i_0 = i_{0,tpb} l_{tpb} \dots (11)$$

Exchange current density per unit length of tpb for H₂ oxidation has been given by Suzue et al. [92]

$$i_{0,tpb,H_2} = 31.4 P_{H_2}^{-0.03} P_{H_2O}^{0.4} \exp\left[-\frac{18300}{T}\right] \dots (12)$$

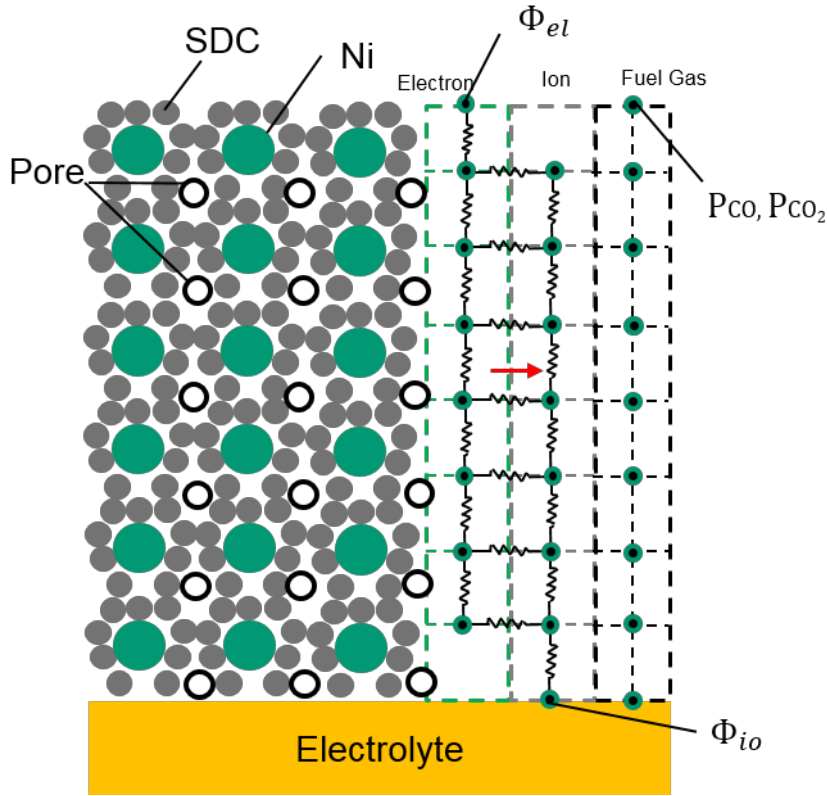


Fig.47 Schematic representation of the nanostructured anode for simulation

However, *Yakabe et al.* [93] reported that there is a higher over-potential for CO oxidation than H₂

$$J_{CO, an} < (2\sim 3) J_{H_2, an} \dots (13)$$

So we can assume that the exchange current density of CO oxidation can be represented as

$$i_{0,tpb,CO} = 0.4 i_{0,tpb,H_2} \dots (14)$$

So Equation 12 can be updated as

$$i_{0,tpb,CO} = 12.5 P_{CO}^{-0.03} P_{CO_2}^{0.4} \exp\left[-\frac{18300}{T}\right] \dots (15)$$

Governing equations for ionic and electronic conduction in a cermet anode are introduced by *Kishimoto et al.* [94]

$$\nabla * (\sigma_{el}^{eff} \cdot \nabla \phi_{el}) = i_{tpb} \dots (16)$$

$$\nabla * (\sigma_{io}^{eff} \cdot \nabla \phi_{io}) = -i_{tpb} \dots (17)$$

Effective electron and ion conductivity for Ni-SDC anode can be defined as

$$\sigma_{el}^{eff} = \sigma_{el} \frac{V_{Ni}}{\tau_{Ni}} \dots (18)$$

$$\sigma_{io}^{eff} = \sigma_{io} \frac{V_{SDC}}{\tau_{SDC}} \dots (19)$$

Bulk electronic and ionic conductivities of Ni and SDC were defined by Nicollet et al. [95]

$$\sigma_{el} = 3.27 \cdot 10^4 \cdot \exp(-10.653/T) \dots (20)$$

$$\sigma_{io} = 3.40 \cdot 10^2 \cdot \exp(-10350/T) \dots (21)$$

Now, we can define the activation over-potential of a cermet anode operating on RBR

$$\eta_{act} = E - E_{eq} \dots (22)$$

Re-writing in form of ionic, electronic and concentration potential

$$\eta_{act} = \phi_{el} - \phi_{io} - \eta_{con} \dots (23)$$

Where

$$\phi_{el} = \Phi_{el} \dots (24)$$

$$\phi_{io} = \Phi_{io} + E_0^{eq} + \frac{RT}{2F} \ln(P_{CO_2,Bulk}/P_{CO,Bulk}) \dots (25)$$

$$\eta_{con} = \frac{RT}{2F} \ln(P_{CO_2,Bulk}/P_{CO_2} * P_{CO}/P_{CO,Bulk}) \dots (26)$$

In order to calculate the volume fractions of the different fractions of the cermet anode, we took the aid of High resolution SEM images. Fig. 48 shows the HRSEM top surface of the Ni-

SDC anode. In order to quantify the volume fraction of the we used the freeware of Image J software. By thresh holding we can separate them and it has an easy function of finding out the total cover area of each threshold. Which can separate the phases in 2D and then integrate them along the 500nm thickness to get the volume fraction.

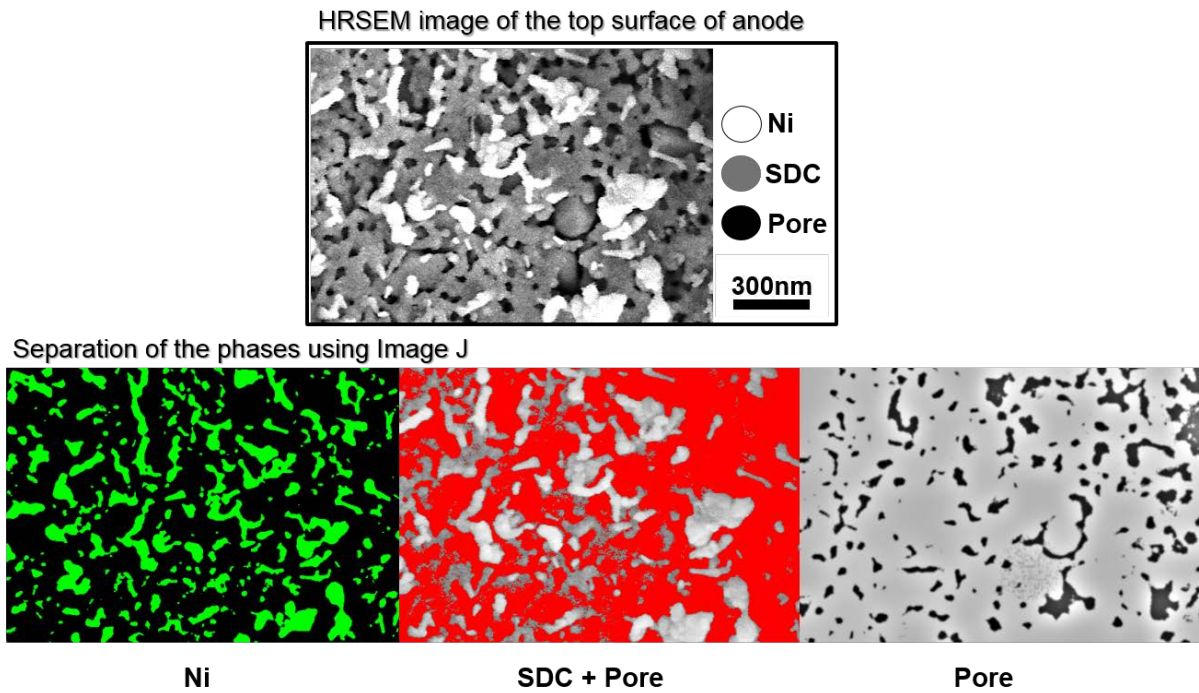


Fig.48 High resolution SEM image of the Ni-SDC anode and phase separation by Image J

Table 10. Volume Fractions V_i of each phase [%]

Sample#	1	2	3
Ni	28.6	25.9	27.2
SDC+ Pore	71.4	74.1	72.8
Pore	13.8	15.9	17.3
SDC	57.6	58.2	55.5

Now Ni and Pore, (black and white phases) were able to be separated easily by using the threshold. However, the thresh holding of grey and black particles was difficult. So we first found out the grey and black covered area in one thresh hold, which would represent both the SDC and pore structure. Then we changed the settings of the thresh hold so that now only the black pores area was seen. Then that pore area was subtracted from the SDC and pore area to give the SDC volume fraction. The volume fractions of each phase were taken across three HRSEM representative samples and have been summarized in Table 10.

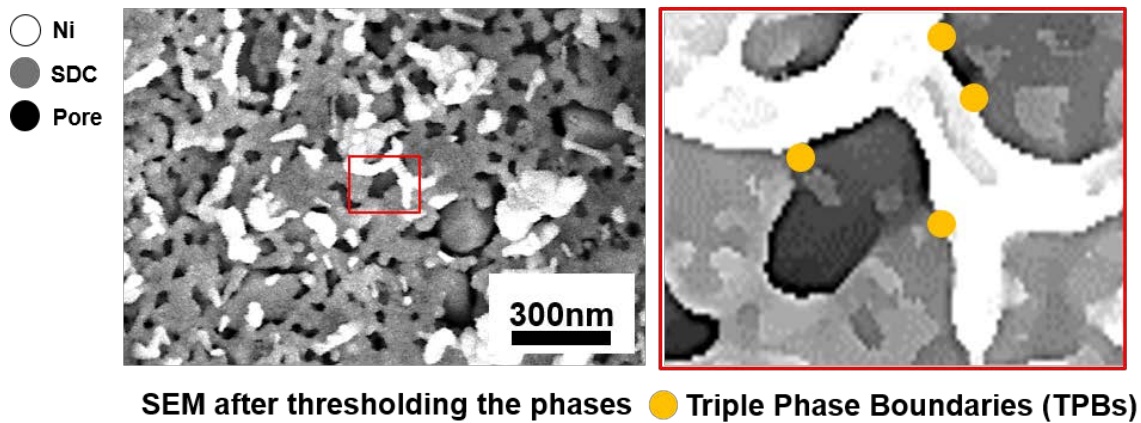
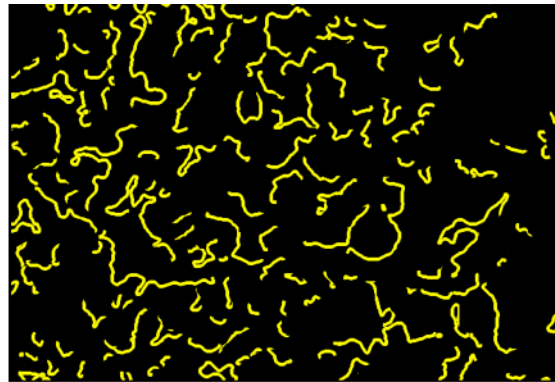


Fig.49 Magnified view of the HRSEM Ni-SDC anode with triple phase boundaries marked

Triple phase boundary (TPB) density was calculated by volume expansion method (VEM). A magnified view of the HRSEM was taken and the junction points between Ni, SDC were expanded to an infinitely small area. This small expansion resulted in overlapping of the Ni-SDC-pore phase, highlighting a TPB point. Fig. 49 shows the magnified view of the HRSEM anode image and the TPB points are marked.

Hiroshi et al. [96] showed that the TPB points can be joined to form a string along the volume of a structure if a) the space resolution is high, b) volume expansion is limited to infinitely small level. Fig. 50 shows such mapping of the TPBs obtained by VEM in image J

software. These TPBs were mapped along 3 different densely populated TPB areas and are represented in Table 11. Average TPB densities were about 3.3 $\mu\text{m}/\mu\text{m}^3$. This value is higher than the value of TPBs found by Hiroshi et al. for Ni-YSZ thick anode. The reason might be that the conventional fabrication methods like the one used by above mentioned authors are not providing the perfect conditions for an optimal cermet anode containing maximum TPBs. Also the thickness of their anode is in micrometer range, so there might be some errors along the large thickness.



Mapping of the TPBs in the Ni-SDC anode by VEM

Fig.50 TPB strings for Ni-SDC anode formed by volume expansion method

Table 11. TPB densities from three different images similar to Fig. 50

Sample#	1	2	3
TPB density [$\mu\text{m}/\mu\text{m}^3$]	3.39	3.22	3.44

Now we aimed to find the tortuosity of each phase in order to see how tortuous the path of the respected transported item is, from a certain phase. Gurland et al. first defined the contiguity of a phase in a i-j mixture as a fraction of the total internal surface area of this phase shared with particles of the same phase and expressed as,

$$C_i = \frac{2N_L^{ii}}{2N_L^{ii} + N_L^{ij}} \dots (27)$$

For Relation of phase contiguity and mean free path, another relation was derived by the same group,

$$\lambda_i = \frac{\bar{L}_i}{1 - C_i} \dots (28)$$

where \bar{L}_i is the mean intercept length, which for our case of 3 phases can be described by the following relation

$$\bar{L}_i = \frac{V_i}{N_L^{ii} + N_L^{ijk}} \dots (29)$$

where N_L^{ijk} is the number of intercepts between the three species and is equivalent to the length of the TPBs found from Table 11.

Underwood [97], related the contiguity of and mean intercept length in a mixture of two phases

$$C_{ij} = \frac{V_i \bar{L}_j}{V_i \bar{L}_j + V_j \bar{L}_i} \dots (30)$$

Fan et al. [98] proved that for equi-axed grains the mean intercept length of the species \bar{L}_i is equal to the mean diameter d_i of that species, So Eq. 30 can be rewritten for each phase interaction as,

$$C_{ij} = \frac{V_i d_j}{V_i d_j + V_j d_i}, C_{jk} = \frac{V_j d_k}{V_j d_k + V_k d_j}, C_{ki} = \frac{V_k d_i}{V_k d_i + V_i d_k} \dots (31)$$

$$C_i = C_{ij} + C_{ki} \dots (32)$$

$$C_j = C_{jk} + C_{ij} \dots (33)$$

$$C_k = C_{ki} + C_{jk} \dots (34)$$

In order to calculate the exact grain size, we took the aid of High resolution TEM images

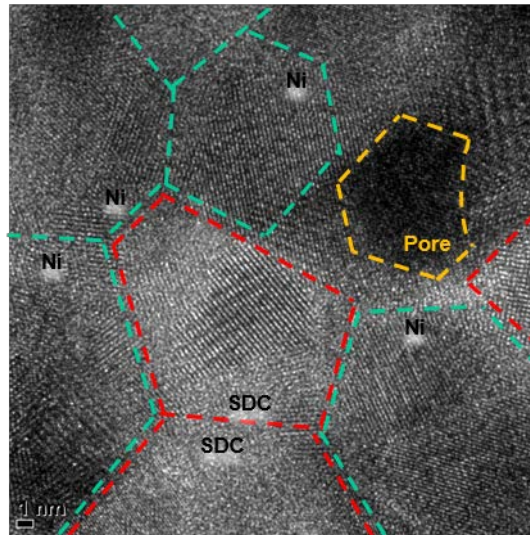


Fig.51 HRTEM image of the Ni-SDC anode, clearly distinguishing the Ni, SDC and Pore grain sizes

Table 12. Average grain sizes, contiguities and tortuosities for the three phases

Parameter	Ni	SDC	Pore
Avg. Grain size[d]	9 nm	13 nm	6nm
Contiguity of a phase [Ci]	0.8703	1.0366	1.0897
Tortuosity Factor[1/Ci] ²	1.32	0.93	0.84

(HRTEM) images. Fig. 51 shows the HRTEM image, where the Ni, SDC and pore phases were clearly distinguished. Table 12 shows the average grain size of the particles calculated from the HRTEM images. Contiguities of the phases were calculated from Eq. 32-34. Previously contiguity of a species has been shown to have an inverse relationship with tortuosity [99]. So the tortuosity factor has also been calculated in Table 12. The values of tortuosity are slightly lower than the ones cited in other Ni-Cermet anodes made by conventional methods[96], showing that the gas pathways and electrical conduction through sputtered media less tortuous (more favorable to easier conduction).

Once the tortuosity was calculated, we now calculated the diffusion of fuel gas molecules through the pores. The two gases were 1:CO and 2:CO₂, and their diffusion through porous Ni-SDC anode was defined by using Dusty Gas Model (DGM). DGM is written as a relationship of molar flux, molar fraction, and total pressure gradient.

$$\frac{N_i}{D_{i,K}^{eff}} + \sum_{j=1, j \neq i}^n \frac{X_j N_i - X_i N_j}{D_{ij}^{eff}} = -\frac{P_i}{RT} \nabla X_i - \frac{X_i}{RT} \left(1 + \frac{K P_t}{\mu D_{i,K}^{eff}} \right) \nabla P_t \dots (35)$$

Effective molecular diffusion coefficient can be expressed as a relationship of Volume fraction and tortuosity with Fuller-Schettler Giddings Equation

$$D_{ij}^{eff} = \frac{V_{pore}}{\tau_{pore}} D_{ij} \dots (36)$$

$$D_{ij} = \frac{0.01013 T^{1.75} \left(\left(\frac{1}{M_i} * 10^3 \right) + \left(\frac{1}{M_j} * 10^3 \right) \right)^{1/2}}{P \left((\sum v_i * 10^6)^{1/3} + (\sum v_j * 10^6)^{1/3} \right)^2} \dots (37)$$

Knudsen diffusion is a type of diffusion where the scale length of system is comparable or smaller to the mean free path of the species travelling through that system. In the Ni-SDC porous electrode, it is estimated that the mean free-path of the molecules is larger than the anode pore size, which means the collisions between the molecules and the boundaries of the anode, are more frequent than with other neighboring molecules. Therefore, it is better to use a Knudsen diffusion coefficient to estimate the reactants and products of the reverse boudouard reaction in this case

$$D_{i,K}^{eff} = \frac{V_{pore}}{\tau_{pore}} D_{i,K} \dots (38)$$

$$D_{i,K} = \frac{d_p}{3} \sqrt{\frac{8RT}{\pi M_i}} \dots (39)$$

$$d_p = \frac{4}{\left(\frac{S}{V} \right)_{pore}} \dots (40)$$

Permeability is defined by combining the Darcy's flow and Poiseuille's flow

$$K = \frac{V_{pore}}{6\tau_{pore} \left(\frac{S}{V} \right)_{pore}^2} \dots (41)$$

We can relate the conservation of gases transported by the Knudsen diffusion, with the charge transfer current by this relation

$$\nabla \cdot \left(\frac{k_1}{RT} \nabla P_1 \right) + \nabla \cdot \left(\frac{k_{1'} P_1}{RT} \nabla P_t \right) = \frac{i_{tpb}}{2F} \dots (42)$$

$$\nabla \cdot \left(\frac{k_2}{RT} \nabla P_2 \right) + \nabla \cdot \left(\frac{k_{2'} P_2}{RT} \nabla P_t \right) = - \frac{i_{tpb}}{2F} \dots (43)$$

$$k_1 = \frac{D_{12}^{eff} \cdot D_{1,K}^{eff}}{D_{12}^{eff} + D_{12,K}^{eff}} \dots (44)$$

$$k_2 = \frac{D_{12}^{eff} \cdot D_{2,K}^{eff}}{D_{12}^{eff} + D_{12,K}^{eff}} \dots (45)$$

$$k_{1'} = k_{2'} = \frac{K}{\mu} + \frac{D_{1,K}^{eff} \cdot D_{2,K}^{eff}}{D_{12}^{eff} + D_{12,K}^{eff}} \cdot \frac{1}{P_t} \dots (46)$$

Combined effective Knudsen diffusion coefficient is expressed as

$$D_{12,K}^{eff} = X_1 D_{2,K}^{eff} + X_2 D_{1,K}^{eff} \dots (47)$$

Since the total pressure is assumed to be constant, hence we can neglect the equations containing P_t terms. Then all the equations take the form of the Poisson-like equation

$$\nabla * (\sigma_{el}^{eff} \cdot \nabla \phi_{el}) = i_{tpb} \quad , \quad \nabla * (\sigma_{io}^{eff} \cdot \nabla \phi_{io}) = -i_{tpb}$$

$$\nabla * (\Gamma \cdot \nabla \phi) \pm S = 0$$

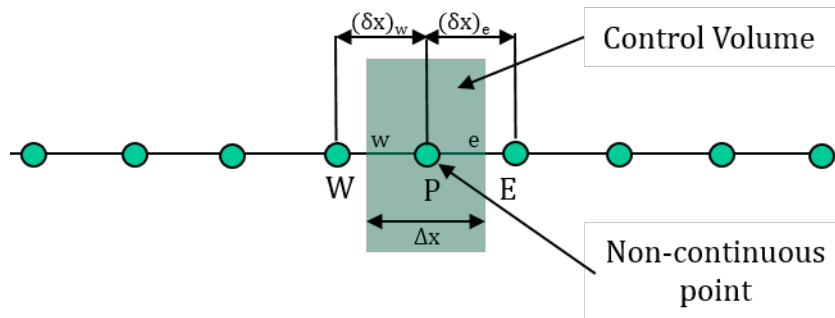


Fig.52 Schematic representation of the point P inside the Ni-SDC anode solved by control volume method

Here S is the source of charge transfer between the electronic and ionic phase. The charge conservation equation is solved for the involved charge transport in the ionic/electronic phase. It involves the solution of the Poisson equations for the ionic/electric field over the entire region.

A 1-D steady state diffusion equation is solved by control volume method (CV) over the entire region to find the solution of this Poisson equation. Fig. 52 shows the control volume schematic representation over a certain point P in consideration.

$$\frac{d}{dx} \left(\Gamma \cdot \frac{d\phi}{dx} \right) + S = 0$$

Integrating it inside a control volume from w to e

$$\int_w^e \left[\frac{d}{dx} \left(\Gamma \cdot \frac{d\phi}{dx} \right) + S \right] dx = 0$$

$$\left(\Gamma \cdot \frac{d\phi}{dx} \right)_e - \left(\Gamma \cdot \frac{d\phi}{dx} \right)_w + \int_w^e S dx = 0$$

Table 13. Boundary conditions for the control volume 1D steady state simulation of the Ni-SDC anode

Parameter	Surface(X=0)	Interface(X=L)
Total Pressure	$P_t(0) = P_t^{bulk}$	$\frac{dP_t}{dx}(L) = 0$
CO partial pressure	$P_{CO}(0) = P_{CO}^{bulk}$	$\frac{dP_{CO}}{dx}(L) = 0$
CO ₂ partial pressure	$P_{CO_2}(0) = P_{CO_2}^{bulk}$	$\frac{dP_{CO_2}}{dx}(L) = 0$
Electric potential in Ni	$\phi_{el}(0) = \eta_t$	$\frac{d\phi_{el}}{dx}(L) = 0$
Electronic & Ionic Potential in SDC	$\frac{d\phi_{el}}{dx}, \frac{d\phi_{io}}{dx} = 0$	$\phi_{el}(L), \phi_{io}(L) = 0$

$$\frac{\Gamma(\phi_E - \phi_P)}{(\delta x)_e} - \frac{\Gamma(\phi_P - \phi_W)}{(\delta x)_w} + S\Delta x = 0 \dots (48)$$

Here we use a uniform grid system of infinitely small grid points and use the function of circular reference in excel to get the value of the desired point. Since the input value of the point includes the value of that specific point, hence circular reference function in excel gives a viable option. We used a grid system of about 200 points and iterated them over an average of 1000 iterations to give the desired result. For a uniform grid system, $\delta x = \Delta x$, so Eq. 48 rearranges to

$$\phi_P = \left(\frac{\phi_E + \phi_W}{2} \right) + \frac{S(\delta x)^2}{2\Gamma} \dots (49)$$

And this is what we basically solve to attain the desired value through iterations in excel. Table 14 summarizes the results of the calculated parameters from the HRSEM images and the above

defined equations. All of these results were used as input parameters to solve the steady state diffusion equations. The units were kept consistently SI.

Table 14. Calculated parameters for simulation

Parameter	Symbol	Value	Unit
Total Pressure	$P_{t,bulk}$	101325	[Pa]
Temperature	T	1073-873	[K]
CO partial pressure	$P_{CO,bulk}$	$0.97 * P_{t,bulk}$	[Pa]
CO ₂ partial pressure	$P_{CO_2,bulk}$	$0.03 * P_{t,bulk}$	[Pa]
Ni Volume Fraction	V_{Ni}	0.273	
SDC Volume Fraction	V_{SDC}	0.571	
Pore Volume Fraction	V_{Pore}	0.156	
Ni Tortuosity Factor	τ_{Ni}	1.32	
SDC Tortuosity Factor	τ_{SDC}	0.93	
Pore Tortuosity Factor	τ_{Pore}	0.84	
Pore Diameter	d	$6*10^{-6}$	[m]
TPB Density	l_{tpb}	$3.35*10^{12}$	[m/m ³]
Anode Thickness	L	$5*10^{-7}$	[m]

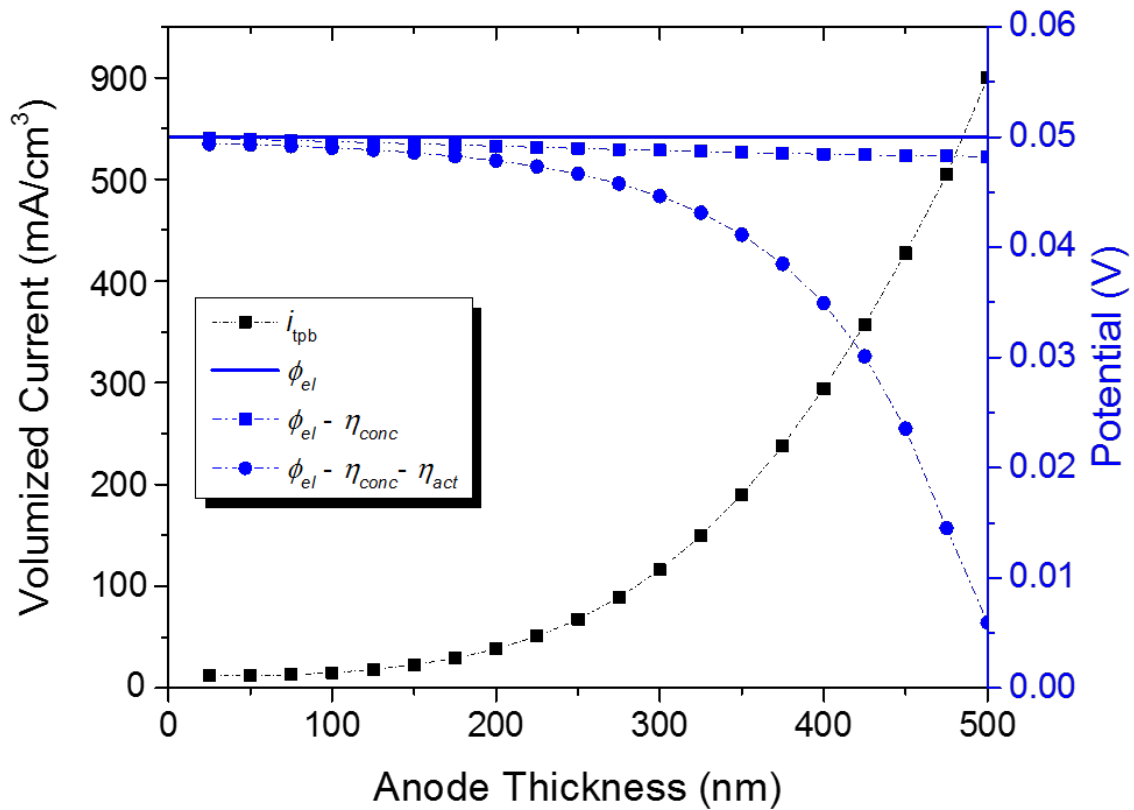


Fig 53. Volume specific current and potential distributions from simulation. Anode over-potential is set to be 0.05V

Fig. 53 shows typical distributions of the potentials and the volume specific current inside the anode in the thickness direction. The left hand of the Fig. 53 corresponds to the anode surface while the right side shows the electrolyte-anode interface. We can see that largest i_{tpb} (charge transfer current) is at the interface, but some current is still available at about 200nm distance from the interface. To the authors knowledge, this is the first time the active region thickness of a cermet anode is reported for such a thin nanostructure. The anode over-potential is fixed at 0.05 for studying a sample test case. Since the fuel supply (Through CO₂ reduction) is

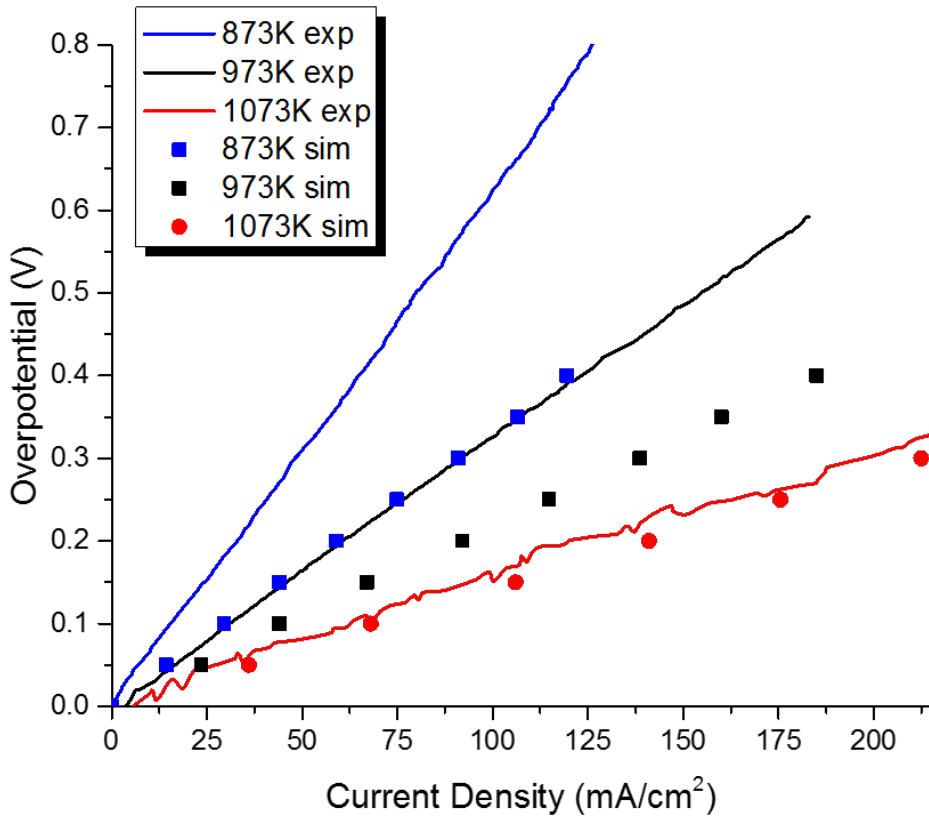


Fig 54. Anode over-potentials at various temperatures for indirect carbon fueled SOFC

constant, the concentration over-potential is very small (blue squares). And naturally the activation losses tend to decrease towards the right side of the figure (blue circles) as there is more charge transfer opportunities available at the interface.

Fig. 54 shows the effect of the operating temperature on the anode over-potential. The simulated over-potential agrees fairly well with the experimental counterpart at high temperature of 1073 K (800°C). The anode over-potential increases with the operating temperature decrease in the experiment. The simulation can reproduce this tendency but in the low temperature

conditions, 973-873K, it is overestimated especially in the large current density region. One of the reasons could be that the reverse boudouard reaction that is taking place outside the cell is heated at near 800°C, so the fuel gas doesn't experience any temperature gradient when it finds the cell at the very same temperature. But at lower cell operating temperatures (600-700°C) the CO fuel might experience a sudden temperature gradient when it enters the fuel cell chamber. The exact temperature loss could not be exactly estimated and was not accounted for in this simulation. Nonetheless we can still fairly match the trend of the nanostructured anode working on CO₂ reduction via carbon fuel, within acceptable limits at high temp range.

We also were able to see the anode structure in high resolution STEM image Fig. 55. The figure on the left side shows the Ni-SDC on top of the zirconia electrolyte. Fig55(b) shows the EDX representation of the same image. We can see that orange dots represent ceria while the sea blue color areas represent Ni. Below that is of course zirconia and the black empty marks are actually pores. So we can see that the cermet anode is arranged systematically with ceria rings surrounding the Ni particles. The schematic of such arranged nanostructured is shown in Fig. 4(c) So we can assume the conduction of the O₂ ions through the cathode via the electrolyte and where there is a triple phase boundary, the electrochemical reaction will take place, producing the necessary electrons conducted by the Ni. To the author's knowledge, this is the first time that the structure of a sputtered cermet anode of this size is seen under TEM and their arrangement explained. It is probably due to this arranged structure that the tortuosity (or blockage to conduction of gases through pores and conduction of ions and electrolytes) of the thin porous electrodes is found lower in simulation, resulting in higher charge transfer currents throughout the cermet anode

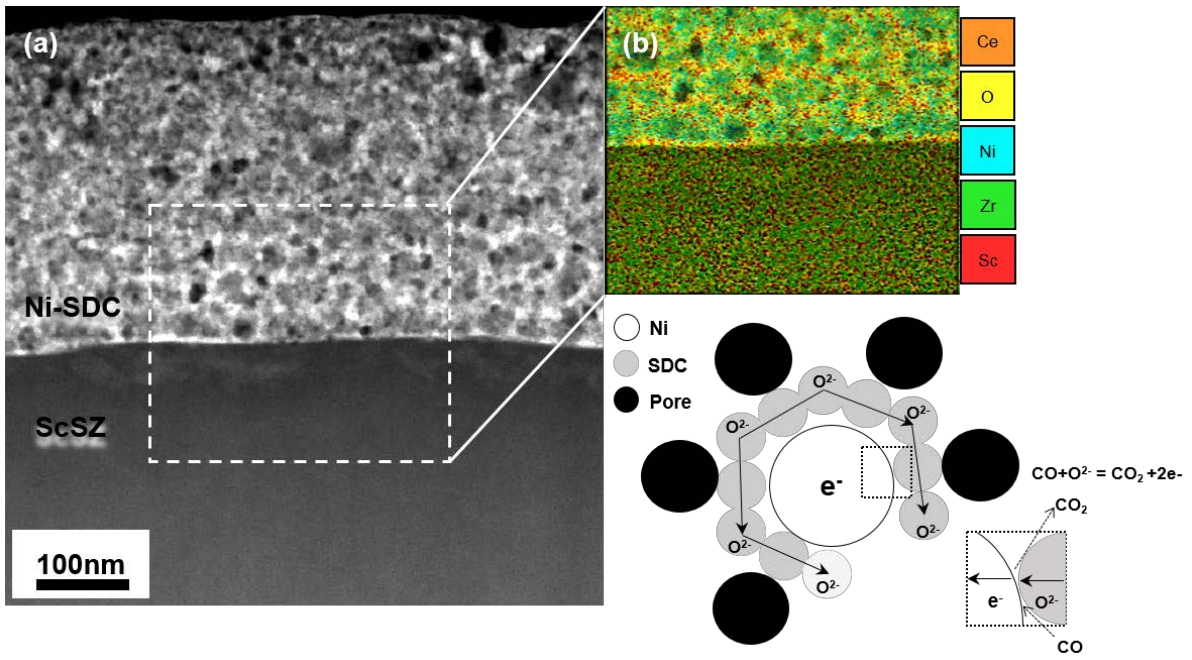


Fig. 55 (a) Scanning Transmission Electron Microscope (STEM) image of the Ni-SDC anode on top of the ScSZ electrolyte (b) EDX image of the electrolyte and anode junction (c) schematic representation of the Ni-SDC TPBs.

6. Concluding Remarks

6.1 Conclusion

Thin film nickel-ceria based anode cells were fabricated via two physical vapor deposition methods, PLD, and RF sputtering. The anodes were supported on a 150 μ m zirconia based electrolyte support having a screen printed 20 μ m LSM/YSZ cathode on the other end. Under H₂ fuel, the PLD Ni-SDC cells exhibited a rather poor performance. It was only when the target temperature was increased up to 700°C that the cells showed a meager improvement in performance. For RF sputtering of the Ni-SDC anodes, firstly, two sputtering background gases were analyzed a) non-reactive Ar only b) reactive Ar/O₂:80/20. It was found that O₂ reactive sputtering background gas, i) retards growth rate, ii) decreases performance, iii) produces lower catalytic Ni, and iv) shows higher agglomeration with time, in Ni-SDC cermet anodes, when compared to the anodes produced with a non-reactive background gas. Once the proper background gas for thin film cermet anode deposition was established, the optimal RF sputtering pressure and power conditions were logged. A range of sputtering powers from 50W ~ 200W with various background Ar pressures of 30mTorr ~ 90mTorr were analyzed. It was found out that in general, deposition rate of the thin films grew exponentially with the increase in sputtering power for the same target. Also peak power density increased linearly with the increase of anode sputtering power. Also, the shape of the thin film Ni-SDC grains changes from, rice like at 50W to circular shaped 200W sputtering powers. Remarkably, the anodes made at the largest pressure and highest power were not the ones that showed the best performance at an intermediate temperature of 700°C. After various experiments under same conditions, the optimum conditions for an excellent performing Ni-SDC anode were found to be 50mTorr Ar at 100W RF sputtering power.

Once the optimal anode conditions were established, the optimal cell was now ready to be tested by carbon fuel source via the Boudouard reaction. Two different types of carbon were

tested, one was pure, conductive, processed carbon Super P-Li, and the other was non-processed, impure, waste-carbon. It was witnessed that even after costly and lengthy processes, thin film Ni-SDC anode did not favor an electrochemical reaction with solid carbon fuel. Once the anode was removed and cells were tested with carbon as a fuel as well as an anode, the impure waste-carbon performed better than the pure Super P-Li carbon. It was deduced that this improvement in performance was due to the presence of impurities like Al and Si, that facilitated the oxidation of carbon at high temperatures. Nonetheless, direct carbon was not the proper choice to use with a thin film anode, so we shifted towards gasification of waste-carbon via Reverse-Boudouard Reaction (RBR). The product of RBR, CO, was made outside the fuel cell chamber in a simple home-made bubbler fitted with an inconel filter. The cells showed unsatisfactory performance with this system and soon stopped performing due to unfavorable reaction conditions between C and CO₂ that constitute the RBR at high temperatures. The bubbler design was updated and this time it was ensured that no CO₂ goes wasted without reacting with the carbon. The new designed bubbler showed immediate improvement, with OCVs of nearly 0.9V and a peak power density that was 82% of when the same cell was operated under hydrogen fuel. The system shown in this research was tested to produce an average OCV of 0.8V over a period of 100hrs. Additionally, there was no need to process the waste-carbon by this method, which would save cost and time. Due to the optimal methods used to produce thin film cermet anodes with indirect carbon fuel source, the results presented in this thesis report, matched, and at times outperformed, the results shown in other cited researches of the same category.

Simulation of the thin film anodes was done by the aid of high resolution 2D SEM and HRTEM images projected along the nanometer thickness. Simulation results matched fairly with the experimental ones. This was the first attempt to successfully model thin cermet anode

films fueled by carbon by simple 2D imaging. The combination of cheap fuel conversion methods with the state-of-the art thin film fabrication processes to produce high performance renewable energy conversion systems, like the one shown in this thesis, have a prospect of paving the way for a responsible green energy future.

6.2 Future Work

The international market for carbon fuel cells(CFCs) is still small compared to SOFC and PEMFCs. To improve the standing of CFCs, one needs to combine the simple carbon gasification methods, with state-of-the art fabrication technologies that can be tested for superior performances for longer operation times. Even though our methods outperformed many of the same category researchers' output, a margin of improvement will always be there for those who dare to excel.

From the promising results achieved in this paper, I intend to apply the simple and cost effective methods of carbon gasification shown here, to fuel cells where all the constituents, including the electrolytes and the electrodes, are made up of thin film deposition methods. Only with the proper research utilization of all aspects this low cost fuel, we shall be able to successfully implement the CFCs in the carbon energy infrastructure, that will lead to the reduction in emission of greenhouse gases and global warming, ultimately realizing the dream of a greener future.

References

- [1] Fuel cell fundamentals, Second edition, 2nd ed.. ed., Hoboken, NJ : John Wiley & Sons, Hoboken, NJ, 2009.
- [2] M.R. Allen, D.J. Frame, C. Huntingford, C.D. Jones, J.A. Lowe, M. Meinshausen, N. Meinshausen, Warming caused by cumulative carbon emissions towards the trillionth tonne, *Nature*, 458 (2009) 1163-1166.
- [3] M. Eby, K. Zickfeld, A. Montenegro, D. Archer, K.J. Meissner, A.J. Weaver, Lifetime of Anthropogenic Climate Change: Millennial Time Scales of Potential CO₂ and Surface Temperature Perturbations, *Journal of Climate*, 22 (2009) 2501-2511.
- [4] H.D. Matthews, N.P. Gillett, P.A. Stott, K. Zickfeld, The proportionality of global warming to cumulative carbon emissions, *Nature*, 459 (2009) 829-832.
- [5] W.R. Grove, XXIV. On voltaic series and the combination of gases by platinum, *Philosophical Magazine Series 3*, 14 (1839) 127-130.
- [6] R.M. Ormerod, Solid oxide fuel cells, *Chemical Society Reviews*, 32 (2003) 17-28.
- [7] O. Yamamoto, Solid oxide fuel cells: fundamental aspects and prospects, *Electrochimica Acta*, 45 (2000) 2423-2435.
- [8] E.D. Wachsman, K.T. Lee, Lowering the temperature of solid oxide fuel cells, *Science*, 334 (2011) 935-939.
- [9] C.G. LLC, Precious Metals Outlook March 2017, in, 2017.
- [10] R.F. Service, The hydrogen backlash, *Science*, 305 (2004) 958-961.
- [11] A. Hugo, P. Rutter, S. Pistikopoulos, A. Amorelli, G. Zoia, Hydrogen infrastructure strategic planning using multi-objective optimization, *International Journal of Hydrogen Energy*, 30 (2005) 1523-1534.

- [12] Kitco, 24hr Nickel, in, Kitco.
- [13] A. Atkinson, S. Barnett, R.J. Gorte, J.T.S. Irvine, A.J. McEvoy, M. Mogensen, S.C. Singhal, J. Vohs, Advanced anodes for high-temperature fuel cells, *Nat Mater*, 3 (2004) 17-27.
- [14] B.C.H. Steele, A. Heinzl, Materials for fuel-cell technologies, *Nature*, 414 (2001) 345-352.
- [15] S.T. Aruna, M. Muthuraman, K.C. Patil, Synthesis and properties of Ni-YSZ cermet: anode material for solid oxide fuel cells, *Solid State Ionics*, 111 (1998) 45-51.
- [16] J.H. Lee, H. Moon, H.W. Lee, J. Kim, J.D. Kim, K.H. Yoon, Quantitative analysis of microstructure and its related electrical property of SOFC anode, Ni-YSZ cermet, *Solid State Ionics*, 148 (2002) 15-26.
- [17] Z. Cheng, M. Liu, Characterization of sulfur poisoning of Ni-YSZ anodes for solid oxide fuel cells using in situ Raman microspectroscopy, *Solid State Ionics*, 178 (2007) 925-935.
- [18] H. He, J.M. Hill, Carbon deposition on Ni/YSZ composites exposed to humidified methane, *Applied Catalysis A: General*, 317 (2007) 284-292.
- [19] S. Ahmed, M. Krumpelt, Hydrogen from hydrocarbon fuels for fuel cells, *International Journal of Hydrogen Energy*, 26 (2001) 291-301.
- [20] F. Joensen, J.R. Rostrup-Nielsen, Conversion of hydrocarbons and alcohols for fuel cells, *Journal of Power Sources*, 105 (2002) 195-201.
- [21] Y.M.A. Welaya, M.M. El Gohary, N.R. Ammar, Steam and partial oxidation reforming options for hydrogen production from fossil fuels for PEM fuel cells, *Alexandria Engineering Journal*, 51 (2012) 69-75.
- [22] X. Dong, L. Tian, J. Li, Y. Zhao, Y. Tian, Y. Li, Single layer fuel cell based on a composite of $\text{Ce}_{0.8}\text{Sm}_{0.2}\text{O}_{2-\delta}$ - Na_2CO_3 and a mixed ionic and electronic conductor $\text{Sr}_2\text{Fe}_{1.5}\text{Mo}_{0.5}\text{O}_{6-\delta}$, *Journal of Power Sources*, 249 (2014) 270-276.

- [23] S. Shen, Y. Yang, L. Guo, H. Liu, A polarization model for a solid oxide fuel cell with a mixed ionic and electronic conductor as electrolyte, *Journal of Power Sources*, 256 (2014) 43-51.
- [24] M. Hashinokuchi, R. Yokochi, W. Akimoto, T. Doi, M. Inaba, J. Kugai, Enhancement of anode activity at Ni/Sm-doped CeO₂ cermet anodes by Mo addition in NH₃-fueled solid oxide fuel cells, *Solid State Ionics*, 285 (2016) 222-226.
- [25] C.S. Ni, J.M. Vohs, R.J. Gorte, J.T.S. Irvine, Fabrication and characterisation of a large-area solid oxide fuel cell based on dual tape cast YSZ electrode skeleton supported YSZ electrolytes with vanadate and ferrite perovskite-impregnated anodes and cathodes, *Journal of Materials Chemistry A*, 2 (2014) 19150-19155.
- [26] B. Shri Prakash, S. Senthil Kumar, S.T. Aruna, Properties and development of Ni/YSZ as an anode material in solid oxide fuel cell: A review, *Renewable and Sustainable Energy Reviews*, 36 (2014) 149-179.
- [27] K. Bae, S. Lee, D.Y. Jang, H.J. Kim, H. Lee, D. Shin, J.-W. Son, J.H. Shim, High-Performance Protonic Ceramic Fuel Cells with Thin-Film Yttrium-Doped Barium Cerate–Zirconate Electrolytes on Compositionally Gradient Anodes, *ACS applied materials & interfaces*, 8 (2016) 9097-9103.
- [28] J. Park, Y. Lee, I. Chang, W. Lee, S.W. Cha, Engineering of the electrode structure of thin film solid oxide fuel cells, *Thin Solid Films*, 584 (2015) 125-129.
- [29] W. Jung, J.J. Kim, H.L. Tuller, Investigation of nanoporous platinum thin films fabricated by reactive sputtering: Application as micro-SOFC electrode, *Journal of Power Sources*, 275 (2015) 860-865.
- [30] <https://en.wikipedia.org/w/index.php?title=Carbon&oldid=766736398>, in.
- [31] D. Smith How much does the Earth weigh? What does the Lithosphere weigh?, in: Lindsey

(Ed.), MadSci Network, 1998.

[32] J.M. Beér, High efficiency electric power generation: The environmental role, *Progress in Energy and Combustion Science*, 33 (2007) 107-134.

[33] I.C. Change, Mitigation of climate change, *Summary for Policymakers*, 10 (2007).

[34] A. Franco, A.R. Diaz, The future challenges for “clean coal technologies”: joining efficiency increase and pollutant emission control, *Energy*, 34 (2009) 348-354.

[35] C.C.M. Chen, T., H.P. H., S.J. R., The reverse Boudouard reaction in Direct Carbon Fuel Cells *ECS Transactions*, 28 (2010).

[36] Y. Tang, J. Liu, Effect of anode and Boudouard reaction catalysts on the performance of direct carbon solid oxide fuel cells, *International Journal of Hydrogen Energy*, 35 (2010) 11188-11193.

[37] Y. Wu, C. Su, C. Zhang, R. Ran, Z. Shao, A new carbon fuel cell with high power output by integrating with in situ catalytic reverse Boudouard reaction, *Electrochemistry Communications*, 11 (2009) 1265-1268.

[38] T.M. Gur, Critical review of carbon conversion in "carbon fuel cells", *Chem Rev*, 113 (2013) 6179-6206.

[39] S. Giddey, S.P.S. Badwal, A. Kulkarni, C. Munnings, A comprehensive review of direct carbon fuel cell technology, *Progress in Energy and Combustion Science*, 38 (2012) 360-399.

[40] A.C. Rady, S. Giddey, S.P.S. Badwal, B.P. Ladewig, S. Bhattacharya, Review of Fuels for Direct Carbon Fuel Cells, *Energy & Fuels*, 26 (2012) 1471-1488.

[41] M.T. Mehran, T.-H. Lim, S.-B. Lee, J.-W. Lee, S.-J. Park, R.-H. Song, Long-term performance degradation study of solid oxide carbon fuel cells integrated with a steam gasifier, *Energy*, 113 (2016) 1051-1061.

[42] W.H. Tanveer, S. Ji, W. Yu, G.Y. Cho, Y.H. Lee, T. Park, Y. Lee, Y. Kim, S.W. Cha, Effect

of 20% O₂ reactive gas on RF-sputtered Ni-SDC cermet anodes for intermediate temperature solid oxide fuel cells, *Current Applied Physics*, 16 (2016) 1680-1686.

[43] Y. Ye, L. Rihko-Struckmann, B. Munder, H. Rau, K. Sundmacher, Feasibility of an Electrochemical Membrane Reactor for the Partial Oxidation of n-Butane to Maleic Anhydride, *Industrial & Engineering Chemistry Research*, 43 (2004) 4551-4558.

[44] J. Piao, K. Sun, N. Zhang, S. Xu, A study of process parameters of LSM and LSM-YSZ composite cathode films prepared by screen-printing, *Journal of Power Sources*, 175 (2008) 288-295.

[45] S. Ohara, R. Maric, X. Zhang, K. Mukai, T. Fukui, H. Yoshida, T. Inagaki, K. Miura, High performance electrodes for reduced temperature solid oxide fuel cells with doped lanthanum gallate electrolyte, *Journal of Power Sources*, 86 (2000) 455-458.

[46] A. De Giacomo, V.A. Shakhmatov, G.S. Senesi, S. Orlando, Spectroscopic investigation of the technique of plasma assisted pulsed laser deposition of titanium dioxide, *Spectrochimica Acta Part B: Atomic Spectroscopy*, 56 (2001) 1459-1472.

[47] M. Kuzma, M. Bester, L. Pyziak, I. Stefaniuk, I. Virt, Modelling of growth of thin solid films obtained by pulsed laser deposition, *Applied Surface Science*, 168 (2000) 132-135.

[48] A. Sambri, S. Amoruso, X. Wang, M. Radovic', F. Miletto Granozio, R. Bruzzese, Substrate heating influence on plume propagation during pulsed laser deposition of complex oxides, *Applied Physics Letters*, 91 (2007) 151501.

[49] A. Sambri, M. Radovic', X. Wang, S. Amoruso, F.M. Granozio, R. Bruzzese, Substrate heating effects on the propagation dynamics of laser produced plume during pulsed laser deposition of oxides, *Applied Surface Science*, 254 (2007) 790-793.

[50] L.V. Zhigilei, Dynamics of the plume formation and parameters of the ejected clusters in short-pulse laser ablation, *Applied Physics A: Materials Science & Processing*, 76 (2003) 339-

350.

[51] Fuel cell fundamentals , second edition, 2nd ed.. ed., Hoboken, NJ : John Wiley & Sons, Hoboken, NJ, 2009.

[52] H.-S. Noh, J.-S. Park, J.-W. Son, H. Lee, J.-H. Lee, H.-W. Lee, Physical and Microstructural Properties of NiO- and Ni-YSZ Composite Thin Films Fabricated by Pulsed-Laser Deposition at 700°C , Journal of the American Ceramic Society, 92 (2009) 3059-3064.

[53] W.R. Burkardt, R., Methods of Coating Articles by vaporized coating materials, in: U.S.P. Office (Ed.), United States, 1939.

[54] B. Berghaus, Method of cathode disintegration, in: U.S.P. Office (Ed.), United States, 1941.

[55] B. Berghaus, Coating of Articles by Cathode Disintegration, in: U.S.P. Office (Ed.), United States, 1942.

[56] W.H. Tanveer, S. Ji, W. Yu, S.W. Cha, Characterization of atomic layer deposited and sputtered yttria-stabilized-zirconia thin films for low-temperature solid oxide fuel cells, International Journal of Precision Engineering and Manufacturing, 16 (2015) 2229-2234.

[57] H. Kishimoto, A. Suzuki, T. Shimonosono, M.E. Brito, K. Yamaji, T. Horita, F. Munakata, H. Yokokawa, Agglomeration behavior of nickel particles on YSZ electrolyte, Solid State Ionics, 225 (2012) 65-68.

[58] W.D. Sproul, D.J. Christie, D.C. Carter, Control of reactive sputtering processes, Thin Solid Films, 491 (2005) 1-17.

[59] Fuel cell fundamentals, first ed., First ed., Hoboken, NJ : John Wiley & Sons, Hoboken, NJ, 2006.

[60] Q. Liu, X. Dong, C. Yang, S. Ma, F. Chen, Self-rising synthesis of Ni-SDC cermets as anodes for solid oxide fuel cells, Journal of Power Sources, 195 (2010) 1543-1550.

- [61] R. Nishida, K. Kakinuma, H. Nishino, T. Kamino, H. Yamashita, M. Watanabe, H. Uchida, Synthesis of nickel nanoparticles supported on hollow samaria-doped ceria particles via the solution-spray plasma technique: Anode catalysts for SOFCs, *Solid State Ionics*, 180 (2009) 968-972.
- [62] A.P. Grosvenor, M.C. Biesinger, R.S.C. Smart, N.S. McIntyre, New interpretations of XPS spectra of nickel metal and oxides, *Surface Science*, 600 (2006) 1771-1779.
- [63] A. Fujimori, Mixed-valent ground state of CeO₂, *Physical Review B*, 28 (1983) 2281-2283.
- [64] Fuel cell fundamentals , second edition, 2nd ed. ed., Hoboken, NJ : John Wiley & Sons, Hoboken, NJ, 2009.
- [65] B.B. Sahu, J.G. Han, J.B. Kim, M. Kumar, S. Jin, M. Hori, Study of Plasma Properties for the Low-Temperature Deposition of Highly Conductive Aluminum Doped ZnO Film Using ICP Assisted DC Magnetron Sputtering, *Plasma Processes and Polymers*, 13 (2016) 134-146.
- [66] B.B. Sahu, K.S. Shin, S.B. Jin, J.G. Han, K. Ishikawa, M. Hori, Effectiveness of plasma diagnostic in ultra high frequency and radio frequency hybrid plasmas for synthesis of silicon nitride film at low temperature, *Journal of Applied Physics*, 116 (2014) 134903.
- [67] B.B. Sahu, J.G. Han, M. Hori, K. Takeda, Langmuir probe and optical emission spectroscopy studies in magnetron sputtering plasmas for Al-doped ZnO film deposition, *Journal of Applied Physics*, 117 (2015) 023301.
- [68] D. Beckel, A. Bieberle-Hütter, A. Harvey, A. Infortuna, U.P. Muecke, M. Prestat, J.L.M. Rupp, L.J. Gauckler, Thin films for micro solid oxide fuel cells, *Journal of Power Sources*, 173 (2007) 325-345.
- [69] H.F. Winters, P. Sigmund, Sputtering of chemisorbed gas (nitrogen on tungsten) by low-energy ions, *Journal of Applied Physics*, 45 (1974) 4760-4766.

- [70] W. Wen-Fa, C. Bi-Shiou, H. Shu-Ta, Effect of sputtering power on the structural and optical properties of RF magnetron sputtered ITO films, *Semiconductor Science and Technology*, 9 (1994) 1242.
- [71] H.L. Tuller, S.J. Litzelman, W. Jung, Micro-ionics: next generation power sources, *Phys Chem Chem Phys*, 11 (2009) 3023-3034.
- [72] J.H. Shim, J.S. Park, T.P. Holme, K. Crabb, W. Lee, Y.B. Kim, X. Tian, T.M. Gür, F.B. Prinz, Enhanced oxygen exchange and incorporation at surface grain boundaries on an oxide ion conductor, *Acta Materialia*, 60 (2012) 1-7.
- [73] R. Meyer, X. Guo, R. Waser, Nonlinear Electrical Properties of Grain Boundaries in Oxygen Ion Conductors Modeling the Varistor Behavior, *Electrochemical and Solid-State Letters*, 8 (2005) E67-E69.
- [74] E. Barsoukov, *Impedance Spectroscopy: Theory, Experiment, and Applications*, 2nd ed ed., Hoboken : John Wiley & Sons, Incorporated, Hoboken, 2005.
- [75] H. Huang, T.P. Holme, F.B. Prinz, Oxygen Reduction Characteristics on Ag, Pt, and Ag-Pt Alloys in Low-Temperature SOFCs, *ECS Transactions*, 3 (2007) 31-40.
- [76] D. Zeng, W. Jie, H. Zhou, Y. Yang, Effect of sputtering power on the properties of Cd_{1-x}Zn_xTe films deposited by radio frequency magnetron sputtering, *Thin Solid Films*, 519 (2011) 4158-4161.
- [77] D.H. Hwang, S. Cho, K.N. Hui, Y.G. Son, Effect of Sputtering Power on Structural and Optical Properties of Radio Frequency-Sputtered In₂S₃ Thin Films, *Journal of Nanoscience and Nanotechnology*, 14 (2014) 8978-8981.
- [78] Z. Chai, Y. Liu, X. Lu, D. He, Reducing adhesion force by means of atomic layer deposition of ZnO films with nanoscale surface roughness, *ACS applied materials & interfaces*, 6 (2014) 3325-3330.

- [79] N. White, A.L. Campbell, J.T. Grant, R. Pachter, K. Eyink, R. Jakubiak, G. Martinez, C.V. Ramana, Surface/interface analysis and optical properties of RF sputter-deposited nanocrystalline titanium nitride thin films, *Applied Surface Science*, 292 (2014) 74-85.
- [80] Bioenergylist.org, Boudouard Reaction spreadsheet, in.
- [81] O. Boudouard, Carbon Reactions, *Acad. Sci. Paris* 128, (1899) 824
1521.
- [82] P.L. Walker, F. Rusinko, L.G. Austin, Gas reactions of carbon, *Advances in catalysis*, 11 (1959) 133-221.
- [83] S.A. Freunberger, Y. Chen, N.E. Drewett, L.J. Hardwick, F. Bardé, P.G. Bruce, The Lithium–Oxygen Battery with Ether-Based Electrolytes, *Angewandte Chemie International Edition*, 50 (2011) 8609-8613.
- [84] L. Yang, L. Gao, Li₄Ti₅O₁₂/C composite electrode material synthesized involving conductive carbon precursor for Li-ion battery, *Journal of Alloys and Compounds*, 485 (2009) 93-97.
- [85] I. Lee, S. Jin, D. Chun, H. Choi, S. Lee, K. Lee, J. Yoo, Ash-free coal as fuel for direct carbon fuel cell, *Science China Chemistry*, 57 (2014) 1010-1018.
- [86] K. Styszko-Grochowiak, J. Gołaś, H. Jankowski, S. Koziński, Characterization of the coal fly ash for the purpose of improvement of industrial on-line measurement of unburned carbon content, *Fuel*, 83 (2004) 1847-1853.
- [87] S.A.A. Naqvi, M.T. Mehran, R.-H. Song, J.-W. Lee, S.-B. Lee, S.-J. Park, D.-R. Shin, T.-H. Lim, Performance evaluation of solid oxide carbon fuel cells operating on steam gasified carbon fuels, *Chemical Engineering Journal*, 300 (2016) 384-393.
- [88] C. Li, Y. Shi, N. Cai, Effect of contact type between anode and carbonaceous fuels on direct carbon fuel cell reaction characteristics, *Journal of Power Sources*, 196 (2011) 4588-

4593.

[89] X. Xu, W. Zhou, F. Liang, Z. Zhu, Optimization of a direct carbon fuel cell for operation below 700 C, *international journal of hydrogen energy*, 38 (2013) 5367-5374.

[90] Reaction Web, in.

[91] C. Li, Y. Shi, N. Cai, Performance improvement of direct carbon fuel cell by introducing catalytic gasification process, *Journal of Power Sources*, 195 (2010) 4660-4666.

[92] Y. Suzue, N. Shikazono, N. Kasagi, Micro modeling of solid oxide fuel cell anode based on stochastic reconstruction, *Journal of Power Sources*, 184 (2008) 52-59.

[93] H. Yakabe, Integrated Numerical Modeling of SOFCs: Mechanical Properties and Stress Analyses, (2008) 323-395.

[94] M. Kishimoto, H. Iwai, M. Saito, H. Yoshida, Quantitative evaluation of solid oxide fuel cell porous anode microstructure based on focused ion beam and scanning electron microscope technique and prediction of anode overpotentials, *Journal of Power Sources*, 196 (2011) 4555-4563.

[95] C. Nicollet, A. Flura, V. Vibhu, A. Rougier, J.M. Bassat, J.C. Grenier, La $2\text{NiO}_{4+\delta}$ infiltrated into gadolinium doped ceria as novel solid oxide fuel cell cathodes: Electrochemical performance and impedance modelling, *Journal of Power Sources*, 294 (2015) 473-482.

[96] H. Iwai, N. Shikazono, T. Matsui, H. Teshima, M. Kishimoto, R. Kishida, D. Hayashi, K. Matsuzaki, D. Kanno, M. Saito, H. Muroyama, K. Eguchi, N. Kasagi, H. Yoshida, Quantification of SOFC anode microstructure based on dual beam FIB-SEM technique, *Journal of Power Sources*, 195 (2010) 955-961.

[97] E.E. Underwood, The mathematical foundations of quantitative stereology, in: *Stereology and Quantitative Metallography*, ASTM International, 1972.

[98] Z. Fan, A. Miodownik, P. Tsakirooulos, Microstructural characterisation of two phase

materials, *Materials science and technology*, 9 (1993) 1094-1100.

[99] W.M. Harris, K.S. Brinkman, Y. Lin, D. Su, A.P. Cocco, A. Nakajo, M.B. DeGostin, Y.-c.K. Chen-Wiegart, J. Wang, F. Chen, Characterization of 3D interconnected microstructural network in mixed ionic and electronic conducting ceramic composites, *Nanoscale*, 6 (2014) 4480-4485.

국문 초록

Nickel-Samarium 기술 Ceria(Ni-SDC)서멧 양극의 얇은 막들 ScSZ 전해질에 준비되어 다른 배경 나오는 가스에 의해 RFsputtering 에 의해 지원됩니다. 일단 의도한 퇴적 상태 설립되었으며, 그 Ni-SDC 것 다른 sputtering powers(50W~200W)과 배경 아르곤 가스 pressures(30mTorr~90mTorr)의 범위에 보관되어 있다. 초기 결과는 양극 얇은 막들 증가 압력과 높은 부착력으로 만든 더 낮은 힘으로 움직이는 것보다 보여 주었다. 는 중간 산화물 연료 전지 온도 범위에서 최대 전력 출력을 보였다 흥미롭게도, 가장 높은 출력과 높은 압력에서 만들어진 anodes 유일한 세력이 아니었다. 결국, 최적의 조건 고성능 박막 Ni-SDC 것을 기록한 것. 이러한 고성능 것 그때는 단순한 집에서 만든 gasifier 에 역 boudouard 반응의 도움으로 생가공되지 않은 탄소를 이용해서 간접적인 탄소 연료의 원천에 따라 시험하였다.(위험도 근거 규제). 탄소 연료의 원천은 H₂ 연료 upto a)상시 첨두 출력 b)장수 c)비용을 낮추는 경기했다. 저자의 아는 바로는 서멧 양극 원료의 탄소원까지 날짜에 운영 이 일은 가장 높은 보고된 효율성이다.

얇은 영화 것의 시뮬레이션 고화질 2DSEM 과 HRTEM 이미지는 나노 미터 두께를 따라 예상의 도움에 의해 이루어졌다. 시뮬레이션 결과 양이 상당히 실험적인 것으로 경기했다. 이것은 첫번째 시도 성공적으로 얇은 인쇄 서멧 양극 영화 탄소가 단순한 2D 영상에 힘입어 모델에. 값싼 연료를 변환 방법의 state-of-the 예술 박막 제작과 조합은 프로세스, 이 중에서 나온 것처럼 고성능 재생

에너지 변환 시스템을 생산해야 한다. 논문 책임 있는 녹색 에너지 미래의 길을
될 가능성이 있다.